January 2017

Study Of Two-Phase And Single-Phase Flow Behavior In Channels Of Sudden Area Change Using Experimental And Computational Approach

Ashish Pramod Kotwal

STUDY OF TWO-PHASE AND SINGLE-PHASE FLOW BEHAVIOR IN CHANNELS OF SUDDEN AREA CHANGE USING EXPERIMENTAL AND COMPUTATIONAL APPROACH

By

Ashish Kotwal

Bachelor of Engineering, University of Mumbai, 2013

A Thesis

Submitted to the Graduate Faculty

of the

University of North Dakota

in partial fulfillment of the requirements

for the degree of

Master of Science

Grand Forks, North Dakota

Fall (December), 2017

This thesis, submitted by Ashish Kotwal, in partial fulfillment of the requirements for the Degree of Master of Science from the University of North Dakota, has been read by the Faculty Advisory Committee under whom the work has been done and is at this moment approved.

_____
Dr. Clement Tang, Chairperson

_____
Dr. Surojit Gupta

_____
Dr. Gautham Krishnamoorthy

This thesis is being submitted by the appointed advisory committee as having met all the requirements of the School of Graduate Studies at the University of North Dakota and is hereby approved.

_____
Dr. Grant McGimpsey,
Dean of the School of Graduate Studies

_____
Date

PERMISSION

Title Study of Two-phase and Single-phase Flow Behavior in Channels of Sudden Area Change Using Experimental and Computational Approach

Department Mechanical Engineering

Degree Master of Science

In presenting this thesis in partial fulfillment of the requirements for a graduate degree from the University of North Dakota, I agree that the library of this University shall make it freely available for inspection. I further agree that permission for extensive copying for scholarly purposes may be granted by the professor who supervised my thesis work or, in their absence, by the chairperson of the department or the dean of the School of Graduate Studies. It is understood that any copying or publication or other use of this dissertation or part thereof for financial gain shall not be allowed without my written permission. It is also understood that due recognition shall be given to me and to the University of North Dakota in any scholarly use which may be made of any material in my thesis.

Name: Ashish Kotwal

Date: November 11, 2017

TABLE OF CONTENTS

LIST OF FIGURES

FIGURE **PAGE**

LIST OF TABLE

TABLE **PAGE**

ACKNOWLEDGMENTS

I will never be able to finish my thesis without help and guide from my committee members, friends, my family. Especially, I would like to express my deepest gratitude to my advisor, Dr. Clement Tang, for his great support, good patience, consistent encouragement, and excellent guidance for my thesis and Master's program. I would like to express my sincere appreciation to Dr. Surojit Gupta and Dr. Gautham Krishnamoorthy for their useful advices and experiences sharing. I want to thank my Mom, Dad, and Sister for supporting and financing me, advising me time to time, keeping track of my events so that I should not miss any. Finally, I would like to thank my friends, especially Che-Hao Yang, Aristotle Postilione, Matthew Anderson for their generous and valuable advises and help. In addition, I would like to thank Spotify, for letting me hear awesome, magnificent Rock and Metal songs, and keeping my spirit high 24/7.

ABSTRACT

It is well recognized in continuum mechanics that the theoretical origination for single-phase flows fundamentally based on the beginning of field equations paraphrasing the conservation laws of mass, momentum, and energy. These equations are accompanied by the appropriate constitutive associations for thermodynamic state and energy transfer, which specify the thermodynamic and transport of a specific fundamental material. Nevertheless, the multi-phase flows equations derivation is, in general, considerably more convoluted than for single-phase flows. This is predominantly due to the presence of significant discontinuities of the fluid properties through the interfaces and complicated flow characteristics approximating the interfaces, separating the individual phases that co-exist within the flow, and multiple, deformable, and moving interfaces.

The purpose of this study is to use computational and experimental approach to understand the gas-liquid two-phase flow, and single-phase flow behavior in channels with sudden contraction/expansion. With the advances in computing capabilities and resources, researchers have continued to reevaluate the reliance of computational analysis and predictions to better understand the transport phenomena, and intricacies in multi-phase flows. Reliable computational approach can often be a more cost-effective tool than an experimental approach that requires accurate sensors and instrumentation. Four test sections with different sudden contraction and expansion in the cross-sectional areas were used in this study. The diameter ratios for the sudden contraction/expansion are 1.33, 1.59, 2.63, and 3.57. The range of flow rates are, for liquid, from 5 to 30 g/s (0.005 kg/s to 0.03 kg/s), and for gas, from 0.49 to 29 g/s (0.00049 kg/s to 0.028 kg/s).

using gauge pressure values form experimental setup, measured and analyzed data, and its assistance to validate computationally modelled data with detailed visualization of pressure profile,

is a one of principle topic of study. Along with it, pressure drop data collected from experimental analysis, and computationally acquired values, and validation between them. This is too prove that, the current computational model can be utilized for complex multiphase flow systems in industries. After validation, another goal of study is to generate pressure profiles, and local velocity profiles and study of their visualization to propose physics behind it.

The computational study for the two-phase flow used an Eulerian-Eulerian multiphase approach and the Reynolds stress turbulence model for two-phase gas-liquid flow with input from the experimental data for boundary conditions of solver. Prior to the two-phase and single-phase flow, grid independence study, and turbulence study is carried out. Turbulence study shows Reynold's turbulence model provides more accuracy than that of the k-ϵ model for higher flow rates. The optimized grid is implemented with the Reynolds stress dispersed multiphase flow turbulence model. Pressure drop along the channels of different area ratios was observed to be influence by the Reynolds number, along with that it is found to be directly proportional to pressure drop for channel. The Reynolds number calculated in the turbulence analysis is found to be 400 to 10000 as the pressure drop value increases and flow rate increases, for the area ratio of 0.1444. The pressure drop values are in range from 0.3 to 10 kPa, for the area ratio with 0.1444. While, the pressure drop values ranges from 0.0146 to 0.8 kPa for area ratio of 0.5625. This also proves that pressure drop is inversely proportional to hydraulic diameter. The after calculation of pressure profiles, the plotted pressure drop values show precise prediction of computational analysis and good agreement with experimental data with margin error of 1 to 11% for two-phase flows and 1 to 3% for single-phase flow for channels with smaller diameters.

NOMENCLATURE

P	Pressure [kPa or Pa].
ΔP	Pressure Drop [kPa or Pa].
A	Flow area [m^2].
C_c	Vena contracta coefficient.
g	Gravitational acceleration [m/s^2].
$\dot{m}$	Mass flow rate [kg/s].
$\Delta P_{sp,exp}$	Pressure drop due to sudden expansion, single-phase flow [Pa]
$\Delta P_{sp,con}$	Pressure drop due sudden contraction, single-phase flow [Pa]
$\Delta P_{tp,exp}$	Pressure drop due to sudden expansion, two-phase flow [Pa]
$\Delta P_{tp,con}$	Pressure drop due sudden contraction, two-phase flow [Pa]
Re	Reynolds number
v	Flow velocity [m/s]
T	Temperature [ºC]
ρ	Density [kg/m^3]
L	Test section length [m]

h_f	Head loss due to friction [m]
f_D	Darcy friction factor
D	Pipe diameter [m or inches]
D_h	Hydraulic diameter [m or inches]
S	Slip ratio
x	Mixture quality
U_{sl}	Superficial liquid velocity [m/s]
U_{sg}	Superficial gas velocity [m/s]
C_D	Coefficient of drag
G	Total mass flux, [kg/m^2s]
We	Weber number

Greek Symbols

σ	Area ratio.
β	Turbulent kinetic energy correction factor
μ	Viscosity [$Pa.s$ or $N.s/m^2$]
α	Void or volume fraction
μ_t	Turbulent viscosity

ϵ	Turbulent dissipation rate
Γ	Pressure coeffiient in Freidel's research
σ_{con}	Area ratio of test section for sudden contraction
σ_{exp}	Area ratio of test section for sudden expansion

Subscripts

con	Contraction
exp	Expansion
g	Gas phase (nitrogen)
l	Liquid phase (water)

CHAPTER I

INTRODUCTION

1.1 Conception

In this article, the author are computing the two-phase gas-liquid flow pressure drop generated across an immediate area of expansions and contractions using computational fluid dynamics simulations, by application of water as liquid and nitrogen as a gas. In addition, the attempt has been made to perform single-phase CFD numerical analysis prior to two-phase flow calculations using computational models while using only water as material. Further, these results compared with respect to experimental results.

Pressure drop defined as loss of pressure difference between two points of when fluid flows between these two points within fluid carrying network [1], [2]. Resistance to flow, flow area, density, elevation. Such as several can be prominent reasons lead to the pressure drop. Thus, the behavior and characteristics of the given fluid can result in conceptual understanding by measuring total pressure drop observation with high accuracy and estimation over the observation in that fluid flow. There are two parts of total pressure drop: the First one is irreversible pressure drop, which is caused by the irreversibility of the mechanical energy conversion [3]. For example, the friction loss and local loss that shows irreversibility of mechanical energy during fluid flow. The other called reversible pressure drop, for example, elevation pressure drop, and acceleration pressure drop.

1.2 Purpose

The purpose of this study to develop a unique mathematical model using experimental dataset and analyze how liquid flow and two-phase gas-liquid flow in close geometries of sudden area change such as sudden contraction or sudden expansion. The study entitles the fluid system behavior in channels with small diameters, which are diameters of 0.5 inches (0.0127 m) to 0.14 inches (0.003556 m). The channels have five different diameters, which allowed four area ratio variations for abrupt contraction and expansion conditions. After finishing experimental data assortment, mathematical model was decided to develop to validate the experimental data and vice a versa. Computational analysis was chosen to observe its microscopic details of flow, for example to find the behavior of flow in the corners of test section. Apart from this, the presentation of previous researchers were shown in accordance with present study made.

1.3 Expectation

The projected results of this experimental and computational study will indicate estimation of pressure profiles in detailed visualization and its validation based on locally collected and calculated individual gauge pressure values, the performance of the pressure drops in the sudden area changing channels and their validation using computational datasets and vice a versa, using collected initial data from experimental analysis. The results will provide useful data and mathematical modeling insights and their benefits to engineering applications involving multiphase flow systems with complex flow geometries.

1.4 Scope of this experiment

In this thesis, the area ratios of the test sections were 0.0784, 0.1444, 0.3844 and 0.5625 hence the computational meshes are made with same dimensions. During computational analysis, mass flow rate, were used as boundary condition, along with it, pressure data collected at first tap

and at the last tap, was useful for boundary conditions. In the two phase flow using Eulerian mathematics, two-fluid model was developed and the liquid as well as gas flow rates were implemented along with volume fractions to understand the local, individualistic phasic behavior of flow by plotting velocity vectors and profiles. The pressure drop, pressure profile comparison were observed.

1.5 Basic Definitions

Before initializing the understanding of the thesis, it is better to get to know some important phenomena, such as void/volume fraction, computational grid, mass flux, slip ratio, solver, and so forth.

Void/Volume fraction: Void/volume fraction (α) is defined as the ratio of the cross-sectional area occupied by the gas (A_g) to the total cross-sectional area of the pipe(A_p). Void/ volume fraction is a mathematical concept to explain the fluid phenomenon, which explains volume of space the gas occupies in the two-phase flow in the pipe.

$$\alpha = \frac{A_g}{A_p} = \frac{A_g}{A_l + A_g} \tag{1.1}$$

Many researchers have studied concept of void/volume fraction analytically as well as by experimentation. According to [4], comparison of 54 void fraction against a diverse experimental and mathematical data in vertical and horizontal two-phase flows, show few are excellent which represents drift flux model better. Co-relation by Woldesemayat, Ghajar for horizontal two-phase flows predicts better values for void fraction for particular microchannel.

Computational grid: To solve integral momentum, continuity equations by converting to sparse matrix algebraic equations, the specific geometrical volume is divided in small equidistant cells. These set of equally spaced cells are called as computational grid.

Solver: A program consist of set of different algorithms to solve the Navier-Stokes equations by converting them into sparse matrices using controlled volume technique, or immersed boundary method. There are many commercial and open-source command line based solvers available. In this study, solver by FLUENT is decided to use, due to wide popularity.

Slip Ratio (S): defined as the ratio of the average velocity of the gas phase (U_g) to the average velocity of the liquid phase(U_l). For S = 1, we get $U_g = U_l$, which can be described as homogenous flow. According to Weisman [5], the experimental calculations shows significant slip among phases, due constant momentum interactions, which is also called as slip ratio.

Friction loss: a loss of pressure or head, that occurs in pipe at near wall distance due to fluid's viscosity [6]. Many reasons are responsible for generation of friction loss, which is consider as minor loss, such as 1.Viscosity of fluid in motion, 2. Fluid molecules against each other 3. Fluid layers moving in different velocities 4. Inter-phase friction between gas-liquid phases 5. Channel inside surface roughness. However, the friction loss can be expressed as Darcy–Weisbach equation

$$h_f = \frac{f_D L\, v^2}{D\ 2g} \tag{1.2}$$

In other words, the friction loss can also be described as pressure loss formation

$$\Delta P = \frac{L\, f_D\, \rho v^2}{2D} \tag{1.3}$$

CHAPTER II

LITERATURE REVIEW

A single-phase flow or two-phase flow is a fluid system and studied in branch of fluid mechanics [7]. Here the word 'Phase' states the condition of matter that is solid, liquid, or gas. Hence, one can say the single-phase flow system contains an existence of single fluid at controlled space and at an instance of time. On the other hand, the two-phase system, which is one of the branches of multi-phase flow and heat transfer, contains existence of two fluids at same instance of time in at same space. Types of two-phase flows are gas-liquid, solid-liquid, gas-solid. In this research study, we are discussing on gas-liquid flows and their behavior in closed confined area changing spaces. Gas-liquid two-phase flow with its flow pattern, liquid holdup, and pressure gradient prediction in pipes is important to understand for design in various channels in industries. This understanding gives us information on global or microscale, while with current advancement in technologies, does provide an idea about the microscopic particle based behavior of two-phase systems. These experimental facilities needs massive amount of funds. However, recent development in computational solvers and high performing computing software helps to find these microscopic phenomena.

2.1 Single-Phase Flow

Single-phase flow associated pressure drop through abrupt area change is little reported in articles related to small channels. When an incompressible liquid flows through a sudden area of change, flow flows through an upstream section of the channel towards a larger section of channel

with sudden expansion causing eddy formations at a cross-section of area change of large section, which takes place as an irreversible process. The static pressure is most frequently found constant over the flow cross section Yoda [8], Wadle [9], Chen [10], Schmidt [11], Attou [12]., the expansion loss coefficients were approximately constant in the single-phase (water) flow. Thus by application of one-dimensional momentum and mechanical energy conservation equation:

2.1.1 Single phase in expansion channels

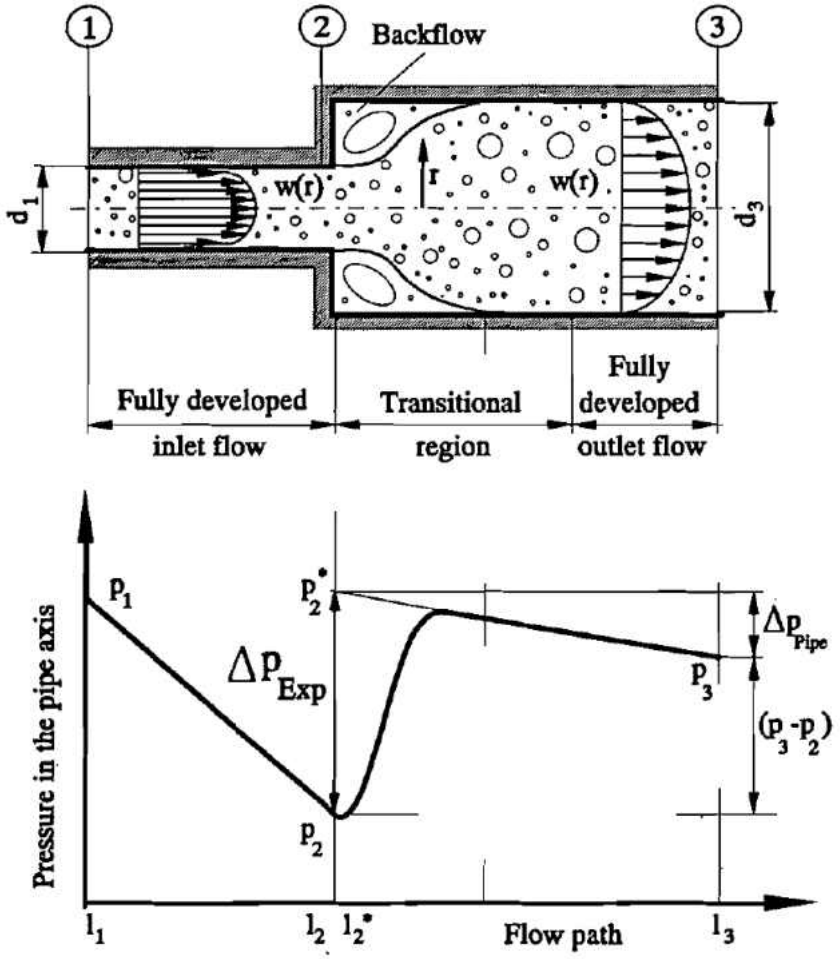

Figure 2.1. Idealized condition of streamlines and profile of static pressure in pipe sudden expansion [13]

The pressure drop in the expansion channels equations will be:

$$\triangle P_{sp,exp} = P_{2,1} - P_{2,3}, \qquad \triangle P_{sp,exp} = \triangle P_{exp,r} + \triangle P_{exp,i} \tag{2.1}$$

Where:

$P_{2,1}$ = Pressure measured from the flow area change to the small channel (See Figure 2.1)

$P_{2,3}$ = Pressure measured from the flow area change to the large channel (See Figure 2.1)

$\Delta P_{exp,r}$ = Reversible pressure drop in the expansion channels.

$\Delta P_{exp,i}$ = Irreversible pressure drop in the expansion channels.

$$\triangle P_{exp,r} = \frac{-{U_1}^2}{2} \times \rho_l \times (1 - {\sigma_{exp}}^2) \tag{2.2}$$

$$P_{exp,i} = k_e \times \rho_l \times \frac{{U_1}^2}{2} \tag{2.3}$$

Where:

k_e = Loss coefficient in the expansion channels = $(1 - \sigma)^2$

σ = Area ratio of Area A_1 and A_3

v_1 = Velocity in the small channel

A_1 = Area of the small channel

A_3 = Area of the large channel

Thus, the equation becomes:

$$\triangle P_{exp} = \rho_l \times {U_1}^2 \times \sigma_{exp}(1 - \sigma_{exp}) \tag{2.4}$$

According to I.Y.Chen et al. [14], similar to Schmidt [15] and Attou [12], and Bowers [7], the pressure difference of the expansion channels in single-phase flow can be studied. This pressure drop can be related to the kinetic energy of flow, which can be described into three parameters that are density velocity, and area ratio of channels.

2.1.2 Single phase in contraction channel

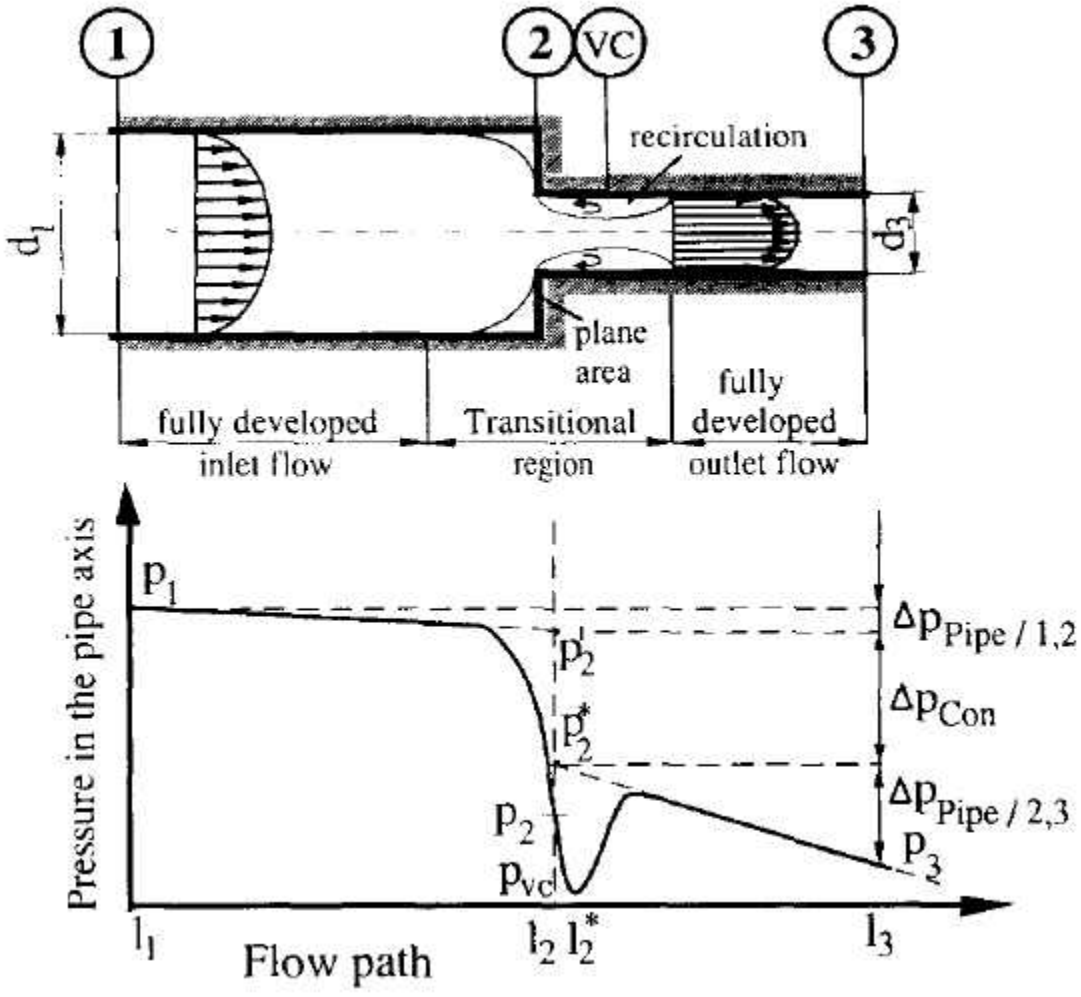

Figure 2.2. Idealized course of boundary streamlines and pressure in pipe contraction, along with effect of vena contracta (VC) Schmidt-Freidel, [11]

In above Figure 2.2 the first representation show the flow currents and streamlines and later part depicts the idealization of pressure profile. In contraction, the flow form larger section of channel advances towards smaller section of channel, at translational cross section the flow splits the internal wall and contracts to the jet with a slenderest cross section suddenly, while at the area change flow generates eddy formation with the negligible losses of mechanical energy.

Along with that, vena contracta takes place, when fluid enters to larger cross-section of channel, where fluid velocity reaches its maximum value, causing sudden drop of pressure, and can even form a hydrodynamic boundary layer flow until adaptation of new section. For pressure drop generalized equation can be considered as [8], [11]: can be formulated using properties of fluid such as velocity of fluid in small channel, kinetic energy correction factor, area ratio, and vena contracta coefficient, with momentum correction factor. The flat velocity formulation is assumed during vena contracta calculations. In terms of flow regimes, laminar flow through channel this kinetic energy correction factor is assumed as 2, while momentum correction factor is assumed as 1.33, but as the turbulent flow regime develops for the simplicity of correlation, both factors are assumed approximately as 1. Hence, the generalized equation can be considered as:

$$\triangle P_{sp,con} = P_{2,3} - P_{2,1} = \triangle P_{con,r} + \triangle P_{con,i} \tag{2.5}$$

By substituting all values:

$$\triangle P_{sp,con} = \rho_l \times \frac{-{U_1}^2}{2g} \times 1 - \frac{\beta_3 \sigma^2 {\sigma_c}^2 2\sigma_c + 2{\sigma_c}^2 {k_d}^2}{{\sigma_c}^2} \tag{2.6}$$

Where:

$$\sigma_{con} = \frac{A_c}{A_1}$$

The contration coefficient (C_c) in single-phase flow referred to Geiger's thesis [16]. The expression formula has shown as below:

$$\sigma_c = \frac{1 - \sigma_{con}}{2.08 \times (1 - \sigma_{con}) + 0.5371} \tag{2.7}$$

The equation for the laminar flow can be shown as (β = 2, k_d = 1.33):

$$\Delta P_{sp,con} = \frac{\rho_l \, {U_1}^2}{2} \times \left[\frac{1 - 2\,\sigma_c}{{\sigma_c}^2} + 2(1.33 - {\sigma_{con}}^2)\right] \tag{2.8}$$

For turbulent flows contraction co-efficient (C_c) is a function of area ratio and the Reynolds number In this case, flat velocity profiles or fully turbulent flow was postulated. The pressure drop in the contraction channel equations will be:

$$\Delta P_{sp,con} = \frac{\rho_l \, {U_1}^2}{2} \times \left[\left(1 - \frac{1}{\sigma_c}\right)^2 + 1 - {\sigma_{con}}^2\right] \tag{2.9}$$

Further, according to Geiger [16] reduced co-relation for pressure drop in contraction such as:

$$\triangle P_{sp,con} = \rho_l \times \frac{{U_1}^2}{2g} \times \left(\frac{1}{\sigma_c} - 1\right)^2 \tag{2.10}$$

Also, According to Chisholm [17] the single phase flow pressure drop in contraction channel is due to irreversible mechanical energy loss at Venna-Contracta ($P_{upstream}$) and pressure recovery towards downstream of the Venna-Contracta ($P_{downstream}$). The application of the contraction coefficient in Chisholm's report was slight different with Geiger [16]. The formulas can be described as below:

$$\triangle P_{sp,con} = \triangle P_{upstream} + \triangle P_{downstream} \tag{2.11}$$

Hence, the equation becomes:

$$\triangle P_{sp,con} = \frac{\rho_l {U_1}^2}{2}\left[\left(\frac{1}{\sigma_c \sigma_{con}}\right)^2 - \left(\frac{2}{{\sigma_{con}}^2}\right)\left(\frac{1}{\sigma_c} - 1\right) - 2\left(\frac{1}{\sigma_c} - 1\right)\right] \tag{2.12}$$

Where:

$$\sigma_c = \frac{1}{[0.639 \times (1 - \sigma_{con})^{0.5} + 1]}$$

2.2 Two-phase Flows

Two-phase flows consist of two different components of fluids or two distinct phases of same liquid in the form of a mixture, a certain number of models and correlations of proposed to calculate frictional pressure drop for the immediate area of change [18]. However, in spite of these developments, the knowledge paradigm for two-phase flow is limited.

According to Yoda [8], Hewitt's book. [19, 20], which says about the annular two-phase flows in various channels, and researchers Jenssen and Kervinen [21] and their consideration of pressure drop at 600 to 1400 PSIA in two phase flow, all these conducted two phase flow, air and water, experiments on abrupt flow area contraction and expansion in small channels. Two diameter of channels were used in there test. Along with the Reynolds number with their range from 870 to 12960, the flow quality was found between 1.9×10^{-3} and 1.6×10^{-2} in the two-phase flow experiment in the small diameter channel.

2.2.1 Two-phase in expansion channel

According to experimental results of Hewitt [7], Thome [22], Yoda [8], Awad [23], Beattie [18], Chen [14], Armand [24] for an incompressible liquid-gas two-phase flow mixture, with the assumption as flat velocities and identical void fractions, that is no sudden phase change, the following empirical co-relation is implemented:

$$\triangle P_{tp,exp} = P_{2,1} - P_{2,3} = \frac{\dot{m}^2}{A_1 A_3}\left(\frac{\sigma}{\rho_3'} - \frac{1}{\rho_1'}\right) \tag{2.13}$$

Where, In above expression we have:

$$\rho' = \left[\frac{1-x^2}{\rho_l(1-\alpha)} + \frac{x^2}{\rho_g \alpha}\right]^{-1}$$

According to Lahey and moody [25], the reversible pressure drop for two-phase expansion channels is:

$$\triangle P_{tp,exp,R} = P_{2,3} - P_{2,1} = \frac{\dot{m}^2 \rho_h}{2\rho_l A_1 A_3}\left(\frac{1}{\rho_3''^2} - \frac{\sigma_{con}{}^2}{\rho_1''^2}\right) \tag{2.14}$$

Where in above equation we have:

$$\rho_h = \left(\frac{x}{\rho_g} + \frac{1-x}{\rho_l}\right)^{-1}$$

And,

$$\rho'' = \left[\frac{(1-x)^3}{\rho_l^3(1-\alpha)^2} + \frac{x^3}{\rho_g^2 \alpha^2}\right]^{-1/2}$$

Also,

$$x = \frac{\dot{m}_g}{\dot{m}_g + \dot{m}_l}$$

In above co-relation by Lahey, to calculate pressure drop, empirical relationship is required for $\alpha \; and \; x$, and thus based on experimental conditions, the pressure drop cannot be based on pure theory.

In addition, based on satisfactory data of Thome [22] the following co-relation proves the validation of pressure drop across sudden expansion, assuming equal void fractions among phases, and incompressibility of flow.

$$\triangle P_{tp,exp} = \phi_{l,exp} \times \triangle P_{l,exp} \tag{2.15}$$

Where:

$\Phi_{l,exp}$ = Two-phase flow multiplier at all liquid condition in expansion channel

$\Delta P_{l,exp}$ = Pressure drop at all liquid condition in expansion channel

$$\triangle P_{l,exp} = \frac{\dot{m}^2}{\rho_l A_1 A_3} \times (\sigma_{exp} - 1) \tag{2.16}$$

$$\phi_{l,exp} = \frac{\rho_l}{\rho'} \tag{2.17}$$

Hence, we have:

$$\triangle P_{tp,exp} = \frac{\dot{m}^2}{2A_1}\left[\frac{1}{A_3} - \frac{1}{A_1}\right]\left(\frac{2\sigma}{\rho'} - \frac{\rho_h}{\rho''^2}\right) \tag{2.18}$$

Where:

$\dot{m}$ = Mass flow rate at small channel

ρ_l = Density of liquid

ρ' = fictitious mixture densities

ρ_g = Density of gas

The homogeneous flow assumption was also applied in Yoda's [8] experimental report. Due to the assumption the velocity of liquid and gas were same, therefore slip ratio equaled to one.

For ideal annular flow situation, Zivi [26] proposed the minimum entropy generation assumption; the outcome of the slip ratio was different. The slip ratio expression was:

$$S = 0.7 \times \left(\frac{\rho_l}{\rho_g}\right)^{\frac{1}{3}} \tag{2.19}$$

Based on the experimental calculations by Wadle [9], proposed constant minor loss coefficient in different fluid applications. The author also proved the coefficient for steam and

water as 0.667, and similar coefficient for application of air and water proved to be 0.83. According to his experimental evaluations, the Total two–phase pressure drop equation shown as,

$$\triangle P_{tp,exp} = (1 - {\sigma_{exp}}^2) \times \left(\frac{\dot{m}^2 k}{2A_1^2}\right)\left(\frac{(1-x)^2}{\rho_l} + \frac{x^2}{\rho_g}\right) \tag{2.20}$$

The non-friction loss mechanical energy equation for two-phase flow pressure drop in sudden enlargement pipes, according to Thome [22]. Void fraction behavior and pressure drop calculations show direct proportionality. The derived equation is:

$$\triangle P_{tp,exp} = \frac{\dot{m}^2}{\rho_l A_1 A_3}\left[\left[\frac{(1-x)^2}{1-\alpha_1} + \frac{\rho_l x^2}{\rho_g \alpha_1}\right] - \sigma_{exp}\left[\frac{(1-x)^2}{1-\alpha_2} + \frac{\rho_l x^2}{\rho_g \alpha_2}\right]\right] \tag{2.21}$$

If the void fractions in above co-relation assumed to be equal then, following result holds validation:

$$P_{tp,exp} = \frac{\dot{m}^2 V_l}{\rho_l A_1 A_3}\left(1 - \sigma_{exp}\right)\left[\frac{(1-x)^2}{1-\alpha} + \frac{\rho_l x^2}{\rho_g \alpha}\right] \tag{2.22}$$

If the void fraction in above equation (24) is given by co-relation of Kawahara et al [27], then that void fraction equation is:

$$\alpha = \frac{0.03\beta^{0.5}}{(1 - 0.97\beta^{0.5})} \tag{2.23}$$

Schmidt and Friedel in 1997 [13], calculated complex formula, using an annular-mist flow model accompanied with mass and momentum balance. The model checked against the experimental data of gas-liquid (air-water) two-phase flow, by including all physical parameters:

$$\Delta P_{tp,exp} \tag{2.24}$$

$$= \frac{G\left[\frac{\sigma_{exp}}{\rho_{eff}} - \frac{{\sigma_{exp}}^2}{\rho_{eff}} - f_{exp} \times \rho_{eff}\left(\frac{x}{\rho_g \alpha} - \frac{(1-x)}{\rho_l(1-\alpha)}\right) \times \left(1 - \sqrt{\sigma_{exp}}\right)^2\right]}{1 - \Gamma_{exp}(1-\sigma)}$$

Where, the terms in above equation are:

$$\frac{1}{\rho_{eff}} = \frac{x^2}{\rho_g \alpha} + \frac{(1-x)^2}{\rho_l(1-\alpha)} + \frac{\alpha_E \rho_l (1-\alpha)}{1-\alpha_E} \times \left[\frac{x}{\rho_g \alpha} - \frac{(1-x)}{\rho_l(1-\alpha)}\right]^2$$

$$\alpha = 1 - \frac{2(1-x)^2}{1 - 2x + \sqrt{1 + 4x \times (1-x) \times \left(\frac{\rho_l}{\rho_g} - 1\right)}}$$

$$\alpha_E = \frac{1}{S}\left[1 - \frac{(1-x)}{1 - x(1 - 0.05 \times We^{0.27} \times Re^{0.05})}\right]$$

$$We = G^2 x^2 \times \frac{d(\rho_l - \rho_g)}{{\rho_g}^2 \sigma}$$

$$Re = \frac{G(1-x)d}{\mu_l}$$

$$\Gamma_{exp} = 1 - {\sigma_{exp}}^{0.25}$$

$$f_{exp} = 4.9 \times 10^{-3} \times x^2 (1-x)^2 \times \left(\frac{\mu_l}{\mu_g}\right)^{0.7}$$

In 1959 Romie et.al. [28], published a report in which, they derived the expression for sudden expansion, for two-phase flows pressure change. Thus foe flat velocities, the void fraction is unchanged. Hence, the expression is given further:

$$\Delta P_{tp,exp} = \frac{-G \times \sigma_{exp}(1-\sigma_{exp})}{\rho_l}\left[\frac{(1-x)^2}{(1-\alpha)} + \frac{\left(\frac{\rho_l}{\rho_g}\right) \times x^2}{\alpha}\right] \tag{2.25}$$

Further, Richerdson [29] streamlined the energy balance model and implicitly assumed that the pressure recovery is proportional to the kinetic energies of the phases. Hence further yielding:

$$\Delta P_{tp,exp} = -\frac{G \times \left(1 - {\sigma_{exp}}^2\right)}{2} \times \left[\frac{\sigma(1-x^2)}{\rho_l(1-\alpha)}\right] \tag{2.26}$$

2.2.2 Two-phase in contraction channel

The two-phase pressure drops occurred in sudden contraction channels is more complicated to understand compared to two-phase flow sudden expansion channel pressure drop. Occurrence of vena contracta is more during change in area of contraction channel, which is proven by Attou [12], Al`Ferov [30], Guglielmini [31], Jansen [21], Chisholm [32], Armand [24] further stating that this Venna-Contracta occurs at just after area change towards downstream of flow. Schmidt and Friedel [15] perform careful experimental investigation over single-phase flow. The author proposed absence of Venna-Contracta (VC) during area change in contraction channel flow, although the measurements were not based on the dip and the recovery in the axial pressure profile. In contrast, Guglielmini [31] presented their findings based on implication of vena contracta.

According to Ghaisassan et al. [33], development of pressure drop phenomena based on vena contracta released downstream of the channels. This prediction also modeled using assumptions such as incompressible two-phase flow, with flat velocities, and unchanged void fractions.

$$\triangle P_{tp,con} = \frac{\dot{m}^2}{{A_1}^2}\left\{\frac{\rho_h}{2\rho^2}\left(\frac{1}{\sigma_c} - {\sigma_{con}}^2\right) + \frac{1}{\rho}(1-\sigma_c)\right\} \tag{2.27}$$

Where in above equation, value for ρ'' is:

$$\rho'' = \left[\frac{(1-x)^3}{\rho_l^3(1-\alpha)^2} + \frac{x^3}{\rho_g^2\alpha^2}\right]^{-1/2}$$

With the homogeneous flow, consideration due to effective mixing the pressure drop related to contraction channel leads to:

$$\Delta P_{tp,con} = \triangle P_{l,con} \times \phi_{l,con} \tag{2.28}$$

Here we have:

$$\Delta P_{l,con} = \frac{\dot{m}^2}{2\rho_l {A_1}^2}\left[\left(\frac{1}{\sigma_c} - 1\right)^2 + (1 - {\sigma_{con}}^2)\right]$$

And,

$$\phi_{l,con} = \left(1 + \frac{x(\rho_l - \rho_g)}{\rho_l}\right)$$

Hence the equation (31) becomes,

$$\Delta P_{tp,con} = \frac{\dot{m}^2}{2\rho_l {A_1}^2}\left[\left(\frac{1}{\sigma_c} - 1\right)^2 + (1 - {\sigma_{con}}^2)\right] \times \left(1 + \frac{x(\rho_l - \rho_g)}{\rho_l}\right) \tag{2.29}$$

The above model holds validation only if the assumptions related to the model such as flow of two-phase and single phase takes same place in particular channel at same location and results in identical contraction ratio, also Geiger [16] shows, there is a particular Contracta coefficient proves the validation for the above model which is,

$$\sigma_c = 1 - \frac{(1 - \sigma_{con})}{2.08 \times (1 - \sigma_{con}) + 0.5371} \tag{2.30}$$

Collier and Thome [22], speculated two-phase flow total pressure drop by performing experimental analysis over certain set of micro-channel. Their assumption is homogeneous model, by considering Geiger's Contracta coefficient, which is:

$$\triangle P_{tp,con} = \frac{\dot{m}^2}{2\rho_l A_1}\left[\left(\frac{1}{\sigma_c}-1\right)^2 + (1-{\sigma_{con}}^2)\right]\left[1+x\left(\frac{\rho_l}{\rho_g}-1\right)\right] \tag{2.31}$$

The momentum and mass transfer balance constructed, Schmidt and Friedel [11] developed a new pressure change model for sudden contraction that incorporates all of the relevant boundary conditions. In this model all the relevant physical parameters, which were also included in their sudden expansion channels research. The test sections inlet tube diameters in the range of 44.2–72.2 mm, and with outlet tubes in the range of 17.2–44.2 mm. Hence, with comprehensive study, the co-relation for incompressible adiabatic flow, the equations for pressure drop in sudden contraction channels is given as:

$$\Delta P_{tp,exp} \tag{2.32}$$

$$= \frac{G^2\left[\frac{\sigma_{con}}{\rho_{eff}} - \frac{{\sigma_{con}}^2}{\rho_{eff}} - f_{con}\times\rho_{eff}\left(\frac{x}{\rho_g\alpha} - \frac{(1-x)}{\rho_l(1-\alpha)}\right)\times\left(1-\sqrt{\sigma_{con}}\right)^2\right]}{1-\Gamma_{con}(1-\sigma)}$$

Where, the terms in above equation are:

$$\frac{1}{\rho_{eff}} = \frac{x^2}{\rho_g\alpha} + \frac{(1-x)^2}{\rho_l(1-\alpha)} + \frac{\alpha_E\rho_l(1-\alpha)}{1-\alpha_E}\times\left[\frac{x}{\rho_g\alpha} - \frac{(1-x)}{\rho_l(1-\alpha)}\right]^2$$

$$\alpha = 1 - \frac{2(1-x)^2}{1-2x+\sqrt{1+4x\times(1-x)\times\left(\frac{\rho_l}{\rho_g}-1\right)}}$$

$$\alpha_E = \frac{1}{S}\left[1 - \frac{(1-x)}{1-x(1-0.05\times We^{0.27}\times Re^{0.05})}\right]$$

$$We = G^2x^2\times\frac{d(\rho_l-\rho_g)}{{\rho_g}^2\sigma_{con}}$$

$$Re = \frac{G(1-x)d}{\mu_l}$$

$$\Gamma_{con} = 0.77 \times \sigma \, (1 - {\sigma_{con}}^{0.306})$$

$$f_{con} = 5.2 \times 10^{-3} \times x^{0.1}(1 - x) \times \left(\sigma_{con} \times \frac{\mu_l}{\mu_g}\right)^{0.8}$$

Apart from this, Balakrishsna et al. [34] from previous data of Mudawar et al. [35], studied flow patterns during the simultaneous flow of high viscous oil and water. Using the sudden contraction and expansion in a horizontal duct, it is illustrated that these abrupt changes in cross-section have a noteworthy impact on the downstream phase dispersal of lube oil–water flow. Their observation, proposed simple technique to create main flow as well as a method to avert pipe wall entangling throughout the transportation of such oil. The pressure outlines from the wall, are discovered self-regulating of liquid viscosity and the loss coefficients are identified as independent of flow patterns in both the cases.

2.3 Void Fraction study

Void fraction (α) is considered as critical parameter of several others, which are important to determine the flow quality and presence of individual phases in two-phase flow. To model pressure drop in terms of analytical method or experimental method, void fraction plays an important role. Identical to void fraction, while modeling the two-phase flow computationally, volume fraction that defines the presence of individual phases in fluid continuum mathematically. Hence one can say freely, void fraction in experimental analysis, is equal to volume fraction in computational analysis.

According to Ghajar and Tang [4], 54 void fractions correlations were studied for upward and downward vertical pipes and horizontal pipe two-phase flows. Based on their analysis, many void fractions were limited in terms handling a wide variety of datasets. Ghajar's recent correlation

with woldesemayat [36] show better drift flux model in terms of void fraction co-relations. This is represented here:

$$\alpha = \frac{U_{sg}}{C_0\left(U_{sg} + U_{sl}\right) + u_{gu}} \tag{2.33}$$

Where:

$$C_0 = \frac{U_{sg}}{U_{sg} + U_{sl}}\left(1 + \left(\frac{U_{sl}}{U_{sg}}\right)^{\left(\frac{\rho_g}{\rho_l}\right)^{0.1}}\right)$$

$$u_{gu} = 2.9(1.22 + 1.22\,Sin\,\theta)^{\frac{P_{atm}}{P_{sys}}}\left(\frac{g \times D \times \sigma\,(1 + \cos\theta)\left(\rho_l - \rho_g\right)}{\rho_l^2}\right)^{0.25}$$

The leading equation constant u_{gu} carries the unit of $m^{-0.25}$. Also the σ can be $\sigma_{con}\ or\ \sigma_{exp}$. Although, while determining the co-relations, some assumptions were made, such as in experimental pressure drop, where fractional and acceleration contributions are assumed negligible, is then used for determining the void fraction from $\Delta P = \left[\rho_g\,\alpha + \rho_l(1-\alpha)\right]gH$.

2.4 CFD study of two phase flow in channels with Eulerian approach

Bharamara et al [37], predicts pressure drop for modeling heat transfer co-efficient using Computational Fluid Dynamics analysis. Their model is of CFD study of two-phase flow of refrigerants inside a horizontal tube with inner diameter of 0.0085 m and length of 1.2 m is approved using homogeneous model under adiabatic conditions. The refrigerants considered are R22, R134a and R407C. With the application of homogenous model, that is slip ratio = 1 average properties are obtained for each of the refrigerants that is considered as single phase pseudo fluid.

The result datasets match well by separated flow correlations, and Muller – Steinhagen and Heck correlation [38].

Raul et al. [39], studied computationally to determine the pressure drops caused by abrupt flow area expansion/contraction in small circular pipes for two-phase flow of air and water mixtures at room temperature and near atmospheric pressure. Their study involves Eulerian 2 fluid approach coupled with realizable $k-\epsilon$ model turbulence model. The experimental data has been carried from Yoda et al. [8]. First computational analysis is done with single-phase phenomenon, and after that, two-phase flow analysis is performed. The results show excellent agreement between computational and experimental analysis.

Dash et al. [40], performed numerical investigation on Two-phase flow pressure drops through thin and thick orifices with air–water flows in horizontal pipes. A similar model, which is used in this research, is used along with combination of $k-\epsilon$ realizable turbulence model. The operating conditions insures the gas and liquid superficial velocity ranges, that are superficial velocity of gas (U_{sg}) = 0.3–4 m/s and superficial velocity of gas (U_{sl}) = 0.6–2 m/s, respectively. For single-phase the local liquid Reynold's number appears to be 3000 to 200000, from which the two-phase multiplier determine to compare with experimental calculations. The experimental and computational data shows good agreement in there article.

Patro et al. [41] develops numerical simulation model for two-phase gas-solid flows using kinetic theory of granular flows (KTGF), for inter-particle collisions in the nozzle for solid particles. This model further coupled with multiphase Eulerian model, and the scalar quantities are solved using RANS $k-\epsilon$ turbulence model. In their findings, trappings of solid particles to the

gas flow considerably restrain the gas turbulence in the nozzle as well as the jet flows. Sufficient particles subdue the turbulence, whereas coarse particles enhance it.

On the other hand, Raul et al. [42] computed the mathematical pressure drop and pressure profiles, for two-phase flow of oil-water emulsions, for which the experimental data was gathered from Pal et al. [43]. Their model is Eulerian 2 fluid model coupled with RANS $k - \epsilon$ model, which updates the fluid viscosity with iterations and capture the individual turbulence in both the phases. They found out, the loss coefficients for the emulsions are found to be sovereign of the concentration and type of mixtures. The mathematical results are validated against investigational data from the previous literature of Pal et al. and are found to be in good agreement.

Rusche, [44], developed a two-fluid (Euler-Euler) methodology at Imperial College is adapted to high phase fractions. Additional models for the inter-phase momentum transfer, which consist of virtual mass, drag and lift, and turbulence for closure were implemented. For evaluation of the methodology is made with reference to experimental data for gas-liquid bubbly flow in an abrupt cross-section change of a circular pipe and in a plane-mixing layer. The computational results found to be assimilating with respect to experimental results. This in future, it is recognized as TwoPhaseEulerfoam.

Ali Abaas [45], studied the links extrapolation for two phase flow pressure drops in a horizontal translucent pipe, (78 mm) diameter by using gas-liquid mixtures at an atmospheric pressure. The experimental data of friction pressure drop (pressure gradient) were presented as friction pressure drops in the form of two-phase friction multipliers where compared with the correlations of Lockhart and Martinelli, Chenoweth-Martin and homogeneous flow theory, and found out to be the homogeneous model as agreeable which is S = 1.

The experiments by Kartushinsky et al. [46], shows that there should be special measures required to generate experimental data related to Eulerian-Eulerian multiphase flow model. They investigated the effects of flow direction (upward or downward) and mean concentration on radial particle distribution and on the mean axial velocities of both particles and fluid in flow. Similar to this research, to get reasonable values between experimental outcomes and model calculations, a lift force term had to be included; core peaking in up-flow and wall peaking in down-flow result from it. There findings are the difference of mean particle and fluid local velocities are decreasing towards near wall in both upward and downward flows.

2.5 CFD study of two phase flow in channels with Lagrangian approach

ALE, which is Arbitrary Lagrangian-Eulerian, is on other hand allows us to find the presence of individual phasic existence by using integral equations, and there inter-dependence on the other vectorial and scalar quantities such as pressure, velocity, and turbulence. This method is useful to determine local existence of phases, with respect to motion of phases, across fluid continuum.

Anjos [47], presented his thesis with numerical simulations in two-phase flows using 3 dimensional Arbitrary Lagrangian-Eulerian formulation (ALE) and the Finite Element Method (FEM), for gas-liquid interface. The Lagrangian description explicitly defines the two-phase boundary position by a set of interrelated nodes that confirms a sharp illustration of the boundary, including the role of the surface tension. This leads to moderate computing cost and accurate results. With the experimental results found in the literature, their model is validated with excellent agreement.

Szczukiewicz et al. [48], created a review in two-phase flow boiling, by representing previous researcher's co-relations, and providing self-developed Computational Fluid Dynamics simulation, for which it's not accessible to generate results through experimental analysis. The mathematical models of boiling flows accomplished by the authors shows the suitable modeling of the thermal inertia of the liquid film confined amongst an elongated bubble and the channel wall, and of the flow recirculation in the liquid slug between two bubbles, offers very valuable local information on the heat transfer coefficient.

The study created by Ubbink [49], adds to the field by presenting a method adaptive to capturing a moving interface between two immiscible fluids on an arbitrary Eulerian mesh. The two fluids are showed as a single flow field with a fluid property jump at the interface. A function of volume fraction indicator is used to spot the discretized fluids and the interface is defined as the transitional region between the fluids. A finite volume discretization is applied to the transport equations. The author presented several test cases show the simplicity and precision with which this method can be used to predict the two-phase flow performance of immiscible fluids.

CHAPTER III

EXPERIMENTAL FACILITY AND PROCEDURE

3.1 Experimental Facility.

An experimental facility for our test requires some specific instruments to complete this study. In this experiment, pressure drop, mass flow rate, temperature difference, Reynolds number, so forth are the significant parameters for analyzing and understanding the behaviors of the phases flow in the contraction and expansion channels shows that the closed-flow loop system was used to gather the data in the experiment. The deionized water storage tank, standard duty gear pump, mass flow meter, thermocouples, contraction and expansion channels, pressure transmitters, static pressure transducers, data acquisition system, heat exchanger and pipes system.

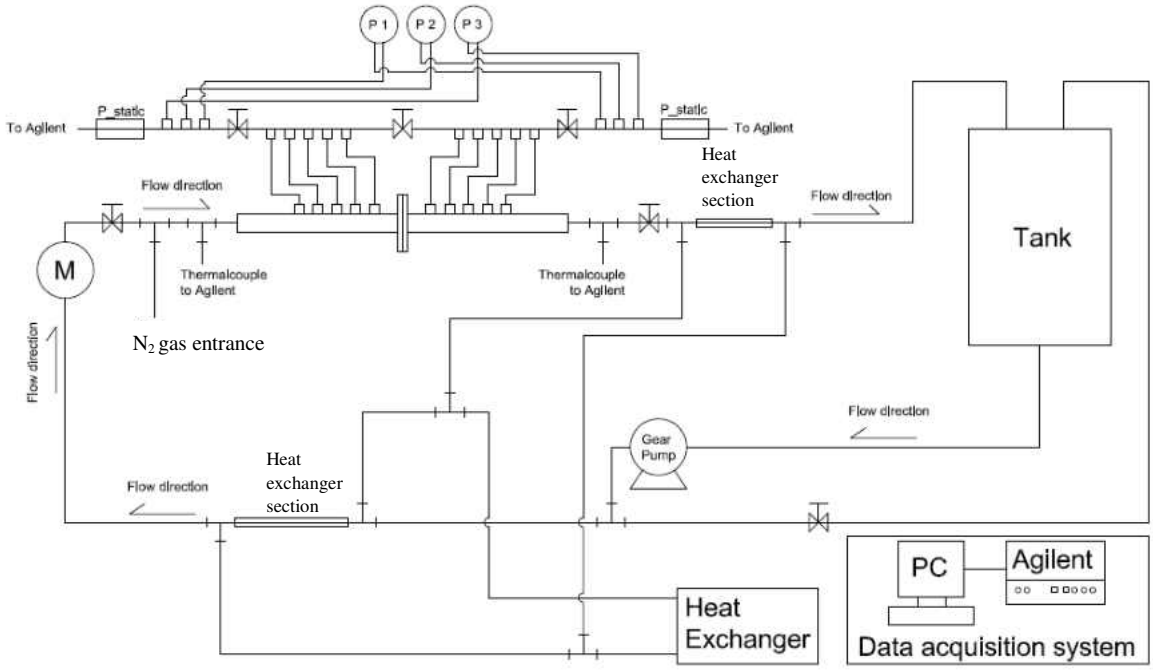

Figure 3.1: Schematic diagram of the experimental system

3.2 Experimental setup

The cylindrical tank, which is made of polyvinyl carbonate (PVC), which has a diameter of 0.25 meter, and height of 0.3048 meters, has a capacity of 15 liters of holding any liquid, is used for storing de-ionized water. To avoid mechanical losses during energy consumption while delivering liquid, and to keep same power output, the tank was installed 1 meter above the ground level of the pump. A standard duty gear pump, configured to deliver flows up to 55 GPM at 100 PSI or 6.9 bars, is preferred to use for efficient circulation of water. The mass flow rate controlled by mass flow meter of liquid in the test system. For better accuracy, Rosemount manufactured CMFS010M model of micro mass flow sensor decided to use for the experimental analysis. There are a specific set of thermocouples for measurement of temperature change across test sections, to monitor and maintain the constant room temperature conditions.

In Figure 3.2 the top part of picture shows the aluminum test section with diameter 0.5 inches (0.0127 meters), 0.375 inches (0.009525 meters), and 0.14 inches (0.003556 meters), and the bottom part shows 0.19 inches (0.004826 meters), and 0.315 inches (0.008001 meters) [50]. During the experimental analysis, test section of diameter 0.5 inches retained as constant, regardless of assessment of the contraction or expansion phenomenon. Figure 3.3. The schematic of the test sections with upstream 0.5 inches. - diameter (Left side) and downstream 0.14 inches. – diameter (Right side)., illustrates the configuration of the test section, where the left side is the inlet for particular fluid or mixture of fluids, whereas the right side is the outlet where the downstream flow is measured. To generate the pressure profile by acquiring data at local pressure, ten pressure taps were installed in the bottom of the test section, and the distance between two taps approximately 1 inch. Hence, the data was acquired at -5, -4, -3, -2, -1, 1, 2, 3, 4, 5 inches. Moreover, 1/8 inches flexible PVC channels are connected with taps. To collect the accurate and efficient data, bubbles are not allowed in the internal flexible PVC channels before the fluid are introduced into the test section.

Rosemount manufactured pressure transmitters for measuring the pressure across test sections installed, from which this data the pressure profile and pressure drop calculated. Static pressure transducers for conversion of analog mechanical signal to digital electrical signal, data acquisition system for recording of data, heat exchangers for maintaining a constant temperature, and pipe system for connections.

Figure 3.2. Various diameters test sections

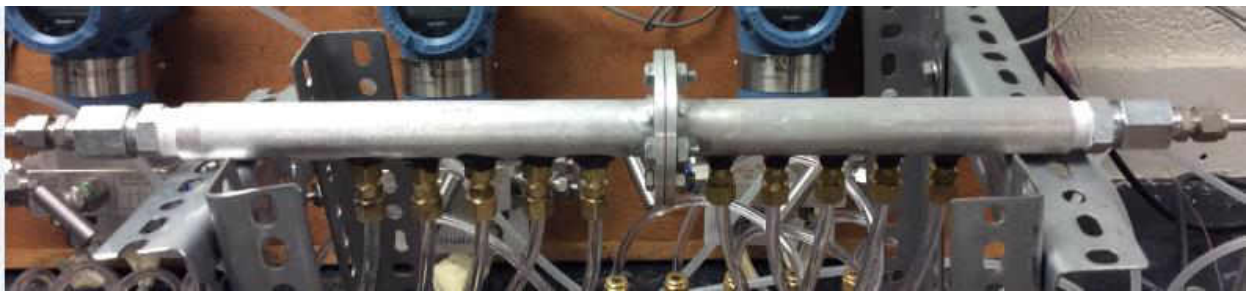

Figure 3.3. The schematic of the test sections with upstream 0.5 inches. - diameter (Left side) and downstream 0.14 inches. – diameter (Right side).

Isothermal conditions applied to these steady-state analysis experiments for not causing a sudden phase change, resulting in irregularities in experimental data. To maintain these constant temperature conditions, heat exchangers were installed to keep the temperature of the fluid almost constant during the entire experimental period. In this case, two heat exchangers applied to the system. As per schematic diagram, one of them installed before the inlet and test section, to get

accurate heat exchanging isothermal conditions, and another one installed at downstream outlet section for moving extra heat, which generated by fluid passing through the test section.

3.3 Experimental procedure

To run entire test facility as closed loop system, it is required to check the leakage in the connections, devices and the test section itself. This leakage proofing ensures the efficiency by eliminating undesired mechanical losses. DPG-107 Dwyer digital pressure gauge (Figure 3.4) and T-970 Ametek pneumatic hand calibration air pump are used for checking the system, to prevent the possibility of flow loop leakage. Hand air calibration pump allows pressure range from 0 to 40 bar. The inlet valve before the mass flow meter and outlet valve before heat exchanger closed. Thus, the hand pump connected to gas flow inlet continuously provide steady pressure buildup until it reached its maximum value on the gauge. At this moment, the pressure is maximized within the test section due to blockage at pressure valves; this makes whole test section acted as a closed system. After observation of given period, if the pressure value on gauge does not changes, the test section is considered as leakage proof, and the test is successfully carried out.

After the leakage test in test section and other counterparts, the entire test assembled to create closed-loop facility. This system further used for passing the flow trial to remove bubbles, for reducing errors. While data measurement, like bubbles, may generate undesired effects on reading the results.

Figure 3.4. The combination of DPG-107 Dwyer digital pressure gauge and A T-970 Ametek pneumatic hand air calibration pump

3.3.1 Single-phase flow experimental procedure

The properties and behaviors of the single-phase flow observation was a step before the application of the two-phase flow. Single-phase (only water) flow is developed in the facility to perform experiment related to single-phase flow, and the data is gathered using pressure transducers and Agilent data acquisition system, which collects data from the micro mass flow meter, thermocouples, and two static pressure transducers; this further converts the data in Excel format using required software process. The liquid mass flow rate of 0.005 kg/s, 0.01 kg/s, 0.015 kg/s, 0.0175 kg/s, 0.02 kg/s, 0.0225 kg/s, 0.0245 kg/s, 0.0265 kg/s, 0.0285 kg/s, and 0.03 kg/s. Periodically provided as an input to the test section. After every input, the system kept ideally running for five minutes to make flow stable. The similar procedure followed for single-phase flow for contraction channel, after reversing the sides of the test sections [50].

3.3.2 Two-phase flow experimental procedure

The gas entrance valve was opened to pass the required nitrogen gas mass flow rate through the test section. Five gas mass flow rates, which units is Standard liter per minutes (SLPM), were applied in the experiment: 0.025 (≈ 0.00048 kg/s), 0.1 (≈ 0.0019 kg/s), 0.5 (≈ 0.0095 kg/s), 1(≈ 0.019 kg/s), 1.5 (≈ 0.028 kg/s). Each giving gas flow rate remained constant and run with the liquid mass flow rate of 0.005 kg/s, 0.01 kg/s, 0.015 kg/s, 0.0175 kg/s, 0.02 kg/s, 0.0225 kg/s, 0.0245 kg/s, 0.0265 kg/s, 0.0285 kg/s, and 0.03 kg/s. individually. The data of the water behaviors were still collected and presented by Agilent software; the gas performances were received by HyperTerminal which menu on Microsoft Windows. After finishing the one test section cycle with all dataset collection, the test section was flipped to receive the different section data for either contraction or expansion. The test section changed one by one after the process was done, and so on so forth.

CHAPTER IV

COMPUTATIONAL/MATHEMATICAL MODELING

Regarding single-phase flow a single-fluid model is developed. Which consist of conservation of momentum and continuity equations in conservative form. Eulerian-Eulerian multi-fluid approach is implemented which contemplates both phases as intersecting continuum within each computational cell of the domain. The domain also holds equations for volume fractions of both phases as dispersed and continuous. However, due to mathematical constraints, the volume of phases cannot be occupied at specific time and controlled volume continuum, hence the concept of phasic volume fraction is used. The flow field is further modeled with Reynolds Stress (5-equation) Model for turbulence regime, using near wall pressure gradient treatment. State of Art computational solver software is used for analysis.

4.1 Governing Equations

Multiphase flows show uncertainty in exact locations of particles of each particle as their prime characteristics at any particular time. For example, suspensions of air or solid particles in water flow, which cannot efficiently analyze at given time and space continuum, hence averaging over time and space provides natural speculations of particles and forces acting on them, calling them as ensemble averaging. This time and space in other words controlled volume average can consider as speculated average. This further justifies steady flow or homogeneous flow analysis.

Using this principle, experiments performed to achieve near steady-state phenomenon in two-phase flow. Furthermore, according to Seito [51], following assumptions are made:

- All materials considered for computational analysis are Newtonian, viscous, and incompressible.
- Physical properties of these materials are considered constant throughout fluid flow analysis.
- For two-phase analysis, there is no mass transfer between two phases. Also for single-phase flow, no mass transfer is assumed.
- For the turbulence regime of flow, Reynolds stress model considered as for the behavior of fluids during flow analysis.
- The surface tension forces neglected for two-phase flow modeling, and pressure for both phases are considered as it for any elemental controlled volume at any cross-section.
- As the experimental analysis achieved under STP (Standard Temperature and Pressure) conditions, no energy equation added while modeling of flow.

4.2 Single phase flow modeling

With the above assumptions, According to Spalding [52], Lauder [53], Gibson [54], Chorlin [55], for single-phase flow analyses following equations are considered:

General Single-phase continuity equation:

$$\frac{\partial \rho}{\partial t} + \nabla . (\rho \vec{u}) = 0 \tag{4.1}$$

In this case, we are considering 2-dimensional axis-symmetric geometries hence the continuity equation becomes:

$$\frac{\partial \rho}{\partial t} + \frac{\partial (\rho u_x)}{\partial x} + \frac{\partial (\rho u_r)}{\partial r} + \frac{\rho u_r}{r} = 0 \tag{4.2}$$

The equation of conservation of Momentum for single-phase flow:

$$\frac{\partial}{\partial t}(\rho \vec{u}) + \nabla.(\rho \vec{u}\vec{u}) = -\nabla P + [\bar{\bar{\tau}}] + \rho \vec{g} \tag{4.3}$$

where the stress tensor is given by:

$$\bar{\bar{\tau}} = \mu \left[[\nabla \vec{u} + \vec{u}^T] - \frac{2}{3} \nabla . \vec{u} I \right] \tag{4.4}$$

4.3 Two-phase (Multiphase) flow modeling

Advances in computational fluid mechanics have provided the intricate details of dynamics of multiphase flows. Currently, there are two approaches for calculations of multiphase flows:

- Euler-Euler approach.
- Euler-Lagrangian approach.

In the Euler-Euler approach, the different phases are treated mathematically as interpreting continua [56]. Since the control-volume of a phase cannot be occupied by the other phases, the concept of phasic volume fraction is introduced. These volume fractions are assumed continuous functions of space and time, and their algebraic sum is equal to one. Conservation of equations for each phases are derived to obtain a set of equations, which have a similar structure for all phases. These equations are closed by providing constitutive relations that are obtained from empirical information for example if the granular flows are provided then, application of kinetic theory.

For the numerical modeling of two-phase flow, considering above assumptions, we are considering Nitrogen as gaseous secondary phase, which is phase g, and water as liquid primary

phase that is phase l. The governing equations of Eulerian-Eulerian multiphase model holds true for liquid as well as gaseous phase. In other words these equations are also written in terms of gaseous phase with suffix g, but due to void fractions of gaseous phase having value less than 0.11, and due to major phase is represented as liquid, hence the following equations are preferred to be represented with liquid notations. Thus, According to Drew [57], Lahey [58], Gidaspow [59], Gibson & Lauder [54], Yeoh [56] the governing equations for both phases are considering analysis done by:

$$\frac{\partial}{\partial t}(\alpha_l \rho_l) + \nabla.(\alpha_l \rho_l \vec{u_l}) = 0 \tag{4.5}$$

Here void fraction equation is,

$$\alpha_l + \alpha_g = 1 \tag{4.6}$$

Momentum equation:

$$\frac{\partial}{\partial t}\left(\alpha_l \rho_l \vec{u_l}\right) + \nabla.\left(\alpha_l \rho_l \vec{u_l}\vec{u_l}\right) = -\alpha_l \nabla P + \nabla.\left(\bar{\bar{\tau}}\right) + \alpha_l \rho_l \vec{g} \tag{4.7}$$

$$+M_l^d + M_l^{VM} + M_l^L$$

In above equation, the last three 'M' terms, will be changed from positive sign to negative sign. This is described in details, further in equations.

Where the liquid phase, as well as gas phase stress tensor, is:

$$\bar{\bar{\tau}} = \alpha_l(\mu_l + \mu_{t,l})(\nabla \vec{u_l} + \nabla \vec{u_l}^T) \tag{4.8}$$

Moreover, for the gaseous phase the equation changes to:

$$\bar{\bar{\tau}} = \alpha_g(\mu_g + \mu_{t,g})(\nabla \vec{u_g} + \nabla \vec{u_g}^T) \tag{4.9}$$

In above momentum equation the terms related to momentum transfer expressed as, the Drag Force:

$$M_l{}^d = -M_g{}^d = \left(\frac{3}{4d_g}\right)\alpha_g.\rho_l.C_D.|\vec{u_g} + \vec{u_l}| \times (\vec{u_g} + \vec{u_l}) \tag{4.10}$$

In above equation the coefficient of Drag, as per Neumann [60], is dependent on Reynolds number, which is as follows:

$$C_D = \begin{cases} 24 \times \left(\dfrac{1 + 0.15 \times Re^{0.687}}{Re}\right), & if Re \leq 1000 \\ C_D = 0.44, & if Re > 1000 \end{cases} \tag{4.11}$$

To calculate Reynolds Number relative to phases in two-phase flow, the following is the co-relation:

$$Re = \frac{\rho_l|\vec{u_g} - \vec{u_l}|d_g}{\mu_l} \tag{4.12}$$

Also, for the gaseous phase the following is the co-relation:

$$Re = \frac{\rho_g|\vec{u_l} - \vec{u_g}|d_g}{\mu_{gl}} \tag{4.13}$$

Where $\mu_{gl} = \alpha_l\mu_l + \alpha_g\mu_g$ is the mixture viscosity of the phases g and l.

The secondary phase exerts a particular force over primary phase called as drag force. Hence, it represented as a vector directed along the relative velocity of the secondary phase. After an extensive amount of simulations with varying bubble diameter for gaseous phase, the pressure profile shows no change, at expansion or contraction section.

The term M_l^{VM} in momentum equation shows virtual mass force derived by cook [61], which shows acceleration of two-phases about each other. This virtual mass effect is significant when gaseous phase density is much smaller compared to liquid phase density. According to

findings of Anglart [62], Drew [57] if the bubbles and droplets are accelerating in the continuous phase, then the following equation holds validity:

$$M_l{}^{VM} = -M_g{}^{VM} = C_{VM} \times \alpha_g . \rho_l . \left(\frac{d_l \vec{u}_l}{dt} + \frac{d_g \vec{u}_g}{dt} \right) \tag{4.14}$$

Where, C_{VM} is Co-efficient of virtual mass which, according to Drew holds value of 0.5 and the term $\frac{d_l}{dt}$ represents liquid phase material time derivative of the form:

$$\frac{d_l(\phi)}{dt} = \frac{\partial(\phi)}{\partial t} + (\vec{u}_l . \nabla)\phi \tag{4.15}$$

Similarly, the gaseous phase, the phase material based time derivative is of the form:

$$\frac{d_g(\phi)}{dt} = \frac{\partial(\phi)}{\partial t} + (\vec{u}_g . \nabla)\phi \tag{4.16}$$

The virtual mass effect is significant when the secondary phase density is much smaller than the primary phase density (for example, for a transient bubble column the phase g, which reflects much smaller density value in comparison with phase l, the virtual mass effect is significant).

The lift force M_l^L term in momentum equation of multiphase model ascends from a velocity gradient of continuum of phases in lateral direction, which is according to Anglart [62], Drew [57], Drew [58], Lahey [25] represented as:

$$M_l{}^L = -M_g{}^L = C_l . \alpha_g . \rho_l . (\vec{u}_g - \vec{u}_l) \times (\nabla \times \vec{u}_l) \tag{4.17}$$

In above equation, C_l is a lift force coefficient. This coefficient for shear flow around droplet is valid with value 0.5.

4.4 Flow turbulence modeling

The modeling of multiphase flow turbulence requires two unique models that are turbulent kinetic energy (k) and turbulent dissipation rate (ϵ) in general case scenario. As solver represents two-phase flow mathematically as the combination of two different single-phase flows while modeling turbulence. Typically, this approach cannot accurately capture the underlying flow physics if the phasic interactions if the flow approaches its complexity. In such scenarios, it is better to combine multiphase algorithm along with turbulence modeling. Thus, in this case, the solver approach is to apply the full Reynolds-Stresses model of turbulence, in conjugation with the Eulerian-Eulerian multiphase model. In this study, the pressure drop application due to two-phase flow is more important than showing sharp phasic visualizations, hence dispersed model is implied in which Reynolds – Stresses are solved for continuous phase while the secondary phase is being dependent on continuous, which is a primary phase. For more robustness during analysis, the interaction between liquid, which considered as continuous, and dispersed phase, which is gaseous, and turbulence between them approximated. So that increment of normal stress participation during fluctuation of energy exchanged. Hence the following Reynolds Stresses Model is applied in this case Launder [53], Launder et al. [63], Spalding [52]:

Reynolds Stress Model (5 - equations):

$$\frac{\partial}{\partial t}(\alpha_l \rho_l (\overline{u_i u_i})_l) + \nabla.\left(\alpha_l \rho_l \vec{U_l} (\overline{u_i u_i})_l\right) \tag{4.18}$$

$$= -\left[\alpha_l \rho_l \left(\nabla.\left((\overline{u_i u_k})_l + \left(\overline{u_j u_k}\right)_l\right)\right)\right] + \nabla.\left[\alpha_l \mu_l \nabla.(\overline{u_i u_j})_l\right]$$

$$+ \alpha_l P'_{ij}[\nabla.(\overline{u_i u_j})_l] - \alpha_l \rho_l \epsilon_l$$

This model solves five equations, which are convection, Stresses production, Pressure Strain, turbulent dissipation, and turbulent kinetic energy. Hence, to achieve full closure solution

with absolute convergence, it is required to model linear pressure-strain term, turbulent kinetic energy, and turbulent dissipation using a standard K-Epsilon model analogy for dispersed phase approach. In addition, according to Tchen-theory [64], predictions for turbulence quantities for the dispersed phases are obtained by the turbulence of homogeneous mixture, which is dispersed, model. Hence according to Launder et al, Troshko & Hassan [53] [65], the equations are:

The transport equations for K:

$$\frac{\partial}{\partial t}(\alpha_l \rho_l k_l) + \nabla.\left(\alpha_l \rho_l k_l \vec{U_l}\right) \tag{4.19}$$

$$= \nabla.\left[\alpha_l \left(\mu_l + \frac{\mu_{t,l}}{\sigma_k}\right) \nabla k_l\right] + \left(\alpha_l G_{k,l} - \alpha_l \rho_l \epsilon_l\right)(1 + 2M_t^2)$$

$$+ K_{gl}\left(C_{gl} k_g - K_{lg} k_l\right)$$

$$+ [K_{gl}]\left[\frac{\rho_g}{\rho_g + 0.5 \times \rho_l}\right](k_{gl} - 2k_l + \vec{u_{gl,dr}})$$

The Transport equations for turbulent dissipation rate (ϵ):

$$\frac{\partial}{\partial t}(\alpha_l \rho_l \epsilon_l) + \nabla.(\alpha_l \rho_l \epsilon_l \vec{U_l}) \tag{4.20}$$

$$= \nabla.\left[\alpha_l \left(\mu_l + \frac{\mu_{t,l}}{\sigma_\epsilon}\right) \nabla \epsilon_l\right] + \alpha_l \rho_l C_{1,\epsilon} G_{k,l} - C_2 \alpha_l \rho_l \frac{\epsilon_l^2}{k_l}$$

$$+ C_{3,\epsilon} \frac{\epsilon_l}{k_l}\left[K_{gl}\left[\frac{\rho_g}{\rho_g + 0.5 \times \rho_l}\right](k_{gl} - 2k_l)\right]$$

$$+ K_{gl}\left[\left[\frac{\rho_g}{\rho_g + 0.5 \times \rho_l}\right]\left(\vec{u_{gl,dr}}\right)\right]$$

Thus, with the inclusion of the turbulence kinetic energy (k) (TKE), and Turbulence dissipation rate (ϵ) the entire Reynolds Stresses Model (RSM) takes an elaborative form, which shows a maximum number of variables and constants in the detailed analysis:

$$\frac{\partial}{\partial t}(\alpha\rho(u_i u_j))_l + \frac{\partial}{\partial x_k}(\alpha\rho\overline{U}_k(u_i u_j))_l \tag{4.21}$$

$$= -\alpha_l\rho_l\left[\overline{(u_i u_k)_l}\frac{\partial}{\partial x_k}(U_j) + \overline{(u_j u_k)_l}\frac{\partial}{\partial x_k}(U_i)\right]$$

$$+\left[\frac{\partial}{\partial x_k}[\alpha_l\mu_{gl}\frac{\partial}{\partial x_k}\overline{(u_i u_j)_l}\right]$$

$$-\frac{\partial}{\partial x_k}\left[(\alpha\rho\overline{(u_i u_j u_k)})_l + \alpha_l P'[\delta_{jk}u_i' + \delta_{ik}u_j']\right]$$

$$+\alpha_l P'\left(\overline{\frac{\partial u_i'}{\partial x_j} + \frac{\partial u_j'}{\partial x_k}}\right)_l - \alpha_l\rho_l\overline{\epsilon_{ij}}$$

$$-2\alpha_l\rho_l\Omega_k\left[\left[\overline{(u_j u_j)}_l + \overline{(u_j u_j)}_g\right] + \left[(\epsilon_{ik})_l + (\epsilon_{ik})_g\right]\right]$$

$$+\left[\left[\overline{(u_i u_i)}_l + \overline{(u_i u_i)}_g\right] + \left[(\epsilon_{jk})_l + (\epsilon_{jk})_g\right]\right]$$

$$+\sum_{n=l}^{n=g}\frac{K_{gl}}{\alpha_l\rho_l}\left(\frac{\rho_g}{(\rho_g + 0.5\times\rho_l)}\right)(k_{gl} - 2k_l)$$

$$+\sum_{n=l}^{n=g}\frac{K_{lg}}{\alpha_l\rho_l}\left(\frac{\rho_g}{(\rho_g + 0.5\times\rho_l)}\right)(\vec{v}_{gl}\cdot\vec{v}_{\mathrm{dr}})$$

This turbulence model holds values of 8 terms, which are described further in order to understand the entire model. The following table shows the values and their description.

Table 4-1: Explanation of each term with respect to their purpose in the equation.

Local Time Derivative =	$\boldsymbol{\frac{\partial}{\partial t}(\alpha\rho(u_i u_j))_l}$
Convection ($\boldsymbol{C_{ij}}$) =	$\frac{\partial}{\partial x_k}(\alpha\rho\overline{U}_k(u_i u_j))_l$

Turbulent Diffusion ($\boldsymbol{D_{T,ij}}$) =	$\frac{\partial}{\partial x_k}\left[(\alpha\rho\overline{(u_i u_j u_k)})_l + \alpha_l P'[\delta_{jk}u_i' + \delta_{ik}u_j']\right]$
Molecular Diffusion ($\boldsymbol{D_{L,ij}}$) =	$\left[\frac{\partial}{\partial x_k}[\alpha_l \mu_{gl}\frac{\partial}{\partial x_k}\overline{(u_i u_j)_l}\right]$
Stress Production ($\boldsymbol{P_{ij}}$) =	$\alpha_l\rho_l\left[\overline{(u_i u_k)_l}\frac{\partial}{\partial x_k}(U_j) + \overline{(u_j u_k)_l}\frac{\partial}{\partial x_k}(U_i)\right]$
Pressure Strain $(\boldsymbol{\varphi_{ij}})$ =	$\alpha_l P'\left(\overline{\frac{\partial u_i'}{\partial x_j} + \frac{\partial u_j'}{\partial x_k}}\right)_l$
Dissipation $(\boldsymbol{\epsilon_{ij}})$ =	$\alpha_l\rho_l\overline{\epsilon_{ij}}$
System Rotation $(\boldsymbol{F_{ij}})$ =	$2\alpha_l\rho_l\Omega_k\left[\left[\overline{(u_j u_j)}_l + \overline{(u_j u_j)}_g\right] + \left[(\epsilon_{ik})_l + (\epsilon_{ik})_g\right]\right]$ $+\left[\left[\overline{(u_i u_i)}_l + \overline{(u_i u_i)}_g\right] + \left[(\epsilon_{jk})_l + (\epsilon_{jk})_g\right]\right]$

Hence, using mathematical proposals of Gibson [54], the pressure-strain modeling is developed using following equation. This term is similar to the pressure-strain equation in the elaborated form of the RSM model.

$$\phi_{ij} = \phi_{ij,1} + \phi_{ij,2} + \phi_{ij,w} \tag{4.22}$$

In this $\phi_{ij,1}$ is the slow pressure-strain term, also known as return to isotropy term. $\phi_{ij,2}$ is called rapid pressure-strain term, and $\phi_{ij,w}$ is the wall reflection term.

Hence, the pressure-strain term $\phi_{ij,1}$ is modeled as:

$$\phi_{ij,1} = -1.8 \times \alpha_l\rho_l\frac{\epsilon_{ij}}{k}\left[(\overline{u_i u_i})_l - \frac{2}{3}\delta_{ij}k\right] \tag{4.23}$$

The term $\phi_{ij,2}$ holds the value for stress production term (P_{ij}), Force rotation term (F_{ij}), and convection term (C_{ij}) which is described above. Hence, it developed as:

$$\phi_{ij,2} = -0.6\left[\frac{P_{ij} + F_{ij} + 5}{C_{ij}} - \frac{1}{3}\delta_{ij}\left(\frac{\mathrm{P} + 10}{\mathrm{C}}\right)\right] \tag{4.24}$$

Moreover, the wall reflection term, $\phi_{ij,w}$ is responsible for re-distribution of normal stress near the wall. Which tends to provide accurate boundary layer information based on near wall parameters. This term left as default to its original state.

Therefore, a wall reflection effect for the mostly dispersed phase ($\phi_{ij,w}$) given as:

$$\phi_{ij,w} \equiv \begin{bmatrix} 0.5\frac{\epsilon_{ij}}{k}\left(\left(\overline{u_k'u_m'}\right)_l n_k n_m \delta_{ij} - \frac{3}{2}\left(\overline{u_i'u_k'}\right)_l n_j n_k - \frac{3}{2}\left(\overline{u_j'u_k'}\right)_l n_i n_k\right)\frac{C_\ell k^{\frac{3}{2}}}{\epsilon_{ij} d} \\ +0.3\left(\phi_{km} n_k n_m \delta_{ij} - \frac{3}{2}\phi_{ik} n_j n_k - \frac{3}{2}\phi_{jk} n_i n_k\right)\frac{C_\ell k^{\frac{3}{2}}}{\epsilon_{ij} d} \end{bmatrix} \tag{4.25}$$

The last term in (ϵ) equation is modeled according to Elgobashi [65]. In this closure for time mean equation is achieved by modeling the turbulence correction up to third order. Following equation shows the modeling of turbulence dissipation rate (ϵ_{ij}):

$$\Pi_{\epsilon_l} = 1.2\frac{\epsilon_l}{k_l}\Pi_{k_l} \tag{4.26}$$

The Π_{k_l} term in above equation is developed for turbulent interactions between phases of multiphase flow model.

Here, in above equations 4.19, and 4.20, $\vec{U_l}$ is phase-weighted velocity. It is represented in equation 4.21 as $\overline{U}_k$. In addition, the constant $C_1$is modeled as given:

$$C_1 = max\left[0.43, \frac{\eta}{\eta+5}\right], \qquad \eta = S \times \frac{k}{\epsilon}, \qquad S = (2S_{ij}S_{ij})^{0.5} \tag{4.27}$$

The terms C_{gl} , C_{lg} can be approximately calculated as,:

$$C_{gl} = 2, \qquad \& \qquad C_{lg} = 2\left(\frac{\eta_{gl}}{\eta_{gl}+1}\right) \tag{4.28}$$

The modeling of turbulent viscosity as per Troshko [66], $\mu_{t,l}$ is in terms of turbulent kinetic energy of liquid phase l :

$$\mu_{t,l} = \rho_l C_\mu \frac{k_l^2}{\epsilon_l} \tag{4.29}$$

Further, Lagrangian time scale $\tau_{t,gl}$ represented in the form of:

$$\tau_{t,gl} = \frac{\tau_{t,l}}{\sigma_1\sqrt{(1 + C_\beta \times \xi_\tau^2)}} \tag{4.30}$$

Where:

$$\xi_\tau = \frac{|\vec{U_g} - \vec{U_l}|}{\sqrt{(\frac{2}{3}k_l)}} \tag{4.31}$$

And,

$$C_\beta = 1.8 - 1.35\cos^2\theta \tag{4.32}$$

The characteristic time of the energetic turbulent eddies $\tau_{t,l}$ for continuous liquid phase defined as:

$$\tau_{t,l} = \frac{3}{2} C_\mu \frac{k_l}{\epsilon_l} \tag{4.33}$$

The ratio between these two-time scales is given as:

$$\eta_{gl} = \frac{\tau_{t,gl}}{\tau_{F,gl}} \tag{4.34}$$

For the dispersed phase model, the characteristic particle relaxation time connected with initial effects acting on the dispersed phase (here it is gaseous phase g) is represented as:

$$\tau_{F,gl} = \frac{\rho_l \times d_g^2}{18\mu_c f(Re, \alpha_l)} (1 + 0.5 \times \frac{\rho_l}{\rho_g}) \tag{4.35}$$

K_{gl} is stated as inter-phase turbulence momentum transfer exchange coefficient. According to the dependent phase in two-phase flows, the term modeled. For special cases such as particulate or bubbly gas-liquid flows, this term holds value as:

$$K_{gl} = -K_{lg} = \left(\frac{\rho_g f d_g A_i}{6\tau_g}\right) \tag{4.36}$$

In above co-relation, the variable τ_g is a drag function, which differs on case basis; in this case, we defined it as:

$$\tau_g = \frac{\rho_g d_g^2}{18\mu_l} \tag{4.37}$$

Where, d_g^2 is diameter of bubbles or droplets of gaseous phase g.

According to Reynolds analogy [67], the eddy viscosity model calculates averaged fluctuations of quantities. In that Reynolds stress tensor for liquid phase l, which is dispersed phase in large quantity, is defined as:

$$\overline{\overline{\tau_\mu}} = -\frac{2}{3}(\rho_l k_l + \rho_l \mu_{t,l} \nabla . \vec{U_l}) + \rho_l \mu_{t,l} (\nabla . \vec{U_l} + \vec{U_l}^T) \tag{4.38}$$

In K model the term production of turbulent kinetic energy, $G_{k,l}$ is computed as:

$$G_{k,l} = -G_{k,g} = (\mu_{t,l} \nabla . \vec{U_l}) + \rho_l \mu_{t,l} (\nabla . \vec{U_l} + \vec{U_l}^T) \tag{4.39}$$

Above equations show particular case of the eddy viscosity modeling.

During the calculations of turbulent eddies and viscosity terms, C_μ is calculated based on standard epsilon model which is kept constant as C_μ = 0.0845.

Along with that, according to Simonin [68, 69], turbulent quantities of the dispersed phase (gaseous phase g) as well as the turbulence interactions between both phases are written as:

$$k_{gl} = 2 \times k_l \left[\frac{(b + \eta_{gl})}{(1 + \eta_{gl})} \right] \tag{4.40}$$

$$k_g = 2 \times k_l \left[\frac{(b^2 + \eta_{gl})}{(1 + \eta_{gl})} \right] \tag{4.41}$$

$$D_{t,gl} = \frac{1}{3} k_{gl} \tau_{t,gl} \tag{4.42}$$

$$D_g = D_{t,gl} + \left(\frac{2}{3} k_g - b \frac{1}{3} k_{gl} \right) \tau_{F,gl} \tag{4.43}$$

Where the value for b is given as:

$$b = \frac{1.5}{\left[\frac{\rho_g + \rho_l}{\rho_l} \right]} \tag{4.44}$$

During interphase turbulent momentum transfer, the turbulent drag term for multiphase flow $K_{gl}(\vec{v_g} - \vec{v_l})$ is modeled as follows, for dispersed phase (gas) and continuous phase (liquid):

$$K_{gl}(\vec{v_p} - \vec{v_q}) = K_{gl}(\vec{U_g} - \vec{U_l}) - K_{gl} \vec{v}_{\mathrm{dr}} \tag{4.45}$$

Due to turbulent fluctuations in the continua as result of void fractions, the drift velocity is generated. This drift velocity also is shown in above equation as $\vec{v}_{\mathrm{dr}}$. This drift velocity is modeled as follows:

$$\vec{u}_{gl,dr} = -\left(\frac{D_g}{\sigma_{gl}\alpha_g}\nabla\alpha_g - \frac{D_l}{\sigma_{gl}\alpha_l}\nabla\alpha_l\right) \tag{4.46}$$

During the presence of the drift velocity, that is when multiplied by the exchange coefficient K_{gl} acts as a momentum correction factor in turbulent flows. Here $D_g \; and \; D_l$ are diffusivities and σ_{gl} is a dispersion Prandtl number. When using T-chen theory in multiphase flows [64], solver assumes $D_g = D_l = D_{t,gl}$ and the default value for σ_{gl} is 0.75.

4.5 Solver modeling and solution schemes

FLUENT solver, allows us to develop the mathematical model based on two types of solvers:

- Pressure based solver
- Density-based solver

In both methods, the velocity field is obtained from the momentum equations. The density-based approach shows, the continuity equation is obtained from density filed while the pressure filed is calculated from the equations of state. On the other hand, the pressure field is extracted by solving a pressure or pressure correction equation, which is obtained from manipulating the continuity and momentum equations, in pressure based solver approach.

In both the cases the governing integral Navier-Stokes equations (N-S-equations) for the conservation of laws and associated scalar equations such as turbulence or chemical species, are solved by using controlled-volume-based approach. This controlled-volume-based approach is defined further:

- Using computational grid, or mesh dividing domain into discretized control volumes
- Integrating dependent variables such as pressure, velocity temperature and conserved scalars, into governing equations on individual controlled volumes, and constructing algebraic sparse matrix equations for these variables.
- Linearization of discretized equations and solution of the resultant linear equations system to yield updated values of the dependent variables.

4.5.1 Pressure-based solver

A projection method, which is a general class of algebraic trial-error methods, is implemented by the pressure-based solver. In projection method, the constant of mass conservation of velocity field is achieved by solving a pressure equation. A derived pressure equation from continuity and momentum equations satisfies the pressure corrected velocity field of continuity equation. Since the governing equations are non-linear sparse matrices, which are coupled with one another, the solution process involves iterations that are designed to set off the governing

equations in repetitions until the solution is converged. The following flowchart shows the pressure based coupled algorithm:

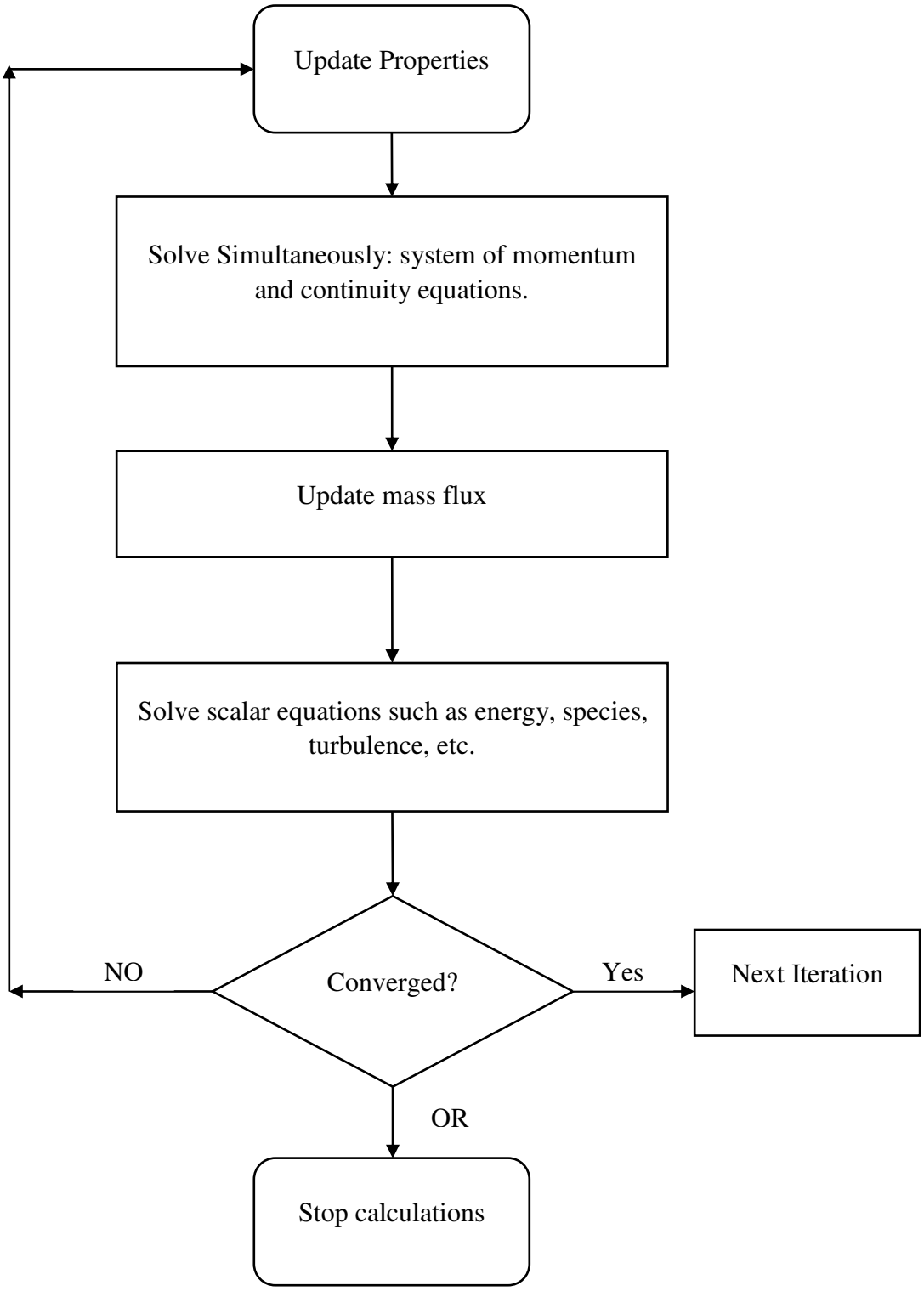

4.5.2 Equations discretization using QUICK scheme.

The control volume technique consists of integrating the transport equation about each control volume, yielding a discrete equation that expresses the conservation law on the control-volume basis. In general, the discretization of governing equations can be explained by considering the partial differential equation term of quantity ϕ. The applied arbitrary control volume V shows the equation in following format:

$$\int_V \frac{\partial \rho \phi}{\partial t} dV + \oint \rho \phi \vec{v} \cdot d\vec{A} = \oint \Gamma_\phi \nabla \phi \cdot d\vec{A} + \int_V S_\phi \, dV \tag{4.47}$$

Where:

ρ = Density

$\vec{v}$ = Velocity vector($u\hat{\imath} + v\hat{\jmath};\ For\ 2D\ cases$)

$\vec{A}$ = Surface area vector

Γ_ϕ = Diffusion co-efficient for ϕ

$\nabla\phi$ = Gradient of ($\phi = \frac{\partial \phi}{\partial x}\hat{\imath} + \frac{\partial \phi}{\partial y}\hat{\jmath}$ for 2D cases)

S_ϕ = Source of ϕ per unit volume

Above equation is applied to all computational domain, volume, cell. In this research, applied computational geometry is meshed based on 'all quad' cells, with the orthogonal quality of 0.98. That is more than 91% of cells have four faces. For any control volume poly-hydra based multidimensional case solver solves with the below given equation. Considering this fact, the below is the quad cell-based derived equation of control-volume technique:

$$\frac{\partial \rho \phi}{\partial t} V + \sum_{f}^{N_{\text{faces}}} \rho_f \vec{v}_f \phi_f \cdot \vec{A}_f = \sum_{f}^{N_{\text{faces}}} \Gamma_\phi \nabla \phi_f \cdot \vec{A}_f + S_\phi V \tag{4.48}$$

Where:

N_{faces}	=	Number of faces enclosing single cell
ϕ_f	=	Value of ϕ converted through face f
$\rho_f \vec{v}_f \phi_f$	=	algebraic value of Mass flux through particular face
$\vec{A}_f$	=	Area of face f, $\lvert A \rvert = \lvert A_x \hat{\imath} + A_y \hat{J} \rvert$
$\nabla \phi_f$	=	Gradient of (ϕ) for particular face f
V	=	Control volume

However, as the equations are increased, and the case becomes a scenario of complex fluid flow the solver implements time and computing resources efficient spatial discretization scheme. For quadrilateral and hexagonal poly-hydra, this scheme is applied in this research to generate less time consuming and more accurate results. Quadratic Upstream Interpolation for Convective Kinematics (QUICK), Leonard [70], is a higher order control volume interpolations derived scheme, where unique upstream and downstream cells are identified by interpolating previously generated values at the center cell. For specified 1D control volume, the faces are defined as $f_1, f_2, and\ f_3$. The applied figure shows the 1D control volume.

The traditional QUICK scheme is obtained by setting $\theta = \frac{1}{8}$. The implementation in computational code uses a variable θ and its solution-dependent value, which is chosen to avoid introducing solution extrema. The QUICK scheme is more solution accurate due to structured grids, constructed according to flow direction.

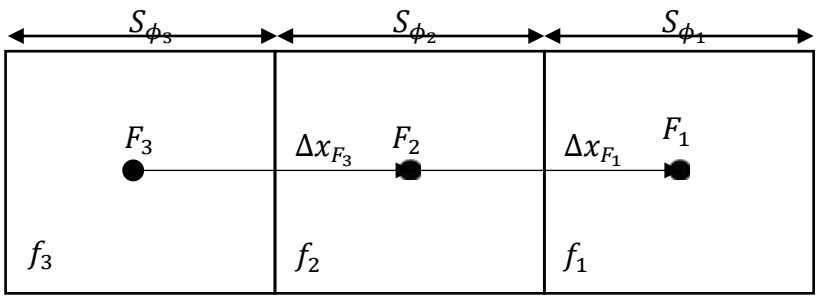

Figure 4.1. Grid (elements) structure in quad based 2D mesh

Hence, the equation for the above 1D control volume becomes:

$$\phi_{f_1} = \theta\left[\frac{S_{\phi_1}}{S_{\phi_2}+S_{\phi_1}}\phi_{F_2} + \frac{S_{\phi_2}}{S_{\phi_2}+S_{\phi_1}}\phi_{F_1}\right] + (1-\theta)\left[\frac{S_{\phi_3}+2S_{\phi_2}}{S_{\phi_3}+S_{\phi_2}}\phi_{F_2} - \frac{S_{\phi_2}}{S_{\phi_3}+S_{\phi_2}}\phi_{F_3}\right] \tag{4.49}$$

As the QUICK is termed as higher order scheme, the generated terms during analysis create a higher amount of residuals. This requires significant memory locations and substantial processing time. Thus, solver can reduce these higher order residual values by multiplication of higher order terms relaxations factor. This is helpful during transient and pseudo-transient analysis with large time-stepping values.

4.5.3 Implicit time integration for transient and pseudo-Transient simulations

The governing non-linear sparse matrix equations must be discretized over time and space for transient and pseudo-transient simulations. In steady state flow case, the spatial discretization and time-stepping algorithms are identical as the time-based derivative is canceled. However, regarding time-based (temporal) discretization, every term in partial differential equations is collectively iterated over time step Δt. The integration of time step derivative is given below:

$$\frac{\partial \phi}{\partial t} = F(\phi) \tag{4.50}$$

Where the function $F(\phi)$ incorporates any spatial discretization. Generically, the first-order accurate temporal discretization is given, If the time derivative is discretized using backward differences, which is given by:

$$\frac{\phi^{n+1} - \phi^n}{\Delta t} = F(\phi) \tag{4.51}$$

Nevertheless, during the implicit scheme of time integration $F(\phi)$ is evaluated using future time step forecasting technique based on the previous value. This helps flow convergence collectively over spatial discretization schemes. Hence, the time step derivative becomes:

$$\frac{\phi^{n+1} - \phi^n}{\Delta t} = F(\phi^{n+1}) \tag{4.52}$$

The above equation is referred as "implicit" integration since ϕ^{n+1} in a given cell is related to ϕ^{n+1} in neighboring cells through $F(\phi^{n+1})$:

$$\phi^{n+1} = \phi^n + \Delta t \times F(\phi^{n+1}) \tag{4.53}$$

4.5.4 Discretization implementation

The above discretization scheme is implemented by solver during the analysis. Integral N-S equations should be able to solve to find the physics-based answers using mathematics by using the optimum time, and computational resources are the primary goals of using the solver. Thus, discretization schemes are used to transform these PDE's into sparse matrices to compute the answers. In this section, we will describe these schemes as implementations over momentum, continuity, pressure-velocity coupling, and other scalar equations such as turbulence.

4.5.4.1 Momentum discretization

Similar to other scalar transport equations such as turbulence and species, the integral physics based momentum transport equation is also discretized. For example, in case of 1D x-momentum equation in primary fluid flow can be discretized and obtained by setting $\boldsymbol{\phi} = \boldsymbol{u}_{\mathbf{ij}}$**.:**

$$\frac{\partial \rho \boldsymbol{u}_{\mathbf{ij}}}{\partial t} V + \sum_{f_1}^{N_{\text{faces}}} \rho_{f_1} \vec{v}_{f_1} \boldsymbol{u}_{\mathbf{ij}_{f_1}} \cdot \vec{A}_{f_1} = \sum_{f_1}^{N_{\text{faces}}} \Gamma_{\phi} \nabla(\boldsymbol{u}_{\mathbf{ij}_{f_1}}) \cdot \vec{A}_{f_1} + S_{\phi_1} V \tag{4.54}$$

Where:

N_{faces}	=	Number of faces enclosing single cell
$\boldsymbol{u}_{\mathbf{ij}_{f_1}}$	=	Momentum converted through face f
$\rho_f \vec{v}_f \boldsymbol{u}_{\mathbf{ij}_{f_1}}$	=	algebraic value of Mass flux generated by momentum through particular face
$\vec{A}_{f_1}$	=	Area of face f, $\lvert A \rvert = \lvert A_x \hat{\imath} + A_y \hat{J} \rvert$
$\nabla \boldsymbol{u}_{\mathbf{ij}_{f_1}}$	=	Gradient momentum for particular face f
V	=	Control volume

If the pressure field and the face mass fluxes are known through boundary conditions, during setting up simulations, then the equation can be solved by above given NITA scheme or any other suitable scheme, and velocity field is obtained. Without essential boundary conditions, these equations lead to divergences although the physics of modeling are correct. After initialization of flow field, these values are specified at the cell centers. In above equation the suffix f_1 is taken from the reference of above Figure 4.1. Pressure Interpolations and discretization

In this research, the second order equations constructed pressure discretization scheme is utilized. The second order scheme reconstructs the face pressure using a cell center derived differentiation scheme. Thus, the pressure values at flow continua initialization at the faces and cell centers is presented by equation:

$$P_f = \frac{1}{2}\left[(P_{F_1} + P_{F_2}) + (\nabla P_{F_1} \cdot \vec{r_{F_1}} + \nabla P_{F_2} \cdot \vec{r_{F_2}})\right] \tag{4.55}$$

In above equation, the reference of suffixes such as F_1, F_2 are taken from Figure 4.1.

4.5.4.2 Continuity discretization

The continuity equation can be modeled same as momentum equation, in fact, while modeling the momentum equation; the continuity equation is derived based on the pressure correction equation. Hence using higher order quadratic upwind interpolation for convective kinematics the momentum equation shows discretization of continuity equations as follows:

$$\sum_{f_1}^{N_{\text{faces}}} J_{f_1} A_{f_1} = 0 \tag{4.56}$$

To find the solution of the above discretization, it is necessary to relate the values of the velocity to store the variable named velocity in cell conditions, while initialization. Linear interpolation of the face values results in unphysical initialization of pressure-correction equation. This Rhie-Chow algorithm [71] is implemented to avoid pressure divergence at the beginning. Hence, the continuity equation is weighted averaged just like momentum equation using factor of weighted averaging as a_P using the procedure the continuity mass flux is written as:

$$J_{f_1} = \rho_{f_1} \frac{a_{p,c_0} v_{n,c_0} + a_{p,c_1} v_{n,c_1}}{a_{p,c_0} + a_{p,c_1}} + d_{f_1}((p_{c_0} + (\nabla p)_{c_0} \cdot \vec{r_0}) - (p_{c_1} + (\nabla p)_{c_1} \cdot \vec{r_1})) = \hat{J}_{f_1} + d_{f_1}(p_{c_0} - p_{c_1}) \quad (4.57)$$

Where p_{c_0}, p_{c_1}, $and\ v_{n,c_0}, v_{n,c_1}$ are pressure and velocities respectively for specific cell within two cells or the sides of face and the term J_{f_1} contains the influence of the velocities in these cells. The term d_f is the function of $\overline{a}_P$, for integral momentum equation.

4.5.5 Pressure-Velocity Coupled scheme

The problem solved using pressure-based solver either is in a segregated manner or coupled manner, which is Phase Coupled Semi-Implicit Method for Pressure-Linked Equations (PC-SIMPLE) [72]. For this research, we are solving the problem using full-coupled approach for single-phase as well as two-phase flows. Form the equation (57) the pressure correction discretization as well pressure-velocity coupling archived by reformatting continuity equation. The advantage over segregated solver is obtaining a solution in the robust and efficient way for single-phase as well as the two-phase implementation of steady-flow, with superior performance and accurate results. Due to massive time-stepping is involved; also taking precautions for poor triangulations or sudden generations of poly-hydras in the computational grid, this scheme is used.

The pressure based segregated algorithm solves the momentum equation and pressure-correction equation separately, resulting in slow convergence. While coupled algorithm scheme combines both equations and provides a solution as singular implicit discretization. To achieve full-coupled scheme, velocity, and other scalar quantities are combined, including Rhie-Chow pressure dissipation terms.

For component k in the fluid continua, the pressure gradient of momentum equation becomes:

$$\sum_{f_1}^{n} p_{f_1} A_k = -\sum_{j}^{n} a^{u_k p} p_j \tag{4.58}$$

Where, $a^{u_k p}$ is a co-efficient derived from the Gauss divergence theorem which states that volume integral of the divergence over the region inside the surface is equal to the vector field through that closed surface, and pressure interpolation schemes. Hence, considering i^{th} cell, with j^{th} cell in y direction, the discretized form of the momentum equation for component u_k is defined as:

$$\sum_{j}^{n} {a_{ij}}^{u_k u_k} \; u_{kj} + \sum_{j}^{n} {a_{ij}}^{u_k p} \; p_j = {b_i}^{u_k} \tag{4.59}$$

In addition, the continuity equations also appear in the discretized form:

$$\sum_{k}^{n}\sum_{j}^{n} {a_{ij}}^{p u_k} \; u_{kj} + \sum_{j}^{n} {a_{ij}}^{pp} \; p_j = {b_i}^{p} \tag{4.60}$$

As overall results of quantitative system analysis, the systems of equations are transformed in the form of δ −unity form, and presented in form of matrix such as:

$$\sum_{j}^{n} [A]_{ij} \vec{X_j} = \vec{B_i} \tag{4.61}$$

Over the influence of cell i and cell j for all equations:

$$A_{ij} = \begin{bmatrix} a_{ij}^{pp} & a_{ij}^{pu} & a_{ij}^{pv} & a_{ij}^{pw} \\ a_{ij}^{up} & a_{ij}^{uu} & a_{ij}^{uv} & a_{ij}^{uw} \\ a_{ij}^{vp} & a_{ij}^{vu} & a_{ij}^{vv} & a_{ij}^{vw} \\ a_{ij}^{wp} & a_{ij}^{wu} & a_{ij}^{wv} & a_{ij}^{ww} \end{bmatrix} \tag{4.62}$$

Also, the unknown residual vector forms have matrix equations as:

$$\vec{X}_j = \begin{bmatrix} p_i' \\ u_i' \\ v_i' \\ w_i' \end{bmatrix} \tag{4.63}$$

And,

$$\vec{B}_i = \begin{bmatrix} -r_i^p \\ -r_i^u \\ -r_i^v \\ -r_i^w \end{bmatrix} \tag{4.64}$$

4.5.6 Coupled solution for multiphase flows

FLUENT solver solves the phase momentum equations, for Eulerian multiphase calculations. The shared pressure is solved in two ways one is coupled algorithm, and another one is a separated algorithm. The user defines the solution method based on the mathematical modeling he /she has done. While solving the equations in a segregated manner in particular with multiphase flow model, solver uses the Phase-Coupled-SIMPLE (PC-SIMPLE), Patankar [72], algorithm. This solution algorithm is based on single-phase Semi-Implicit Method for Pressure–Linkage Equations, well suited to solve the discretized macroscopic balance equations of mass, momentum, and energy for mixture or homogenous flow. This pressure correction technique is an iterative approach to cater for implicit type algorithms for steady and transient flows using per phase pressure–velocity equations. Nevertheless, due to compressibility effects in pressure and velocity of the gaseous phase. This equation fails to acknowledge the truncation error, further failing convergence of the equations. Also, this approach increased the equation solution divergence while solving the pressure correction equations along with pressure-velocity per phase coupling, during implicit analysis that results into divergence.

Another disadvantage of using Phase-Coupled-SIMPLE is asymmetry of the resultant matrix for continuity constraints, which probably generate zeroed diagonal box and convert entire matrix in echelon form or diagonal identity matrix, making the solution challenging to obtain. The problem can quickly solve by using direct sparse matrix solvers, which are third party and proprietary, resulting inexpensiveness for large and complex cases. Also, in the multiphase model due to the presence of two interchanging phases the case of vanishing phase from the particular cell can result in asymmetric matrices. With these prominent reasons, for multiphase cases, it is a wise decision to use full-volume fraction inclusive phase coupled solver.

For multiphase with 2-phases, the vector solution shows x$(p', u_1', v_1', w_1', u_2', v_2', w_2', \alpha_2')$ with the shorter notations, $(p', U_1', U_2', \alpha_2')$. Hence, for following matrix:

$$\sum_{j}^{n} [A]_{ij} \vec{X_j} = \vec{B_i} \tag{4.65}$$

Becomes:

$$\begin{bmatrix} a_{ij}^{pp} & \left(a_{ij}^{pu}\right)^{g} & \left(a_{ij}^{pv}\right)^{l} & \left(a_{ij}^{pw}\right)^{\alpha_2} \\ (a_{ij}^{up})^{g} & \left(a_{ij}^{uu}\right)^{g} & \left(a_{ij}^{uv}\right)^{lg} & \left(a_{ij}^{uw}\right)^{g} \\ \left(a_{ij}^{vp}\right)^{l} & \left(a_{ij}^{vu}\right)^{gl} & \left(a_{ij}^{vv}\right)^{l} & \left(a_{ij}^{vw}\right)^{l} \\ a_{ij}^{wp} & \left(a_{ij}^{wu}\right)^{g} & \left(a_{ij}^{wv}\right)^{l} & \left(a_{ij}^{ww}\right)^{\alpha_2} \end{bmatrix} \begin{bmatrix} p_i' \\ (u_i')^{l} \\ (v_i')^{g} \\ (w_i')^{\alpha_2} \end{bmatrix} = \begin{bmatrix} -r_i^{p} \\ -r_i^{u} \\ -r_i^{v} \\ -r_i^{w} \end{bmatrix} \tag{4.66}$$

This system can easily be generated until the presence of n phases. The components of above matrix are also matrices.

For large value problems, such as the one involved in this research, the Algebraic Multi-Grid (AMG) solver with Incomplete Lower Upper (ILU) smoother provides an accurate and robust method. Along with it, fully coupled solver with pseudo-transient time stepping method adds more diagonal to the matrix.

CHAPTER V

COMPUTATIONAL PROCEDURE

5.1 General Pre-processing

Before starting of any simulation general pre-processing is essential. During this pre-processing, a researcher decides the geometrical design based on the mathematical modeling requirement. In addition, to reduce the simulation time and computational load it is essential to find the required part of experimental setup need to be mathematically modeled. A significant amount of Computer Aided Design software are available. This computer-aided software developed based on the concept of parametric coordinate system and point perturbation algorithm. The mathematical model developed using 2-Dimensional co-ordinate system hence using computer-aided design software Two-dimensional geometry constructed. Two-dimensional axis-symmetrical parameters chosen for simplicity and efficiency during computing while less expensive computational cost. The experimental test section is a cylindrical pipe with specific diameters, hence to define the geometry in with all geometrical constraints; it is easy to develop a rectangular profile as a cross-section of a cylindrical pipe. In addition, as the goal of this study, it is essential to plot the graphs over the axis of geometry to know the axial pressure profile values hence using the axis-symmetric case settings and developing the geometry according to these settings, the work of computational setup reduces.

For solving sparse matrix based algebraic equations the controlled area or controlled volume need to divide into a multiple numbers of elements. In simple terms, the process of division

of arbitrary controlled volume or area into a number of elements for accurately calculate flow field equations is called as meshing. Thus the governing flow equations are transformed from $f(x, y)\ to\ g(\xi, \eta)$ as new independent variables.

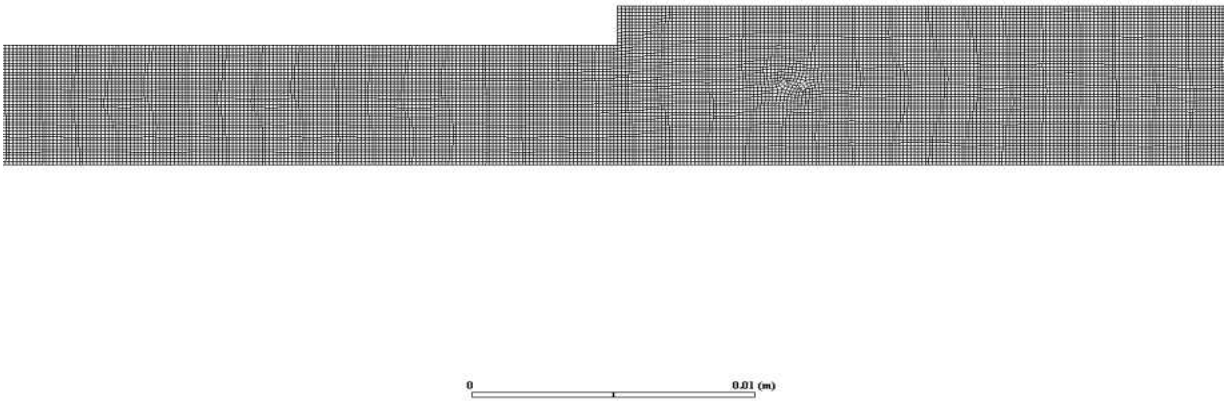

Mesh for test section 0.375-0.5, $\sigma = 0.5625$

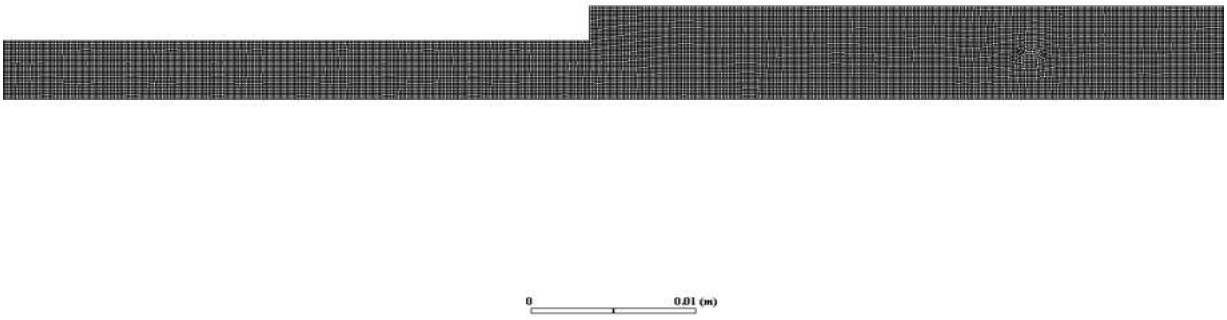

Mesh for test section 0.315-0.5, $\sigma = 0.3844$

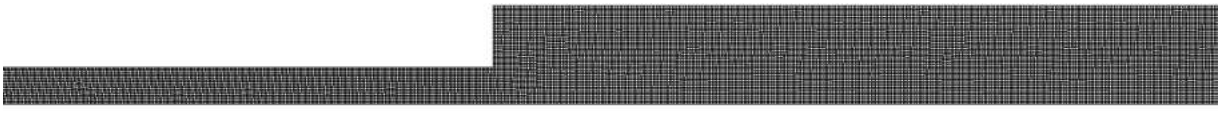

Mesh for test section 0.19-0.5, $\sigma = 0.1444$

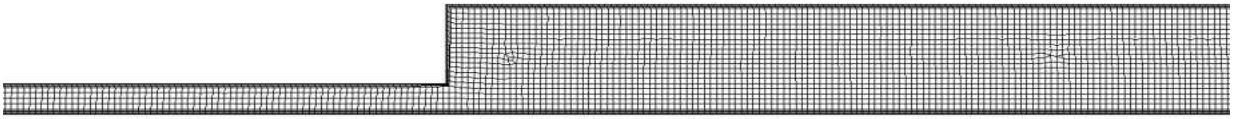

Mesh for test section 0.14-0.5, $\sigma = 0.0784$

Figure 5.1. The meshes of test sections which were used in experimental analysis shown by zooming

After the development of CAD geometry, using import option of meshing software fetches the geometry in the meshing environment. Since the geometry is a surface regarding CAD terminology, it is represented as 2D controlled surface shape with mathematically negligible thickness. The edges are representative ‘Named Selection,' for example, if one knows the presence

of axis in the geometry, then using the 'Named selection' option one can label the line as an axis, which further considered as an axis for boundary conditions in solver simulations environment. Therefore, using leading mesh generation algorithm called 'quadrilateral dominant cut-cell node method', meshes generated with an average orthogonal quality of 0.98 in meshing elements. This helps to define superior and accurate meshing with all quads meshing parameter, and 95-97% relevance for computational fluid flow based meshing. In concern with elements in corners of geometry especially around the area of sudden change, the proximity parameter considered for certain mesh generation at those zones of the domain. Further, named selections given as inlet, outlet, and walls to respective geometry parts. The mesh stored in solver oriented meshing format. Moreover, imported in the solver for further numerical analysis.

5.2 Simulation environment selection

The selection of simulation environment regarding mathematical modeling is another crucial step for any simulation engineer. Although the parameters in simulation environment software show universal values, every case treated as a different set of mathematical equations.

In this section, standard parameters discussed which are required to set up regardless of single-phase flow or two-phase flow mathematical modeling. After importing in solver, axis-symmetric parameter, and absolute velocity formation option selected, while pressure based solver selected for more accuracy (The solver/computing scheme is discussed in computational modeling in more details).

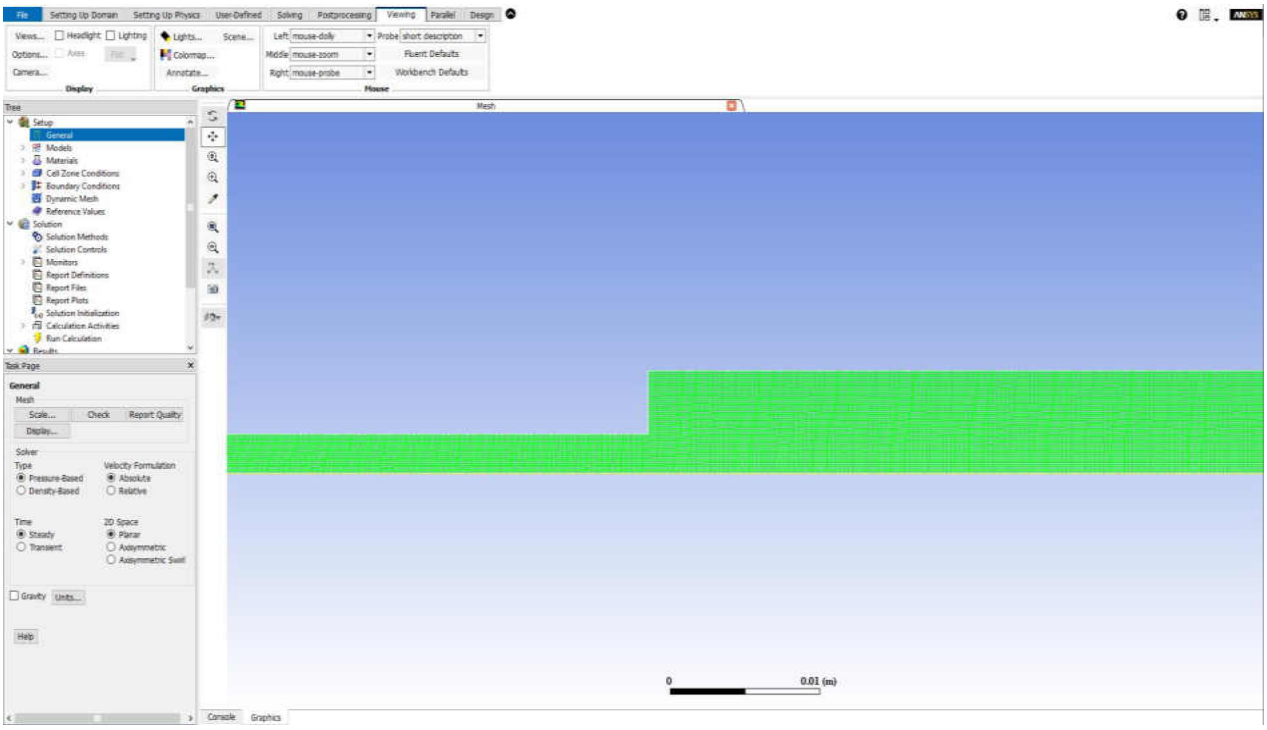

Figure 5.2. Overall solver environment window

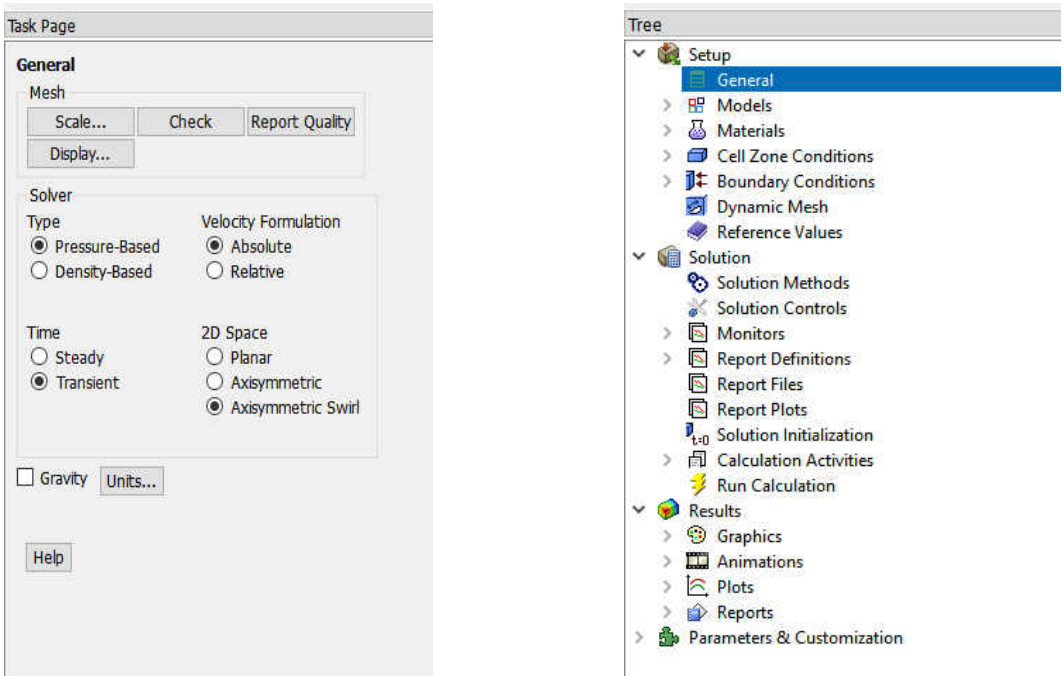

Figure 5.3. The first one shows basic task page of solver Second one shows task tree where all tasks are contained

However, apart from this, mesh quality analyzed for accuracy. The imported mesh considered as generic mesh generation algorithm by solver because solver can import different types of meshes from various sources. As a result of that, due to node-drop or cell misconfiguring, develops undesired ‘poly-hydras’ (for example, tetrahedral cells in the place of quad cell meshing algorithm) which further generate misrepresentation of computational results. As an unstructured solver based simulation environment, the analysis uses solver dependent data structures for its cell faces node points and overall elements. Therefore it is possible to develop best boundary condition accustomed mesh topology which is the unstructured approach, compared to old meshing (i,j,k array based) algorithms were converted to quad cells to increase more precision.

5.3 Single Phase flow setup

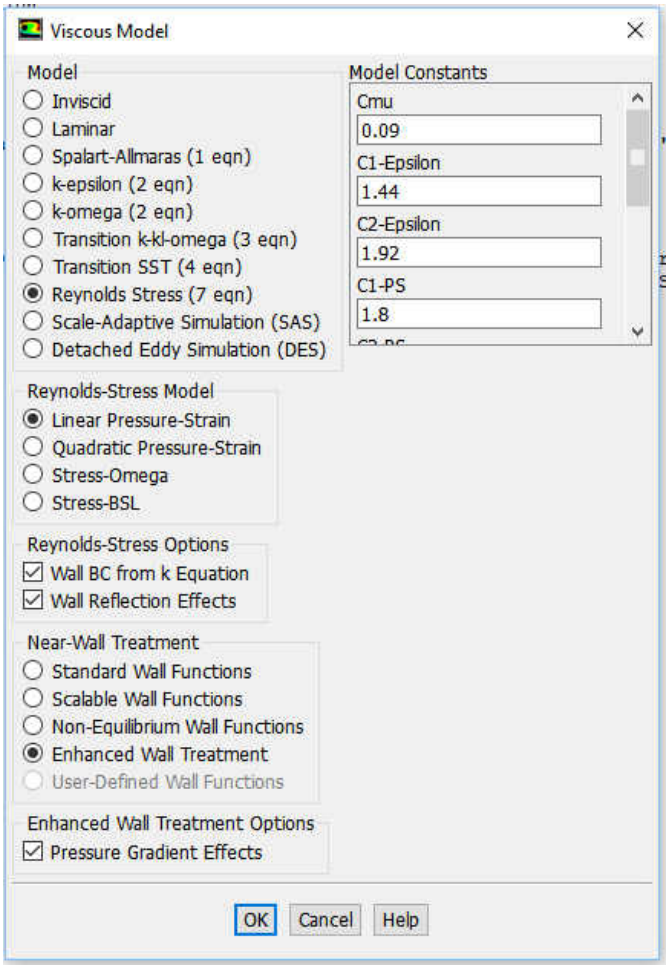

Figure 5.4. Model selection for single-phase flow where Reynolds Stress Model (5-equation) is shown

5.3.1 Solver model selection

After preparing the mesh suitable for transient solver time-based simulation parameter selected with the pressure-based solver. Units are for length is changed from mm to inches as the geometry was designed using 'inches' measurement unit. This helps during defining boundary conditions. Under parameter tree, 'Models' option is chosen (Figure 5.4). A Reynold's Stress (5-equation) with linear pressure-strain parameter selected. Along with it, Wall Boundary Conditions (BC) from kinetic energy equation and wall reflection effects chosen. Enhanced near wall

treatment is considered to study boundary layer phenomenon. Also, this relation between enhanced wall effect and pressure generation is activated, which is called as pressure gradient effects. The model constants further discussed in the table.

Table 5-1: Reynold's Stress equation model constants

Reynold's Stress equation model constants	
$\mathbf{C_\mu}$**(model constant wall friction)**	0.09
$\mathbf{C_1 - \epsilon}$ **(Constant one, dissipation rate)**	1.44
$\mathbf{C_2 - \epsilon}$**(Constant two, dissipation rate)**	1.92
$\mathbf{C_1 - PS}$ **(Constant one, Pressure_Strain rate)**	1.8
$\mathbf{C_2 - PS}$ **(Constant two, Pressure_Strain rate)**	0.6
$\mathbf{C'_1}$**_PS (Derived Constant one, Pressure_Strain rate)**	0.5
$\mathbf{C'_2}$**_PS (Derived Constant two, Pressure_Strain rate)**	0.3
Turbulent Kinetic Energy Prandtl number constant	1
Turbulent Dissipation Rate Prandtl number constant	1.3

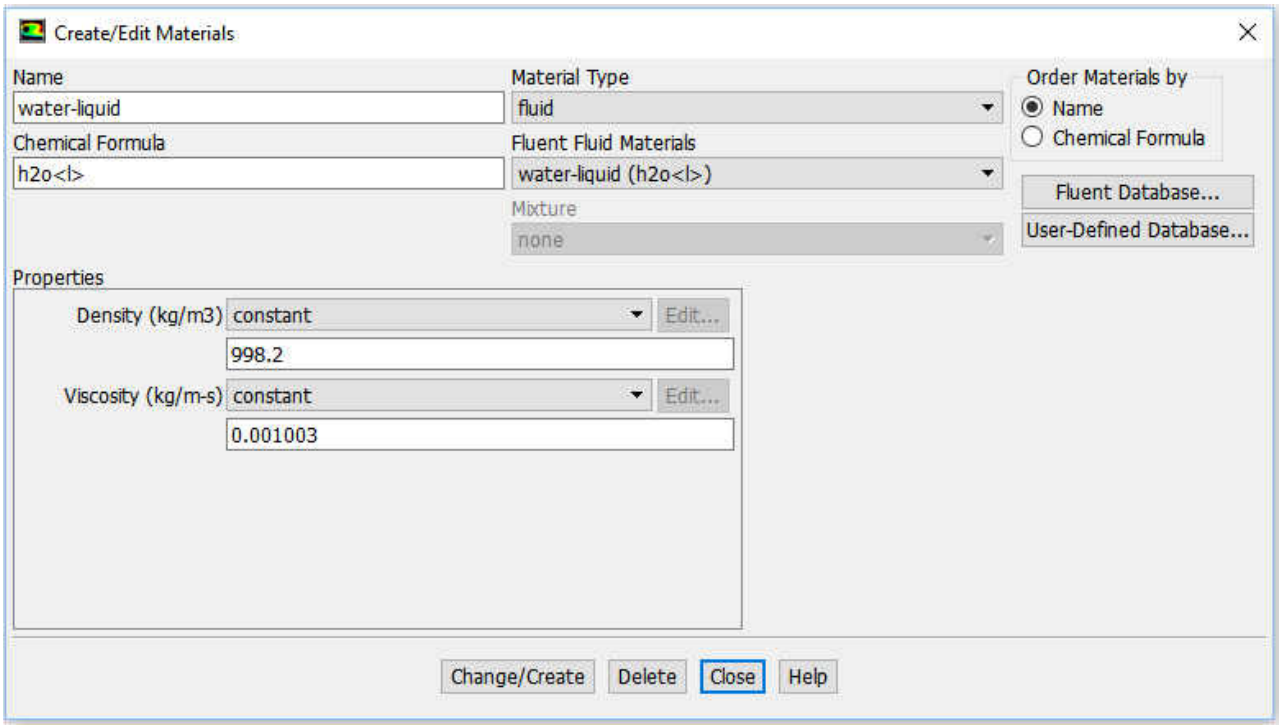

Figure 5.5. Material selection task page water with constant properties chosen as material

5.3.2 Material selection

After setting up the model, the material is chosen to be water under the material tab of simulation setup tree (Figure 5.5). First, the test sections were decided to set up the flow field with single-phase flow with only water as a continuum. Hence, the only one material and that is water chosen for simulation. Although heat transfer is not a part of the study, single-phase liquid based simulation aid to understand and anticipate the flow boundary conditions, geometrical parameters, the pressure exerted on test section and the thermodynamics and heat transfer of flow. Therefore with the help of previous literature, it was decided to set up the continuum mechanics of fluid as water.

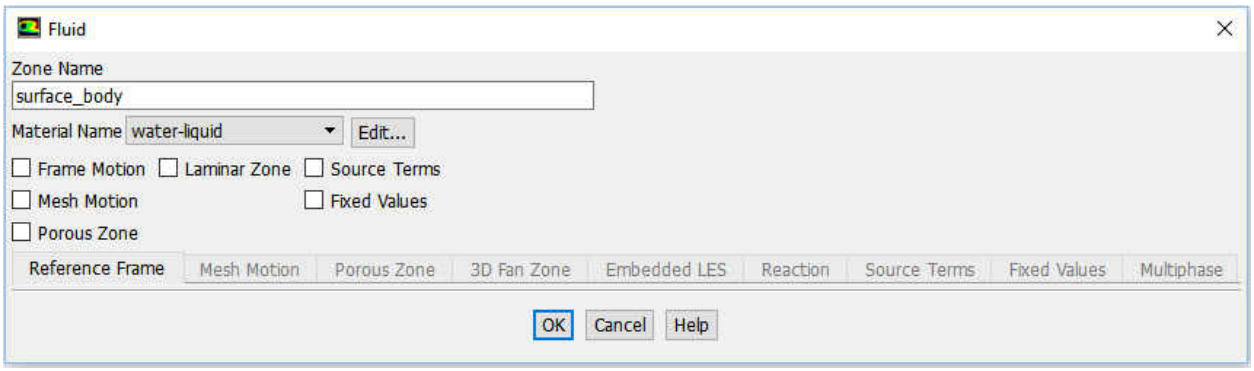

Figure 5.6. Cell-zone conditions selected as general and solver recognizes the body 2D surface body

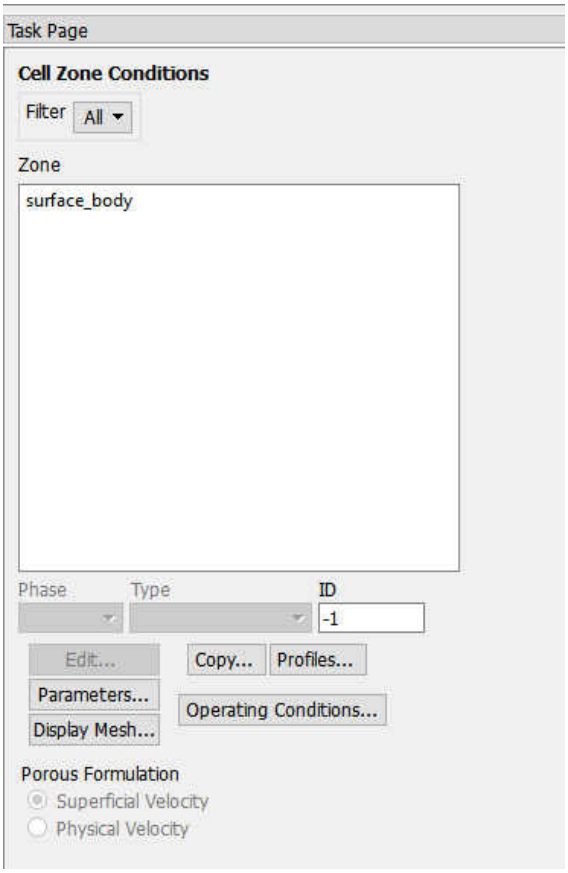

Figure 5.7. Cell-zone conditions task page where under operating conditions tab pressure is defined.

5.3.3 Cell-Zone and boundary conditions

'Cell Zone Conditions' and 'Boundary Conditions' is the most critical part of computational fluid dynamics. For this reason, five cases were developed for the single experimental dataset. The filled part inside 2D or 3D boundary of the body appears as a continuum for simulation environment in 'cell zone condition' task page of solver (Figure 5.6). This continuum can be derived from the mesh developed over entire test section. If the developed mesh is dynamic, hexagonal cut cell method then zone derived from the mesh is called as moving zone. Here, in this case, the part named as 'surface_body,' and due to simple 'all quad grid algorithm,' the mesh reflected as non-moving, static frame. The type for this cell zone is fluid, and the material chosen for the mesh is water-liquid(H_2O). The atmospheric pressure selected as 101325 Pa under 'Operating Conditions' tab of same task page (Figure 5.7).

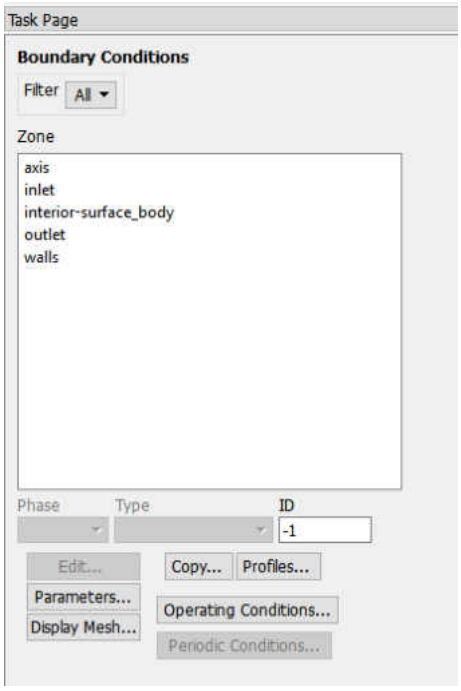

Figure 5.8. Boundary Conditions (BC) task page where conditions to solve the sparse matrix equations are given.

Boundary condition task page shows the initial and boundary conditions required solving the momentum, continuity, and energy equations to find the residuals and physics-based answers. In addition, 'Boundary Conditions' section allows defining reliable turbulence properties. If the boundary lines and surfaces are marked with names during mesh generation, solver displays it as 'Boundary Condition' zones. Hence, for example, in this case, the zones are derived as 'Axis,' 'Inlet,' 'Interior-surface_body,' 'Outlet,' 'Wall.' Although the zones displayed in this task page, the researcher need to define their respective type in the simulation. The following table shows the boundary condition choice:

Table 5-2: Boundary conditions used for the simulation

Boundary Condition(s) Type (Thermally Equilibrium)	**Single-phase flow Contraction and Expansion**	**Two-phase flow Expansion**	**Two phase flow Contraction**
Inlet	Mass flow rate (kg/s),	Mass flow rate (kg/s), Pressure @ Inlet.	Mass flow rate (kg/s), Pressure @ Inlet.
Outlet	first: Outflow, After steady state, Pressure @ Outlet	Pressure @ Outlet	Pressure @ Outlet
Wall	No-Slip,	No-Slip,	No-Slip,
Volume fraction	N/A	values were taken after calculating Ghajar's co-relation	values were taken after calculating Ghajar's co-relation

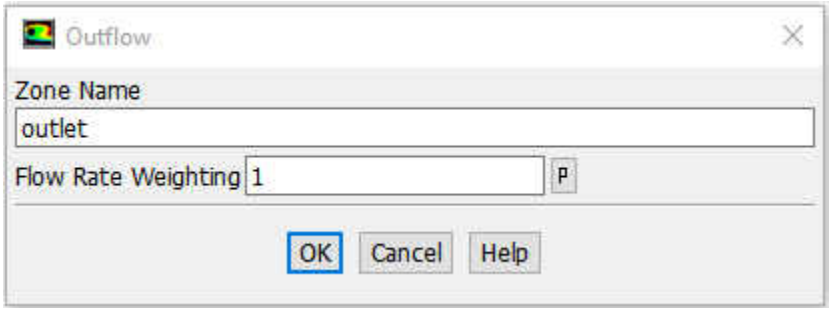

Figure 5.9. Outlet boundary condition is defined as outflow at start to stabilize the flow

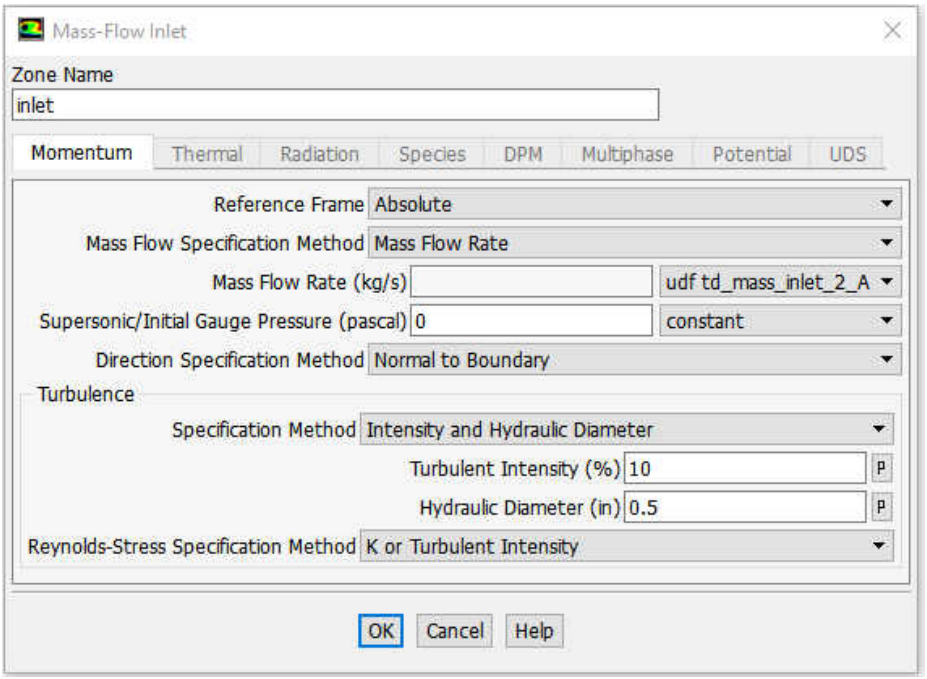

Figure 5.10. Inlet boundary condition, mass flow rate is defined as user-defined function (UDF) and turbulent intensity defined as high

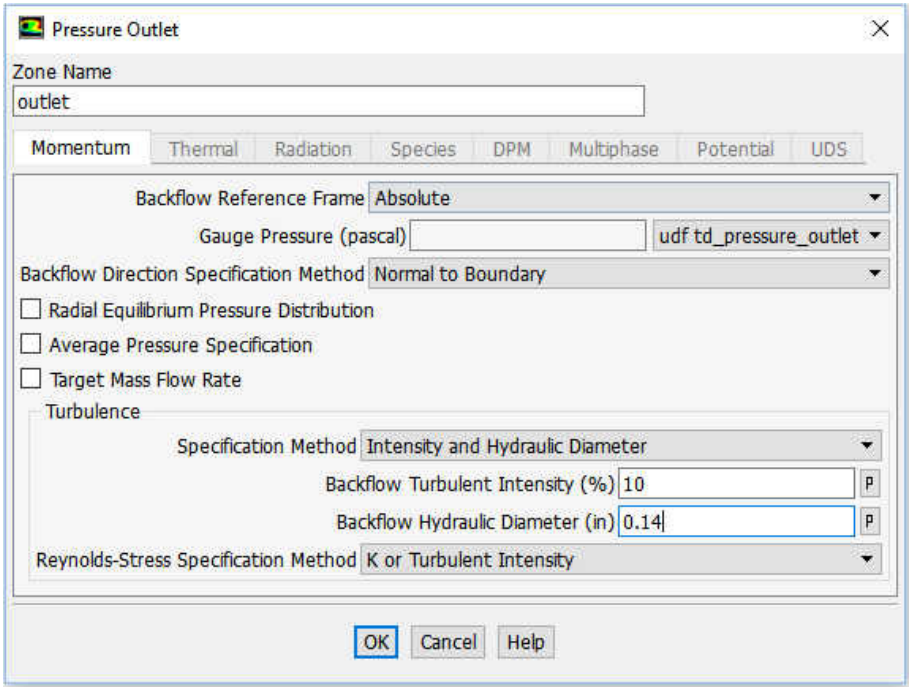

Figure 5.11. Outlet boundary conditions as pressure outlet after stable flow calculation convergence

For a system of non-linear partial differential equations (PDE's) the iterative method with an initial guess of solution helps to achieve converged residuals. Turbulence properties where chosen as intensity and hydraulic diameter where the diameter of test section mentioned. Also, 101325 Pa. value given for 'Pressure' for all cases. This defines the pressure initialized with atmospheric pressure inside the system. The above values are required to apply for reference-controlled volume. Hence, usually one must choose the available cell zone mesh as reference continuum using 'Reference Zone' drop menu. For example, for all cases in this study, for 'Reference Zone' drop menu, 'surface_body' option was chosen

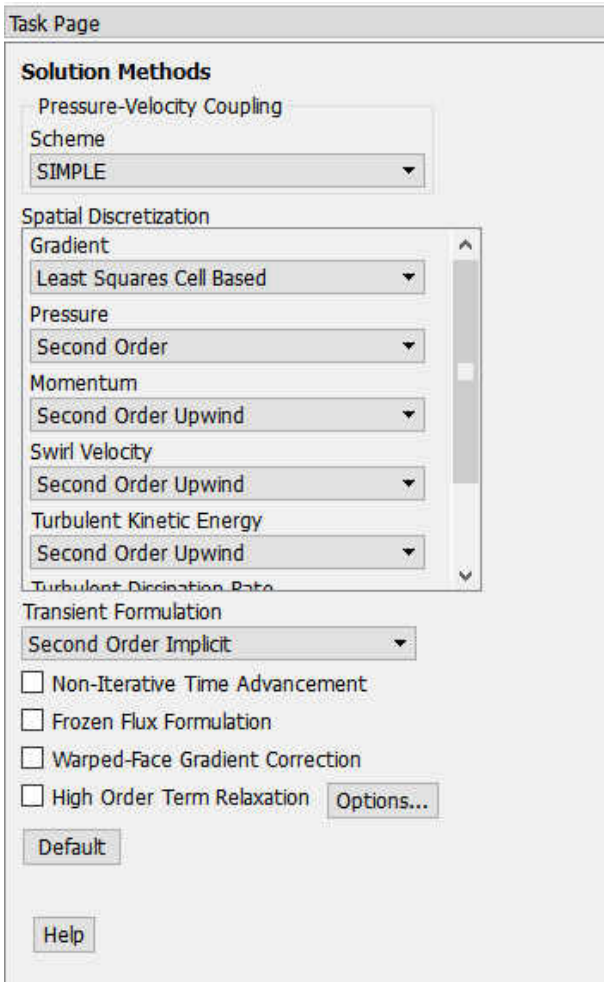

Figure 5.12. Solution method task page, the pressure-velocity scheme, and integral equations discretization are defined here.

5.3.4 Solving method setup

'Solution Methods' task page is second most critical part of the computational setup after 'Boundary Conditions' task page. The boundary conditions are required to define physics based characteristic values for sparse matrix based Numerical schemes are one of the essential parameters while setting up successful computational analysis. An optimized programming algorithm is required to solve these equations to achieve cost saving time reducing simulations with accurate physics and mathematics based solutions.

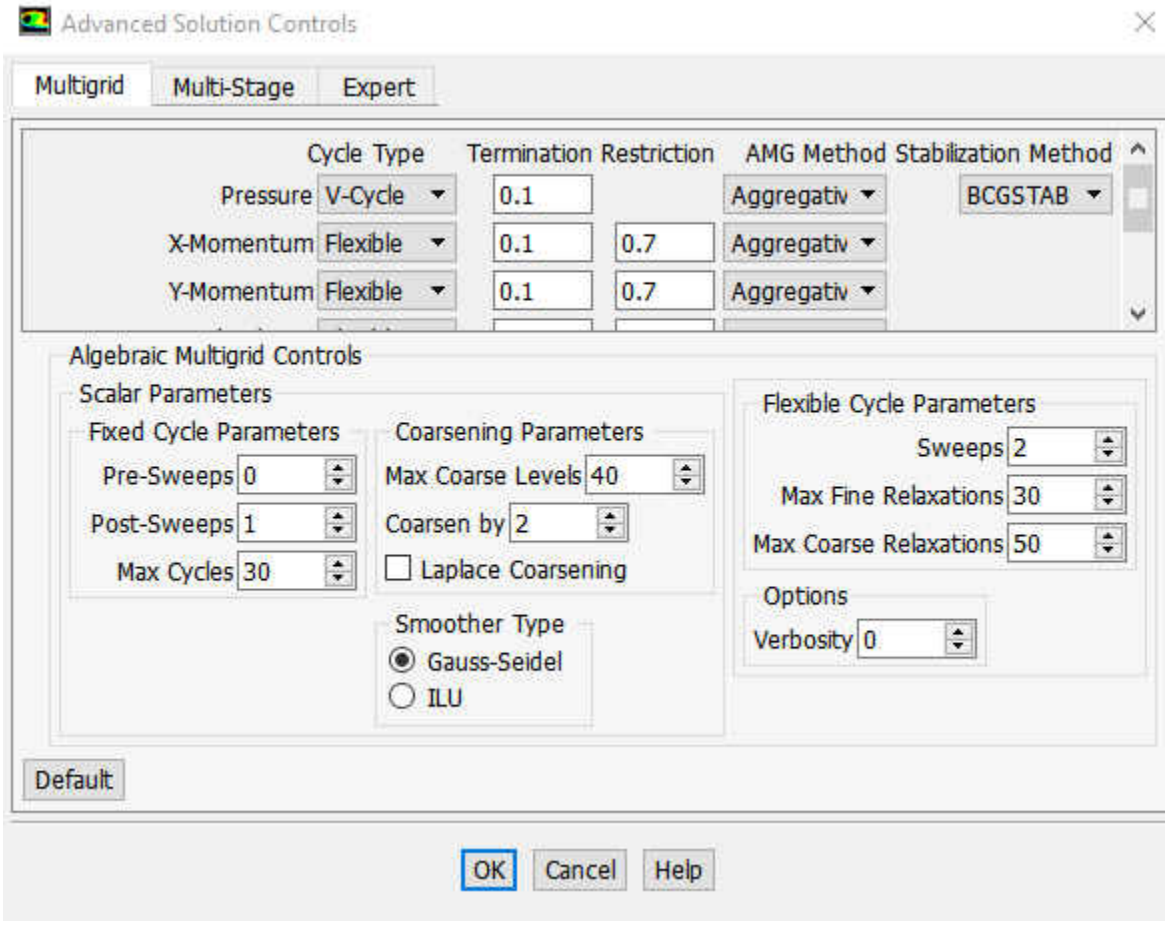

Figure 5.13. Solution methods control option, the AMG solver with the CGSTAB method, is selected.

We defined Algebraic Multigrid (AMG) solver with 2D bi-conjugate gradient stabilized method (CGSTAB) for residual convergence, this also allows defining error verbosity level of 3 which helps to reduce the computational error tolerance further helps to compute great accuracy answers. Further for pressure and velocity coupling Semi-Implicit Method for Pressure-Linked Equations (SIMPLE), with QUICK (Quadratic Upstream Interpolation for Convective Kinematics) algorithm scheme is used for solving pressure correction, continuity and momentum, turbulent kinetic energy, turbulent eddy dissipation rate, and energy equations. For spatial discretization, the least square cell-based gradient is selected. Warped-face gradient correction is applied to remove the solution singularity in the solver equation discretization algorithm over non-conformal meshes. The higher order terms relaxation was given for optimizing simulation time with 0.75 relaxation factor for all variables.

The ‘Solution Control’ allows optimizing the individual variables during analysis of flow field to avoid divergence. While using QUICK scheme for solving sparse matrix non-linear equations, the third and higher degree terms of equations develop error accumulation in residuals leading residuals state of non-convergence. To avoid this, the pressure-based solvers provide facilitated access to individualistic solution control to all variables, relaxation factor for all variables. Hence, during the simulation, these numbers can be decided by trial and error. All equations are decided to solve under equation dialog box. No changes are made under ‘solution limit’ dialog box.

For ‘Monitors’ task page the monitor's setup is completed with residuals monitoring and some additional variables monitoring, The pre-existing residuals monitoring routine edited with convergence criteria as none for all turbulence, energy, and momentum residuals. Since This is 2D simulation environment, the surface monitors were decided to setup instead of volume based

monitors. Inlet flow, Outlet flow, and iteration established pressure correction with axis parameter were decided to monitor for all iterations.

The Solution Initialization task page defines values for flow variables and initializes the flow field to these values. Hybrid Initialization method was chosen for all kinds of cases. This helps to optimize the simulation time by interpolation of randomly selected values for the flow field based variables such as temperature, pressure, turbulence, and so forth. Further, it automatically patches the corresponding cell zones with all averaged values.

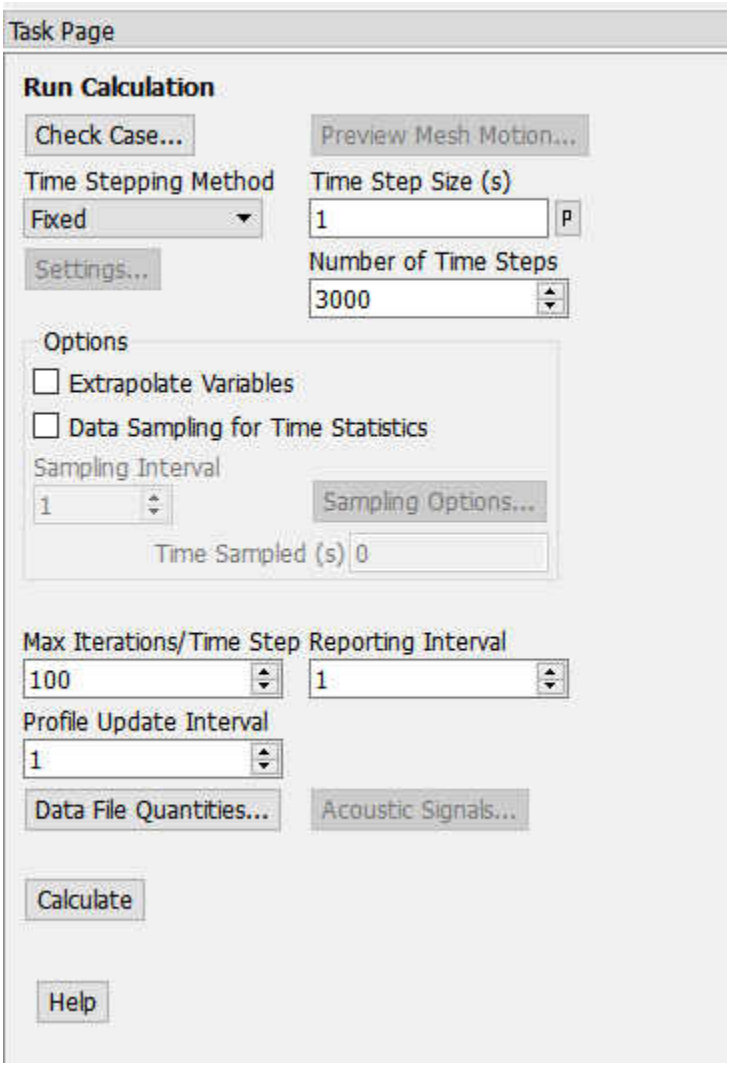

Figure 5.14. Calculations task page, final step of setting up flow simulation

5.3.5 Calculations setup

The solver calculations are performed at 'Run Calculation' task page, where transient, pseudo-transient, steady-state calculations are done as per the requirement of physics-based answers. First, the case is checked to find the anomalies in algorithmic setup and programming based errors by the program, which can find by re-reading the user developed backend code. In these single-phase flow calculations, the time-stepping method is applied for transient simulations. Adaptive time stepping methods is made functional for optimization of residuals towards convergence. For each time step, 100 iterations were given which will render 100 converging iterative values for the single time step. Similar to this, 3000 time-steps were chosen to simulate the flow field. This will generate $100 \times 3000 = 300{,}000$ iterations over the period of all flow rates employed in single test section simulation.

5.4 Two-Phase flow setup

To mathematically model the Two-Phase flow, the multi-phase flow model setup is executed which is similar to single-phase flow with additional code activation and a moderate amount of algorithm change. Founded upon a previous literature review [42], [56], [33], it was decided to use 'Multi-Phase-Eulerian' model for this research study. However, solving entire multiphase model without prior knowledge to volume fractions of both gas and liquid flow increases the burden on computing resources along with the certain assurance of divergence. Hence, it was decided to solve initial two-phase flow solution to notice the specific volume fractions for the given mass flow rates for better convergence. There are multiple methods to obtain initial solution calculations for the Eulerian model, but in this study, the calculations further carried using mixture model. First, the model was set up using mixture model with slip velocities, which are derived from experimental mass flow rates. As the flow leads to divergence the slip velocity

ratio is changed, until there is an assurance for convergence, after that the volume fraction was computed using algebraic co-relation between slip velocities and volume fraction. The discovered value further decided to validate using the setup of entire Eulerian-Multi-phase model for that same case, without activation of the model based volume fraction equation. This volume fraction equation is founded upon meshing elements which are in the form of integral for all elements in the given control volume, in other words, the given equation is an elemental form of partial differential equations. Hence, the volume fraction calculations derived from PDE is different from volume fraction derived from experimental analysis based co-relations of previous researchers. After achieving intimal all residuals convergence, the volume fraction equation is activated by substituting the calculated value from previous researcher's co-relations. The Flowfield further initialized with new equations residuals. This further perform continuum mechanics calculations, along with sudden computational jump of residuals. A CFD engineer can locate possibility of divergence during calculations. After multiple iterations, the volume fraction residuals show convergence, if the residuals do not show convergence, then volume fraction changed until the correct volume fraction value is found. Moreover, thus this procedure is carried for few flow rates; using linear interpolation method, the remaining volume fraction values are found.

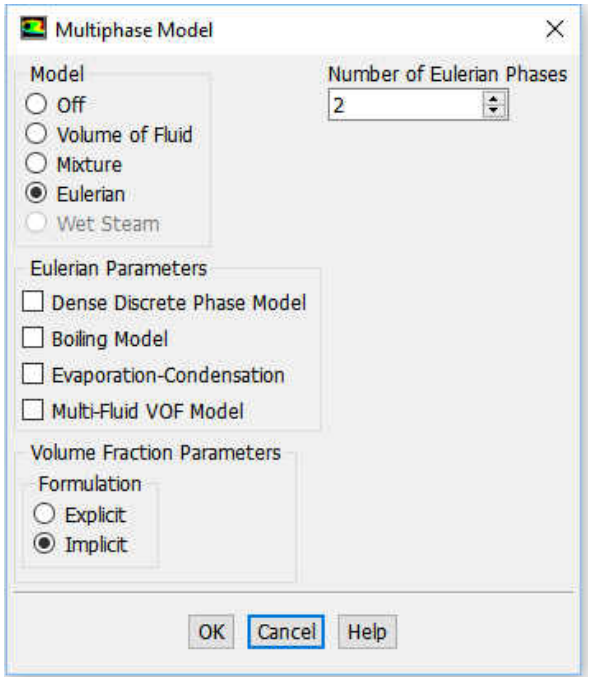

Figure 5.15. Eulerian multiphase model option, implicit formulation chosen, and number of Eulerian phases selected as two

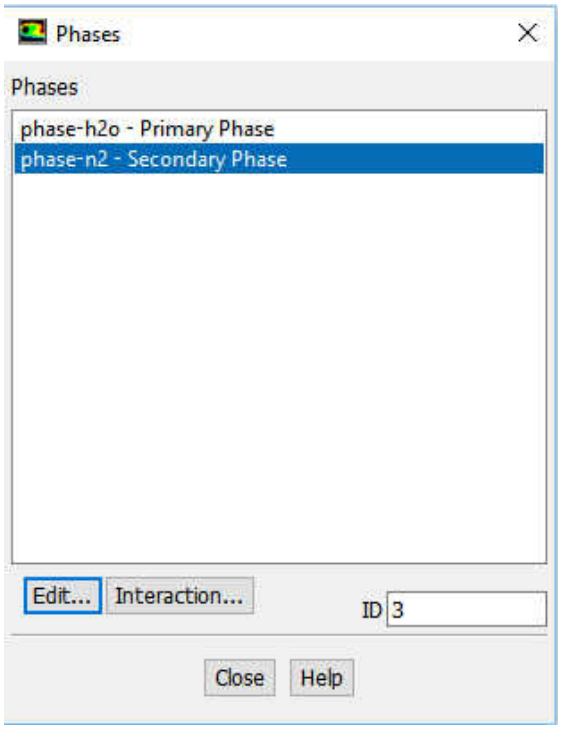

Figure 5.16. The defined phases for multiphase model

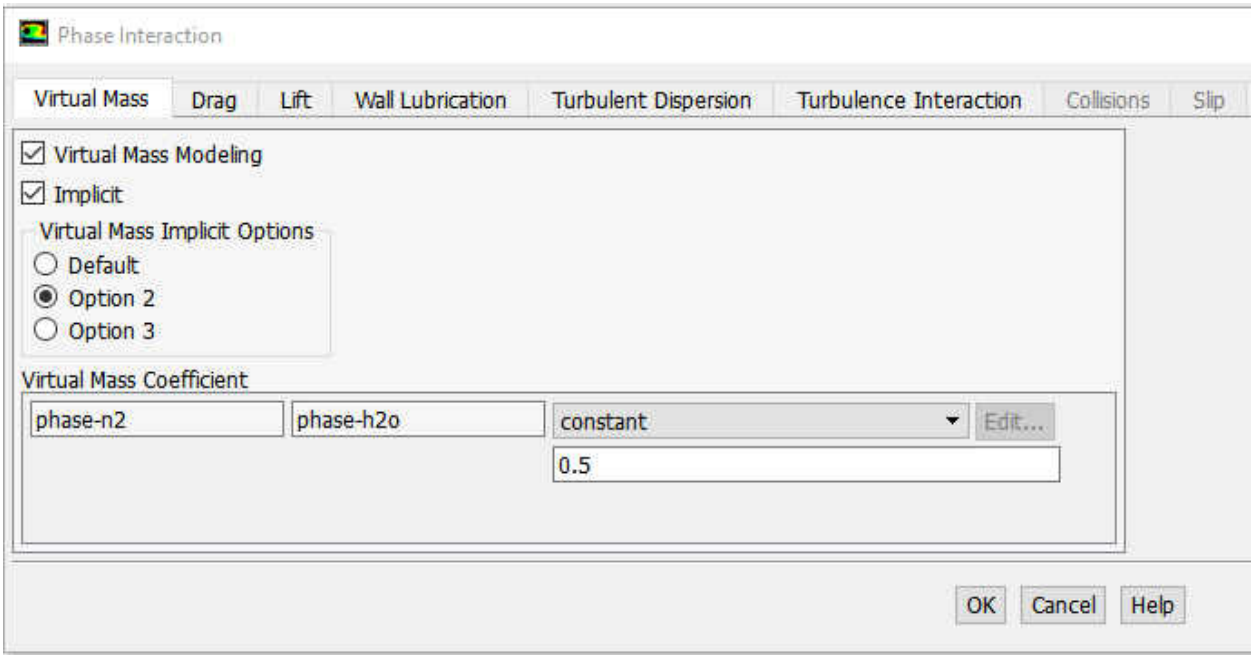

Figure 5.17. Model selection for single-phase flow where Reynolds Stress Model (5-equation) is shown

After volume fraction calculations, the multi-phase flow model setup is executed which is similar to single-phase flow with additional code activation and a moderate amount of algorithm change. For two-phase flow, Multiphase model activated with implicit volume fraction formation through 'model setup' dialog box, which decides the solution convergence based on the previous time-step and provides better accuracy. Also, the interface modeling is selected as dispersed, as the interfacial pressure correction equation is not considered due to developed flow is considered as stable. A number of Eulerian phases are given as two since it is two-phase flow. Before this, the solver selection setup is identical to single-phase flow, which is 2D, axis-symmetric, pressure based Navier-Stokes (p.b.N.S.) solver, with no gravitational force, and absolute velocity formation. For further model development, the materials are defined as phases acting as continua. Under phase

selection dialog box in task page tree, the phase p which is dominating during flow analysis, chosen as water (H_2O) which is represented as phase (l) and phase q, selected as Nitrogen (N_2) which is decided to perform as an ideal inert gas with equilibrium thermodynamic quantity. Here it is considering as phase(g). Hence, phase p is defined as $l = liquid = Water$ and phase q is defined as $g = gas = Nitrogen$. The particle diameter value for secondary phase, water is 0.0003937 inches. The interchange mechanisms selected within phase interactions dialog box. First, implicit virtual mass modeling is activated with virtual mass computing algorithm 'option two' which provides a hybrid solution of turbulence in each computational cell and does not allow momentum residual to diverge. Then, for drag mechanism in multiphase flow model with phase-interaction-drag mechanism Schiller-Neumann [60], mechanism chosen for drag coefficient. Throughout the analysis, the lift kept as constant with a value of 0.5. This lift and drag coefficient acts on individualistic particle of flow as an interfacial phase interactions, in other words the pressure developed on water, particle within flow field also exerts pressure on nitrogen particle using virtual drag and lift mechanisms.

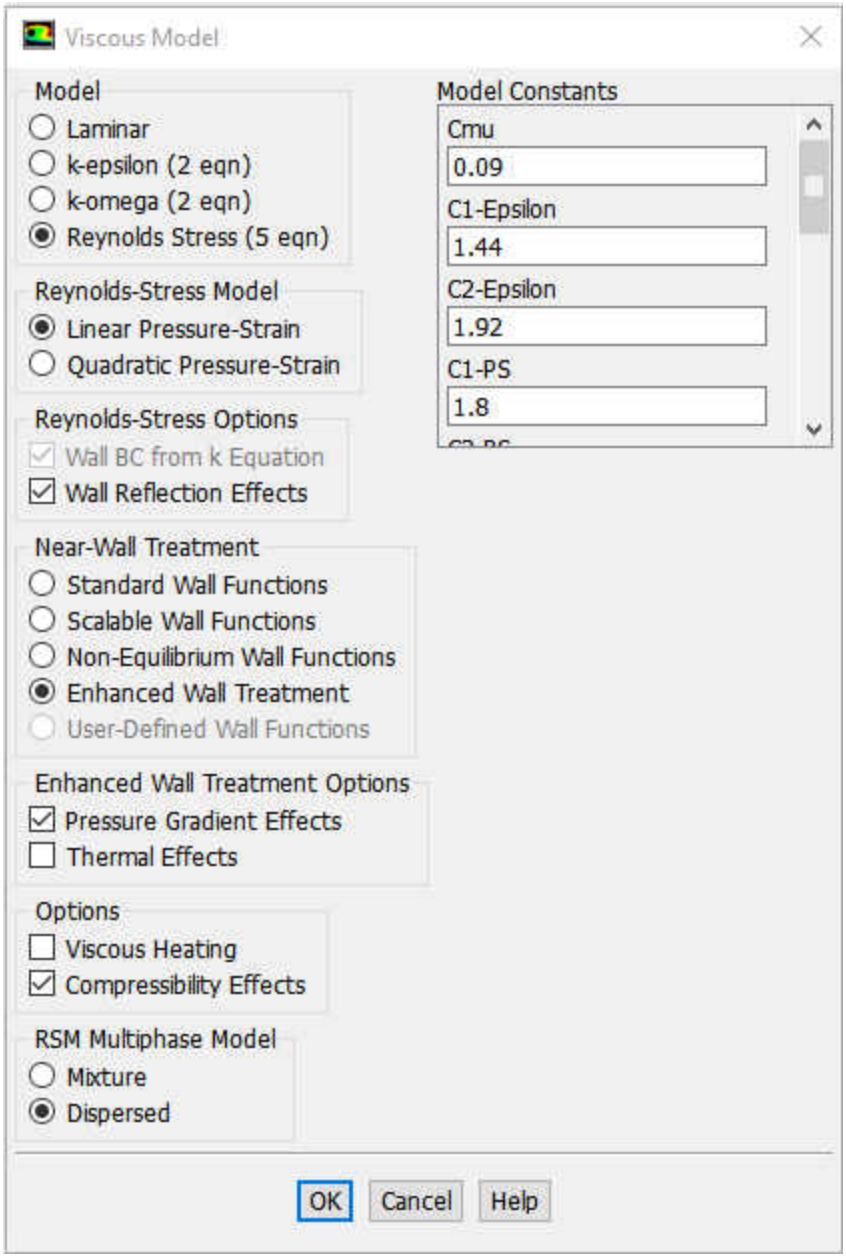

Figure 5.18. Model selection for multiphase flow model where Reynolds Stress Model (5-equation) is shown with a dispersed parameter, compressibility effects are accounted.

Since the nitrogen is modeled as an ideal gas, the thermodynamic properties play a critical role in simulation environment thus energy equation model is activated. Reynolds stress turbulence model is activated. Under which the linear pressure strain, wall reflection effects, enhanced

pressure treatment for the wall with pressure gradient effects. Dispersed phase model selected for RSM multiphase model. Compressibility effects are accounted for phase interactions. This includes identical values for model constant, along with it, Dispersion Prandtl number, energy Prandtl number, wall Prandtl number are included for which the values are 0.75, 0.85, 0.85 respectively. Materials are Nitrogen and water-liquid, as discussed earlier.

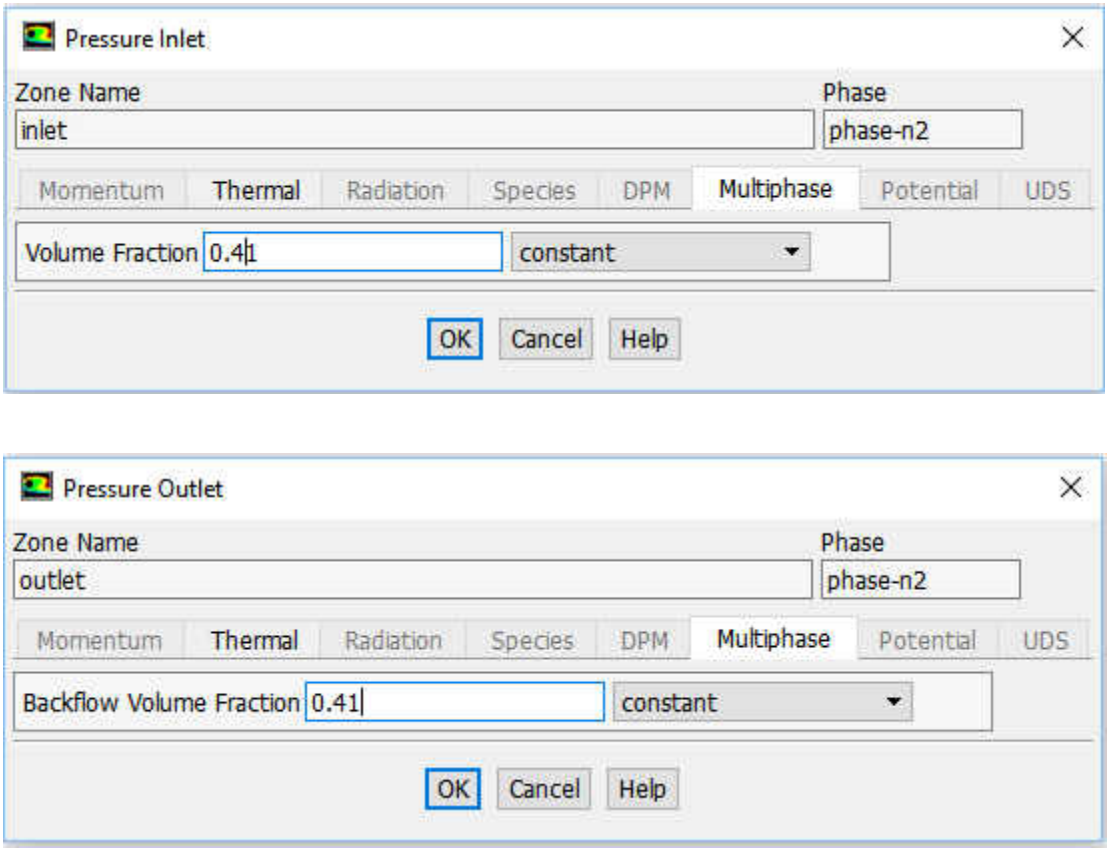

Figure 5.19. The volume fraction boundary conditions, which is one of the critical options to set successful multiphase model.

The boundary conditions are different compared to single-phase flow, first identical boundary conditions are decided to apply for two-phase flow, but the multiphase flow model does not support 'Outflow' boundary condition since the flow field is assumed regarding sparse matrix equations as stable. While multi-phase model equation system develops the flow from unstable to

stable conditions over a period steps but does not pre-condition it as stable. Therefore, the satisfactory boundary conditions found out to be, at inlet application of experimentally found inlet pressure value, and correspondingly at outlet, pressure value, which is discovered from experimental analysis. These boundary conditions are mentioned in Table 5-2. Further, to use this boundary condition, under 'cell-zone condition' tab, the atmospheric pressure value is provided as zero, proving that the continuum is mathematical 'pressure driven flow.'

While choosing solver solution algorithm, Pressure-velocity coupling scheme is selected as 'Coupled', without coupling all volume fraction equations. Higher order terms relaxation is given. Spatial discretization schemes for individual variables for selected solver is discussed further in the table (number).

Table 5-3. Spatial discretization schemes for individual variables concerning solver selection for the multiphase model.

Spatial Discretization Schemes	
Gradient	Least Squares Cell-Based
Density	First Order, Upwind
Momentum	QUICK (Quadratic Upstream Interpolation for Convective Kinematics)
Volume Fraction	QUICK (Quadratic Upstream Interpolation for Convective Kinematics)
Turbulent Kinetic Energy	QUICK (Quadratic Upstream Interpolation for Convective Kinematics)
Turbulent Dissipation Rate	QUICK (Quadratic Upstream Interpolation for Convective Kinematics)
Reynold's Stresses	First Order, Upwind
Energy	QUICK (Quadratic Upstream Interpolation for Convective Kinematics)

The pseudo-transient algorithm is activated, along with 'Warped-Face Gradient Correction.' Algebraic Multigrid Solver (AMG) with aggregative time stepping method is selected

since the model parameters are implicit. Similar to single-phase flow BCGSTAB (bi-conjugate gradient stabilized method) is selected.

Hybrid initialization with 1600 time-steps are given for analysis at the start with a time-step value of 1s, but the residual convergence achieved at 800^{th}- time step. Then the residual convergence criteria is turned off for further calculations, for more accurate answers.

5.5 Solver Automation and batch processing.

The Experimental analysis for single-phase flow was done with four different test sections, including ten different liquid flow rates for each section. Thus, a single-phase computational analysis generates almost forty graphs of static pressure across the axis. These graphs only explain sudden expansion phenomenon; another forty graphs explain sudden contraction phenomenon. Thus, total eighty datasets describe just single-phase flow. For two-phase flow, the experimental analysis is operated using three test sections that are 0.375 inch - 0.5 inch, 0.315 inch - 0.5 inch, 0.19 inch - 0.5 inch at inlet and outlet respectively for sudden expansion, conversely similar test sections are used for sudden contraction phenomenon. Each test section adds fifty gas-liquid combinations of flow rates, hence 300 complete datasets occurred in total two-phase flow computational analysis. This encompasses the enormity of experimental as well as computational analysis of two-phase and single-phase flow. Every analysis takes approximately 19 to 30 minutes of real time. Hence, the massiveness of data indeed consumes an enormous amount of computational hours. Apart from that, the idealness of the program after finishing dataset calculations due to human inattention also augment the time of post-processing of data for further analysis. Hence, solver batch processing and automation were desired option to process the most of the data.

To process batch dataset processes, the stable non-divergence generating computational case was required. As mentioned earlier for both single-phase flow and two-phase flow, a single case was taken into consideration with all parameters and boundary conditions. With all kinds of diverging computational attempts. Then the favorable test conditions which show converging residuals with equivalent values of inlet mass flux and outlet mass flux, also inlet and outlet energy flux, although no heat transfer is involved in the simulation, were selected to study further. After certain value changes the case were studied whether the flux parameters changes within previously achieved time step iterations. Thus, another finalized case is developed with the same settings, which is considered as core case with the original computational setup. Further scheme language based its backend settings are studied to find the precise patterns. These patterns then converted to ANSI C language based UDF (User Defined Functions) for single-phase flow. While for two-phase flow after studying patterns, scheme and lisp language constructed journal-setting files are created.

After studying the cases, for single-phase flow, where transient (time-dependent) iterative time stepping is applied, the User Defined Functions (UDF) is constructed by using ANSI C language. Due to C language support to solver software is as per 'C/C++ 99 standards', while loop in UDF generates bugs, which ultimately creates compilation and interpretation errors. Thus, with nested if-else loops, the UDF's are generated for execution of 10 flow rates equally established within 3000 transient time steps. In this, the new mass flow rate is provided to iterative equation calculating system after 300^{th} time step. The following algorithm snippet is typical compiling UDF of particular single-phase flow simulation.

#Include -> udf.header

Define profile for mass flow rate;

```
Begin loop
        Select face for udf application;
        Get real flow time from system calculations;
        If flow time is less than 302 time step seconds
            Print flow time;
            Print designated mass flow rate;
            Looped flow rate value
                Flow rate = the assigned value for that set of time steps;
            End loop
        Else if flow time is between specific time steps
            Print the time step number with simulation time;
            Change the mass flow rate value to new value, for further time steps;
            End loop
        End else if
End loop
```

With this simple loop, the process of changing designated mass flow rate and the corresponding value of pressure at the inlet is controlled for 3000 time-steps. This further helps to eliminate the ideal time between two flow rates, assisting as a catalyst for boundary conditions to encapsulate all flow rates in a single simulation. After every 250 time steps, the residual shows linearizing behavior, additionally showing a balance of energy and mass fluxes across the flow field. Hence, with the additional tolerance, the AutoSaving of case and data file is performed after every 300^{th} time step and for every 301^{th} time step the UDF changes the boundary condition value for corresponding variables.

For two-phase flows, the instead of UDFs, Journal files are generated which consumes less computational memory for every iteration compilation, since instead of request and response data through the compiler or interpreter, the journal file injects TUI commands which are written in Lisp language easily in core scheme and C language based code. While performing two-phase

flow calculations, the time steps are executed with a pseudo-transient algorithm with certainty in linearized steady-state flow field for optimizing flow simulation time. Hence instead of developing steady state flow based UDF, it was more easy to construct set of scheme language based journal commands, which were decided to execute individual cases constructed with individualistic experimental data values. A sample code snippet to perform the desired operations on the particular gas flow rate and the associated all liquid flow rate cases is given below:

```
/file/read-case Case_Name.cas  (/*file is imported from same folder to solver environment*/)
/solve/initialize/hyb-initialization (/*Same file is initialized with hybrid initialization*/)
solve iterate 1100  (/*File Further iteratively solved for 1100 time steps */)
/file/write-case-data Case_Name.cas yes (/*same file is overwritten with newly generated data*/)
/file/write-settings Case_Name.txt yes (/*Case specific settings are saved for further utilization*/)
/file/read-case-data Case)_Name.cas yes (/*Again File is read along with data*/)
/plot/plot yes 'File_Specific_Pressure_Graph_Name'.out yes no no mixture pressure yes 1 0 axis()
(/* The graph along axis is plotted with static pressure as variable and data are written to file*/)
/file/write-case-data Case_Name.cas yes (/*again file is overwritten using same data*/)
```

Using above algorithm, the files were generated simulation specific data independently, along with static pressure profile graph using axis parameters. Using Iron-python console of FLUENT ACT (Accessories Customization Toolkit). An application was developed which collects all data from plot files of individual flow rates and stores them in large excel file.

CHAPTER VI

RESULT AND DISCUSSION

6.1 Experimental analysis

Pressure drop calculated from upstream linear trend-line subtracted from downstream trend-line because the difference between two trend-lines considered as pressure drop according to previous researchers. As the pressure profiles are plotted the pressure drop slope gradually elevates Che-Hao Yang [50]. Also, the superficial velocity of liquid particles as well as gas particles shows small compressibility; this superficial velocity shows co-relation with mass flow rate. Hence, the pressure drop shows proportionality to the increasing mass flow rates and superficial velocities of gas and liquid. Also with former researcher's conclusion, it is agreeable that sudden change in the area changes the mean velocity. This proportionality has seen in single-phase as well as two-phase flows. Here in this research, the results are shown based on a channel with $\sigma = 0.0784, 0.1444, 0.3844, 0.5625$ for single-phase flow, but for the two-phase flow, $\sigma = 0.1444, 0.3844, 0.5625$ are shown, and observed. Test channels are described based on area ratios, where $\sigma = 0.1444$ shows 0.19 inches(0.004826 meters) as inlet for expansion case while same diameter is used as outlet for contraction case. Similar to this, $\sigma = 0.3844$ explains 0.315 inches (0.008 meters) as inlet and outlet for expansion and contraction respectively, and $\sigma = 0.5625$ explains 0.375 inches (0.009525 meters) as inlet and outlet for expansion and contraction respectively. Based on the experimental data and the previous co-relations, the loss coefficient reduces as the velocity increases. Hence from the analysis, it shows that loss factor is inversely

proportional to the velocity of flow, and hence the kinetic energy of flow too. The experimental data shows loss coefficient is predictable for speed greater than 1.5 m/s. Conjointly, as per experimental analysis, loss coefficient is inversely proportional to area ratio of channels. Further, Reynolds number 6000 and above in test sections, the loss coefficient is shows predictable flat behavior. The computational and experimental analyses of single-phase as well as two-phase flows show agreeable report, in terms of minor loss coefficient.

Each experimental required flow rate ran three times to acquire accuracy in the experiments. After single-phase flow, a gas inlet connected to nitrogen cylinder through Alicat MC5 (range: 0.025 to 5) SLPM (Standard liters per minute) full-scale gas flow rate meter and controller. Five gas flow rates were chosen and applied to two-phase experimental conditions, which are; $0.025\ SLPM\left(\approx 0.00049\frac{kg}{s}\right)$, $0.1\ SLPM\left(\approx 0.0019\frac{kg}{s}\right)$, $0.5\ SLPM\left(\approx 0.0095\frac{kg}{s}\right)$, $1.0\ SLPM\left(\approx 0.019\frac{kg}{s}\right)$, $1.5\ SLPM\left(\approx 0.028\frac{kg}{s}\right)$., for each gas flow rate, 10 liquid flow rates accompanied. For contraction test section two-phase flow experiments, the same procedure followed by changing positions of the test section.

6.2 Computational analysis

The computational analysis shows the results for the channel with $\sigma = 0.1444, \sigma = 0.3844, \sigma = 0.5625, and\ \sigma = 0.0784$ based on experimental analysis. The numerical calculations show good agreement with current work and the previously done analysis by researchers. This further speculates that use of multiphase turbulence Reynolds stress model is effectively valid for two-phase flow computational fluid dynamics with the gas-liquid model. To perform the analysis on the regular lab based computer systems which has a low computing power, the turbulence intensity of flow is considered to be an average of 10% of overall turbulence based

CFD calculations. Hence the solver performs the calculations reduced to the factor of 10, which then considered while performing the overall analysis of data points.

6.2.1 Grid Independence Study (GIS)

The accuracy of CFD results can establish and validated with a dense grid(mesh) with excellent computational time. For grid independence studies, sudden expansion phenomenon with five different grid densities is selected for two different test sections, with area ratio $\sigma = 0.1444, 0.3844$, where the inlet diameter 0.19, 0.315 inches and outlet diameter 0.5 inches are established for calculations. Two-phase fluid flow with liquid mass flow rates are as $\dot{m}_l = 0.03 \frac{kg}{s}$ and the gas mass flow rate is $\dot{m}_g = 0.00049 \frac{kg}{s}$. (0.025 Standard Liters Per Minutes), and nitrogen volume fraction of 0.11 chosen for the boundary conditions using the experimental values. The $\dot{m}_l = 0.03 \frac{kg}{s}$ repersents Reynolds number of 7900 for channel section with area ratio 0.1444. Meanwhile, the $\dot{m}_l = 0.03 \frac{kg}{s}$ repersents Reynolds number of 4863 for channel section with area ratio of 0.344. The selected grid sizes for test section with $\sigma = 0.1444$ are (Figure 6.2), mesh 1 = 84416 Elements, mesh 2 = 392352 elements, mesh 3 = 873667 elements, mesh 4 = 998746 elements, and mesh 5 = 1166410 elements. In other section of two-phase flow (Figure 6.3), for which the area ratio is 0.3844, the comparision shows promising results similar to the results of test section with area ratio 0.1444. Five meshes were generated for test section with $\sigma = 0.3844$ with the elements count as follwing: mesh 1 = 101146 elements, mesh 2 = 421956 elements, mesh 3 = 911778 elements, mesh 4 = 1011146 elements, and mesh 5 = 1217113 elements. Next, similar procedure is followed as the test section with area ratio 0.1444, and optimum mesh is resulted.

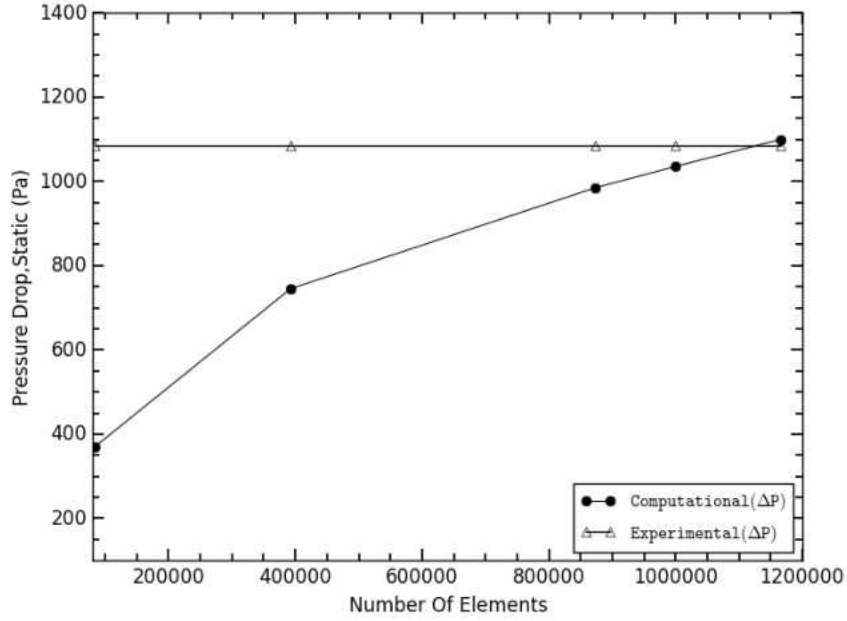

Figure 6.1. Pressure drop comparison for G.I.S. $\sigma = 0.1444, \dot{m}_g = 0.028\frac{kg}{s}, \dot{m}_l = 0.03\frac{kg}{s}$

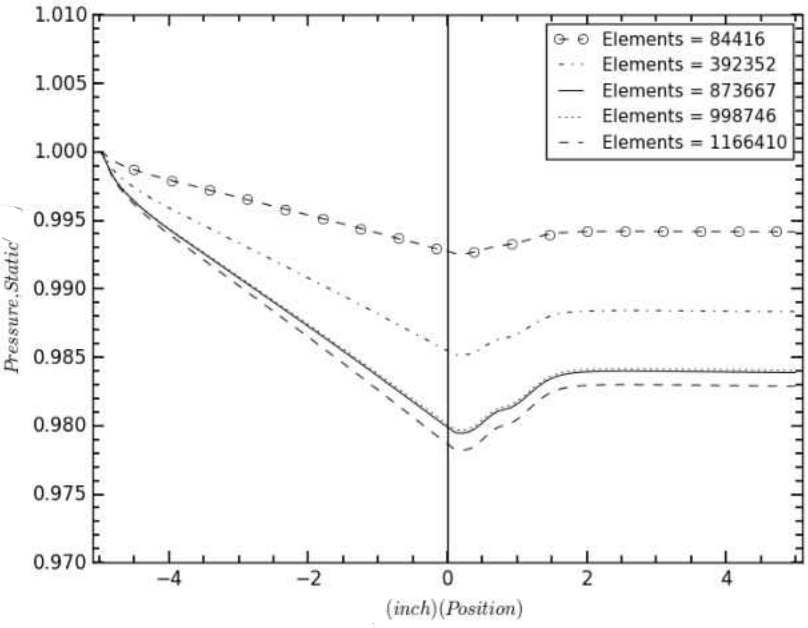

Figure 6.2. Pressure profiles comparison for G.I.S. $\sigma = 0.1444, \dot{m}_g = 0.028\frac{kg}{s}, \dot{m}_l = 0.03\frac{kg}{s}$

The following Figure 6.1, Figure 6.2, Figure 6.3, Figure 6.4, are generated using two-phase flow analysis. The figure shows pressure profiles generated using a different number of elements(cells) and figures show pressure drop calculated using these pressure profiles by computational methods and its comparison with experimental pressure drop. Mesh 4 and Mesh 5 shows more accurate and desired results but the computational time and cost increases with increasing number of elements. In Figure 6.2, the 873667 (all quad based) elements show agreeable and promising results towards grid independence studies.

In Figure 6.3, pressure drop changed drastically from mesh 1 to 3, but after mesh three the change in pressure drop is almost negligible compared to the change in the number of elements. Also, its value is well established at 5.7% error value of experimental value for given two-phase flow case.

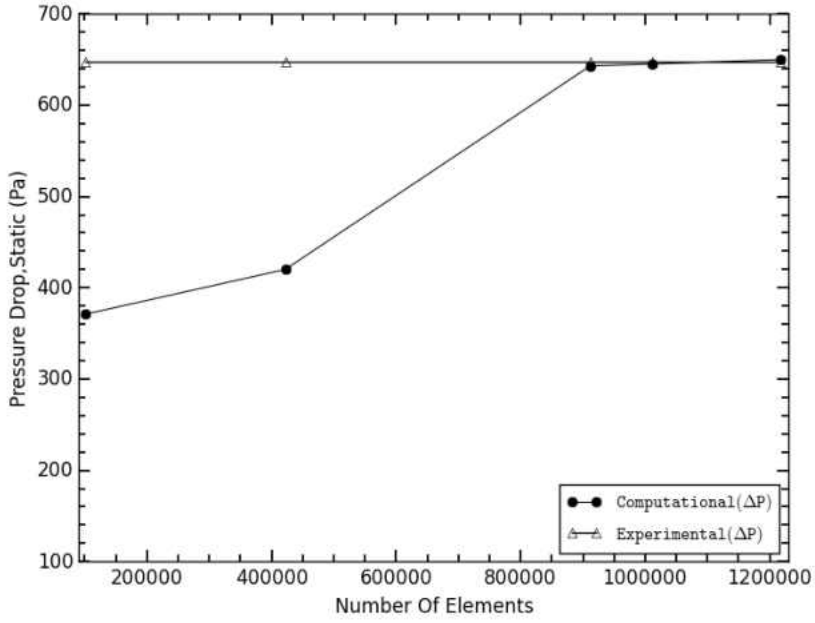

Figure 6.3. Pressure drop comparison for G.I.S. $\sigma = 0.3844, \dot{m}_g = 0.028\frac{kg}{s}, \dot{m}_l = 0.03\frac{kg}{s}$

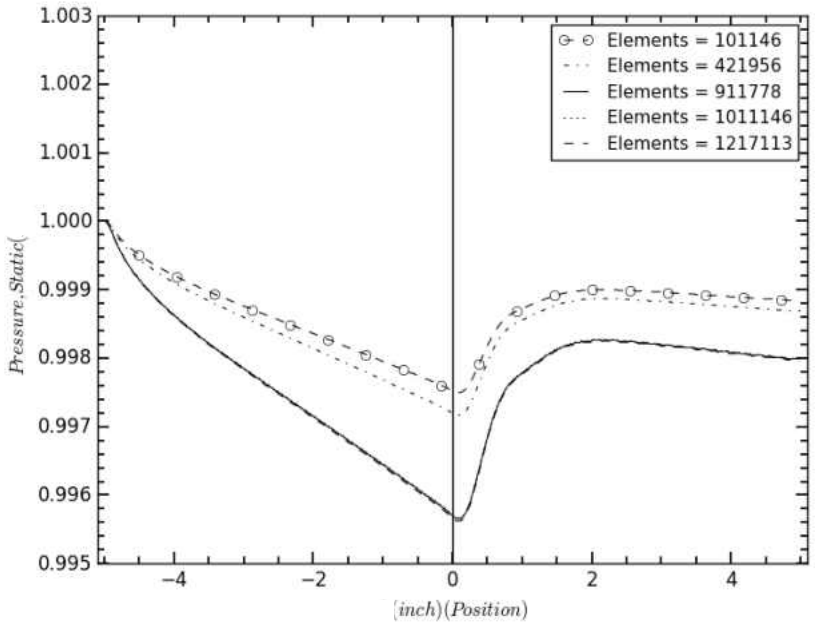

Figure 6.4. Pressure profiles comparison for G.I.S. $\sigma = 0.3844, \dot{m}_g = 0.028\frac{kg}{s}, \dot{m}_l = 0.03\frac{kg}{s}$

The following figures show the pressure profiles plotted with multiple meshes with singular boundary conditions for all cases. In Figure 6.4, the pressure profile with maximum elements show distinctive space between other pressure profiles, also using this pressure profile, the calculated pressure drop value show absolute zero percentage deviation from the experimental value, but the time consumption and the computational energy consumption is vast, also due to low memory resource on system, the entire system freezes/ hangs over non-definitive time period. Hence discarding the mesh with 1217113 elements, and 1011146 Elements, i.e. mesh 5, and 4 respectively, the other meshes are decided to accept. After that mesh 3 with 911778 Elements show acceptable pressure drop difference of 5%, also consumes less computational resources. Hence the mesh 3 is accepted for test section with area ratio 0.3844.

For single-phase flow, the test section with $\sigma = 0.5625, and\ \sigma = 0.0874$ are decided to apply for grid independence study, the inlet in this test section is 0.375, and 0.14 inches respectively, while the outlet section is common which is 0.5 inches. Only single-phase continuum flow field with material as water is decided for analysis. For each test section 5 meshes are generated with different number of elements. For test section with $\sigma = 0.5625$ following meshes are costructed (Figure 6.8), mesh 1 = 332146 Elements, mesh 2 = 971076 Elements, mesh 3 = 1135748 Elements, mesh 4 = 1171341 Elements, and mesh 5 = 1237683 Elements. In other section (Figure 6.6), for which the area ratio is $\sigma = 0.0784$, 5 meshes were generated with the elements count as follwing mesh 1 = 71921 Elements, mesh 2 = 301146 Elements, mesh 3 = 783147 Elements, mesh 4 = 875746 Elements, and mesh 5 = 1000173 Elements. A case with single-phase fluid flow with liquid mass flow rates are as $\dot{m}_l = 0.03\frac{kg}{s}$ and no gas mass flow rate is chosen for the boundary conditions. The $\dot{m}_l = 0.03\frac{kg}{s}$ repersents Reynolds number of 4000 for channel section 0.5625 area ratio. Meanwhile, the $\dot{m}_l = 0.03\frac{kg}{s}$ repersents Reynolds number of 10715 for channel section 0.0784 area ratio.The results of pressure drop calculated as per procedure previously given.

The Figure 6.5, Figure 6.6, Figure 6.7, and Figure 6.8 show the expansion in test sections $\sigma = 0.5625, and\ 0.0784$ show the axial pressure profile, and pressure drop graphs generated using simulation results of meshes. five different grid densities (number of elements) were implimemted for single-phase flow grid indepence study for both test sections. For $\sigma = 0.0784$ in Figure 6.5, the comparision suggest that the pressure drop value for mesh 3 = 783147 Elements, mesh 4 = 875746 Elements, and mesh 5 = 1000173 Elements, does not show diffrence and its value resembles with less than 5% marginal error to the experimental value.

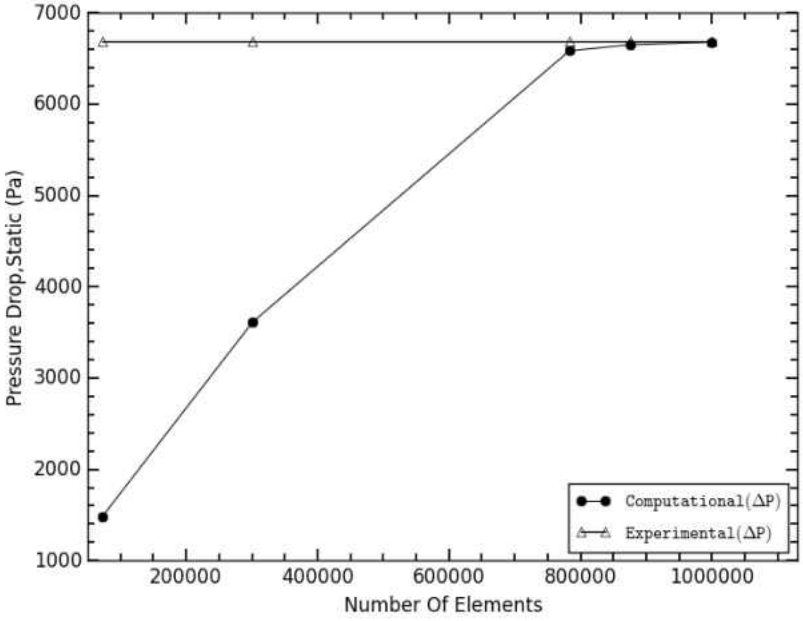

Figure 6.5. Pressure drop comparison for G.I.S. $\sigma = 0.0784, \dot{m}_l = 0.03 \frac{kg}{s}$

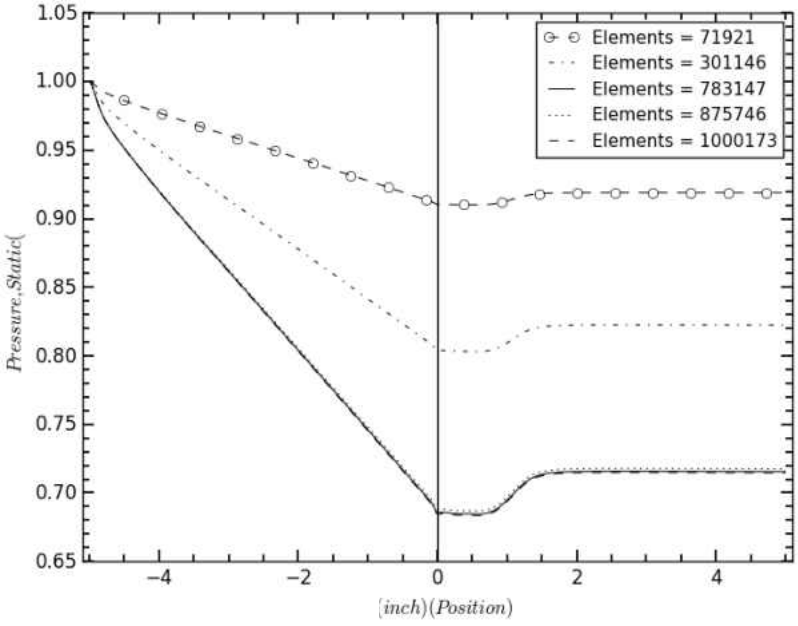

Figure 6.6. Pressure profiles comparison for G.I.S. $\sigma = 0.0784, \dot{m}_l = 0.03 \frac{kg}{s}$

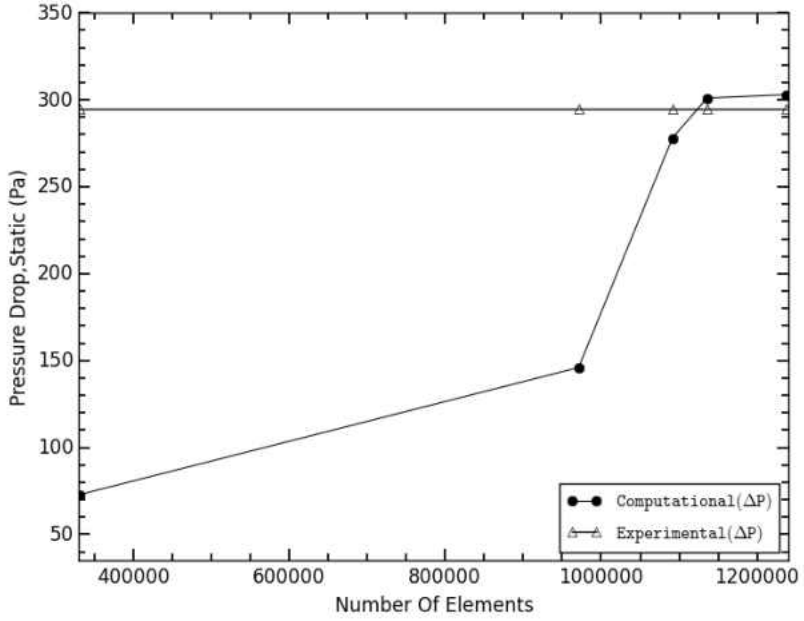

Figure 6.7. Pressure drop comparison for G.I.S. $\sigma = 0.5625, \dot{m}_l = 0.03 \frac{kg}{s}$

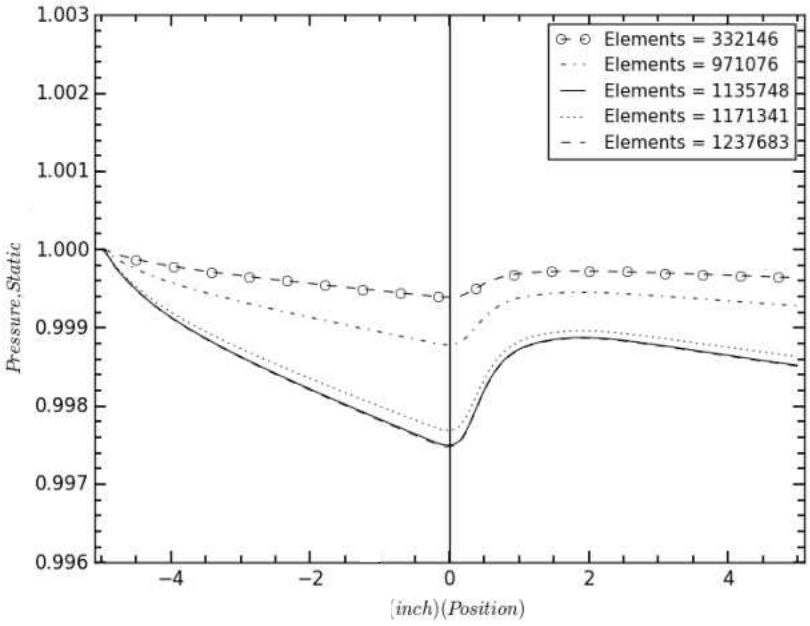

Figure 6.8. Pressure profiles comparison for G.I.S. $\sigma = 0.5625, \dot{m}_l = 0.03 \frac{kg}{s}$

While in the above Figure 6.7, the $\sigma = 0.5625$ test section show comparision of pressure drop value among all case studies suggest that the value for mesh 4 = 1171341 Elements, and mesh 5 = 1237683 Elements, show similar identity and less than 10% but greater than 5% comparision error with respect to experimental values.

Considering the computational time and resources, the future calculations performed with mesh 3 = 783147 Elements for $\sigma = 0.0784$ test section, and mesh 4 = 1171341 Elements for $\sigma = 0.5625$ test section are chosen for futher computaional analysis.

6.2.2 Flow Turbulence study:

Turbulence and other scalar quantities are chosen for study prior to single-phase and two-phase flow study. Test section with $\sigma = 1.4444$ was chosen for both contraction and expansion phenomenon. Flow rates such as 0.005 kg/s, 0.0225 kg/s, and 0.03 kg/s selected. solver analysis for single-phase flow calculation show accurate solver algorithm, hence results stability in calculations with better convergence and possibility of accurate prediction of turbulence and wall forces along channel wall. Thus, model comparison becomes easier.

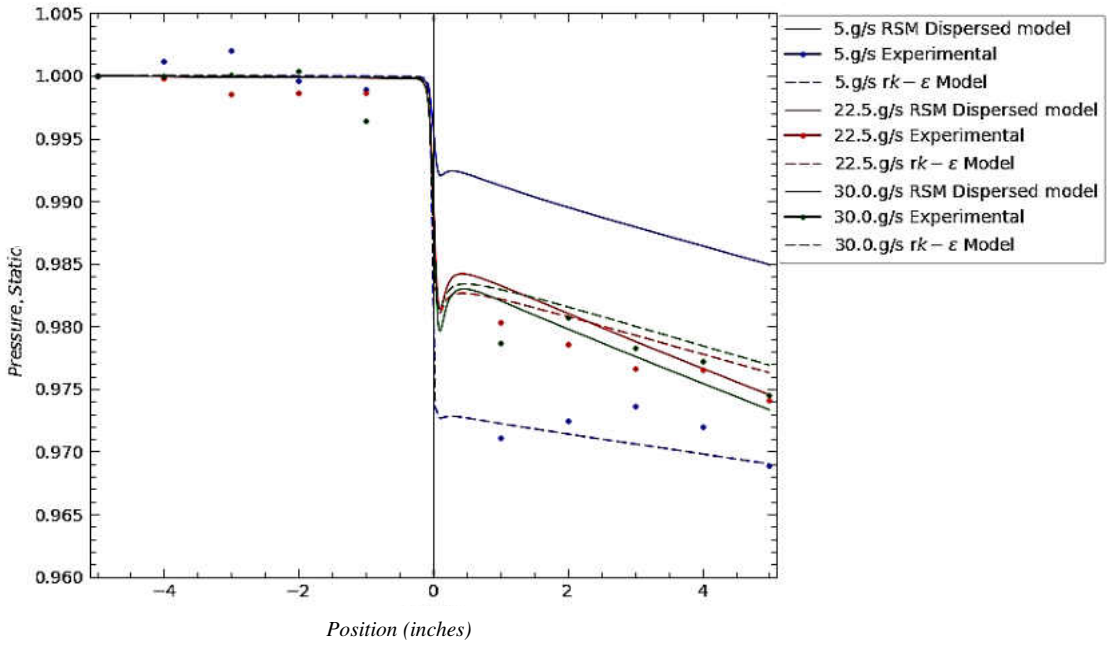

Figure 6.9: Single-Phase, $\sigma_{con} = 0.1444$, pressure profiles compared with experimental data for Turbulence model comparison

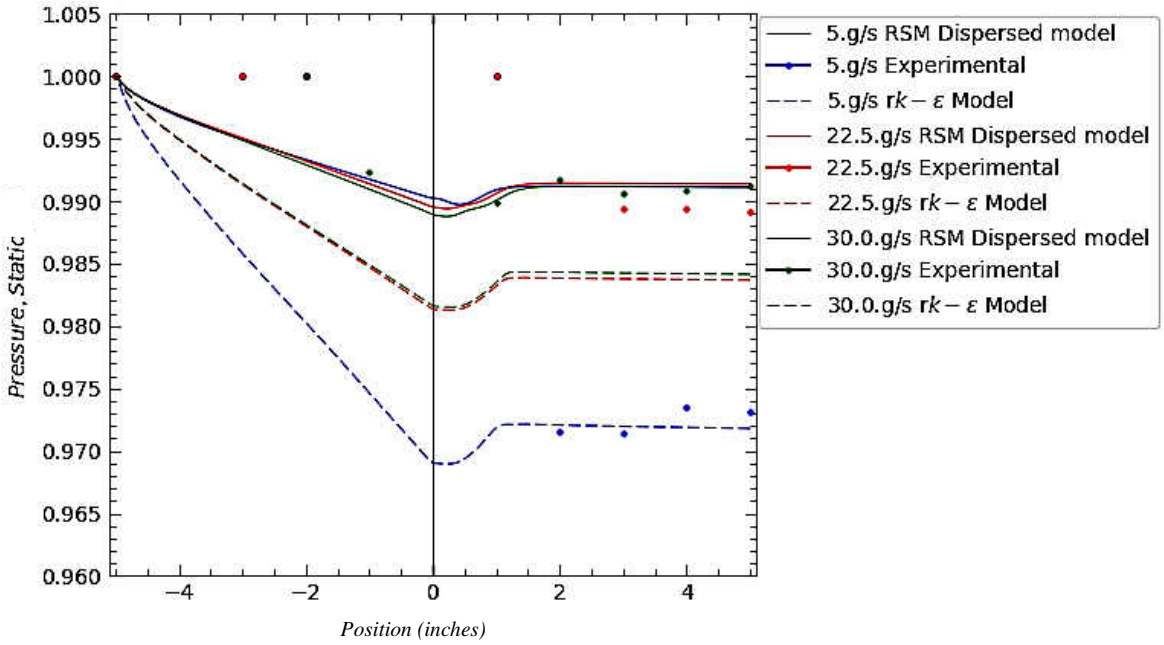

Figure 6.10. Single-Phase, $\sigma_{exp} = 0.1444$, pressure profiles compared with experimental data for Turbulence model comparison

The Figure 6.10, and Figure 6.9 show expansion and contraction phenomenon for test section $\sigma = 0.1444$ respectively. The Reynolds Stress Model(RSM) shows close relationship with the experimental data for 0.0225 kg/s and 0.03 kg/s flow rate calculations, while for 0.005 kg/s, $rk - \epsilon$ model shows better prediction. Here r stands for realizable. Hence, Although RSM model consumes time and computational resources, for the better accuracy, and considering higher flow rates, the RSM model is chosen for single-phase and two-phase flow analysis for sudden expasion phenomenon. The prediction of RSM model for higher flow rates show absolute accuracy, while lower flow rates show better agreement with $rk - \epsilon$ model. Due to lack of previous research with RSM turbulance model with respect to experimental datasets, and mejority of higher flow rate covenanting, RSM model is slected for turbulence evalution of Navier-Stokes equations for single-phase and two-phase flows for sudden contaction phenomenon.

6.2.3 Single-Phase flow

Single-phase flow considered for analysis for computational calculations before calculations of two-phase flow. Thus giving us more information about the mathematical behavior of basic overall incompressible fluid flow. Experimental analysis performed using pressure taps on the test sections, which provided the static pressure available at an instance. While the numerical analysis shows the pressure drop along with pressure profile across the axis of the same test channel, by solving integral flow governing equations. This also gives us an idea of turbulence and helps to understand better turbulence model for this research also, other scalar parameters such as wall shear stresses and volume fraction.

6.2.3.1 Expansion Pressure drop and pressure profile

Due to no presence of void fraction, all computational elements analyze single-phase flow with a single fluid association, and that is water(liquid). With the choice of the RSM model the flow analysis developed for all flow rates with boundary mentioned above conditions, and computational procedure. Test sections with $\sigma = 0.0784,\ 0.1444,\ 0.3844,\ 0.5625$ are used with expansion phenomenon for each section. These Figure 6.12, Figure 6.14, Figure 6.16 show the pressure profiles of fluid flow with selective mass flow rates. Also, Figure 6.11, Figure 6.13, Figure 6.15 further indicates the pressure behavior in channels, related to single-phase fluid flow. Also, pressure drop was calculated with these pressure profiles where interpolation of upstream points and downstream points is done.

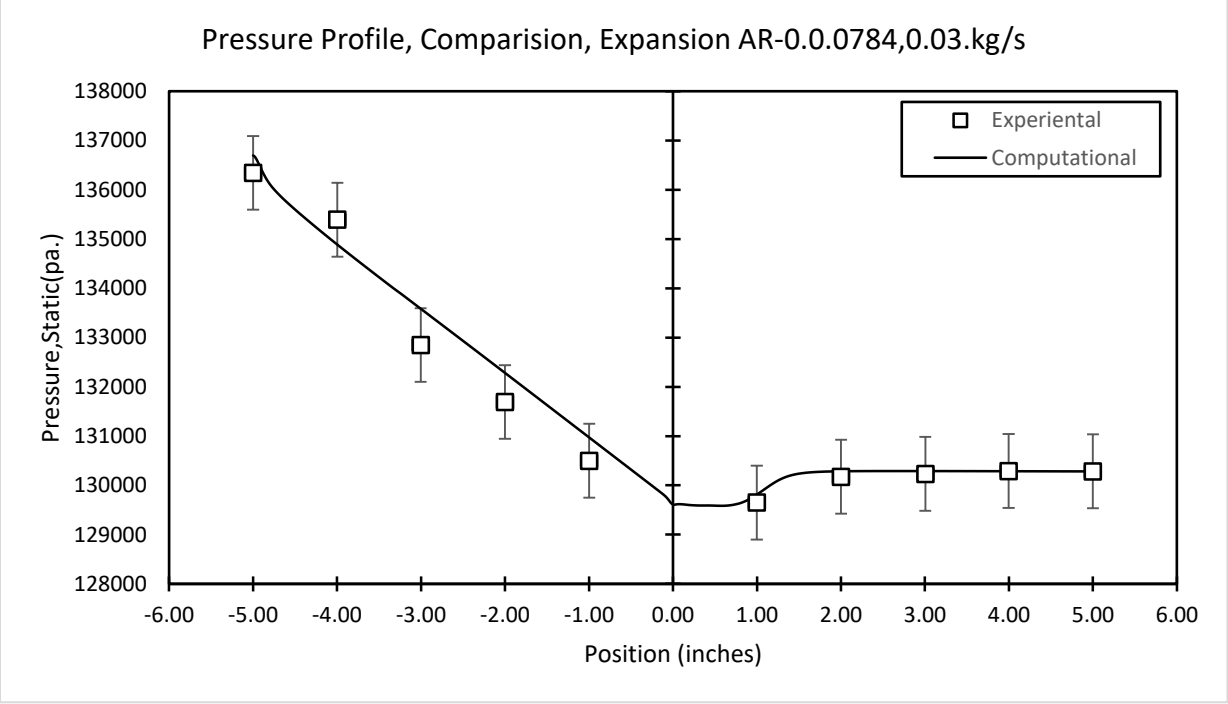

Figure 6.11. Single-phase flow pressure profile structure, compared with experimental data, σ_{exp} = 0.0784, $\dot{m}_l$ (kg/s) = 0.03

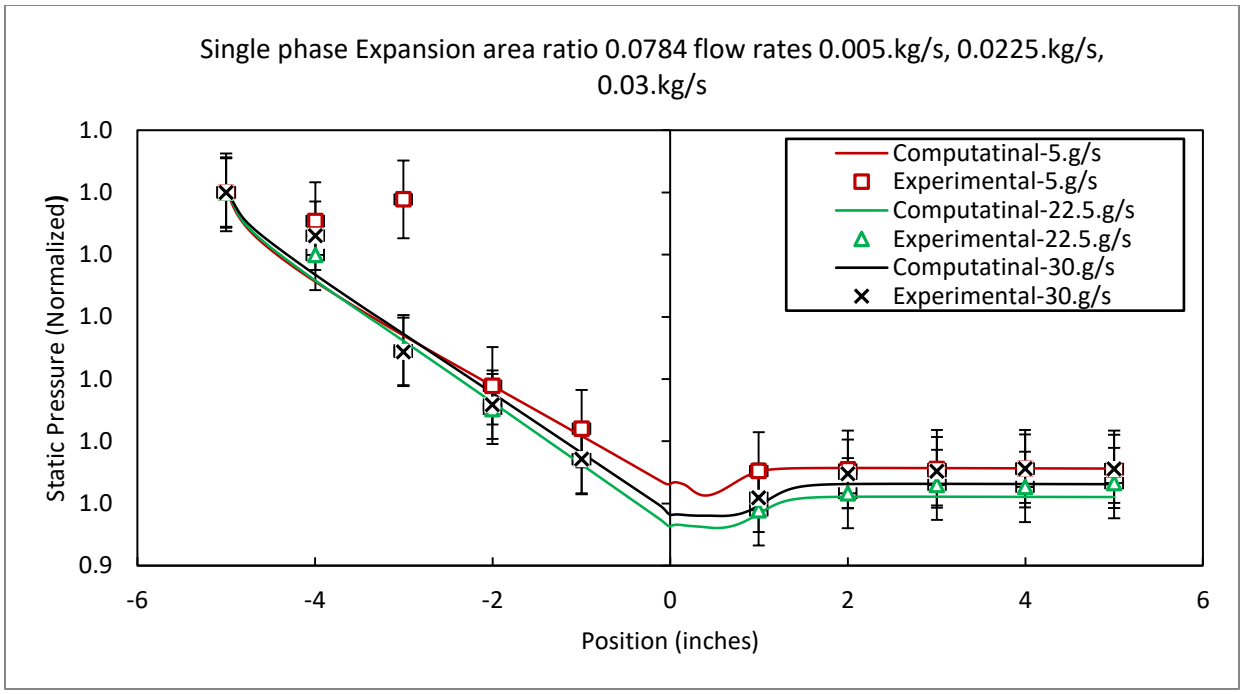

Figure 6.12. Single-phase flow pressure profile performance, compared with experimental data, σ_{exp} = 0.0784, $\dot{m}_l$ (kg/s) = 0.03, 0.0225, 0.005

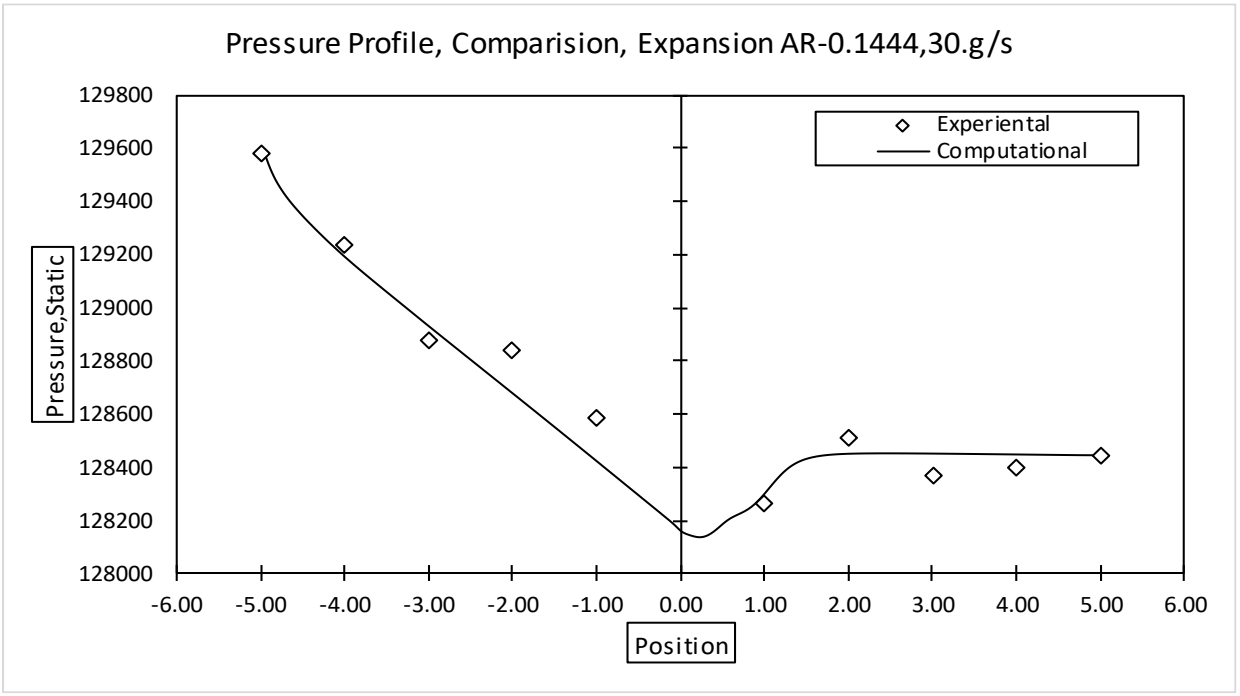

Figure 6.13. Single-phase flow pressure profile structure, compared with experimental data, σ_{exp} = 0.1444, $\dot{m}_l$ (kg/s) = 0.03

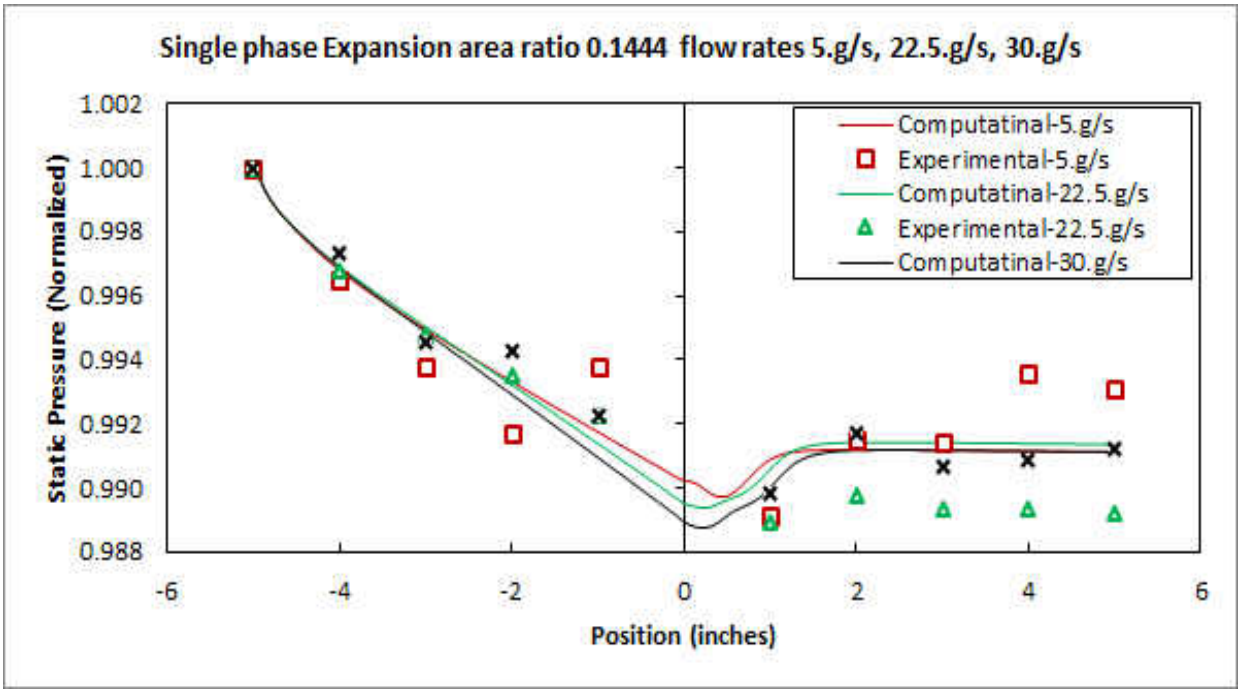

Figure 6.14. Single-phase flow pressure profile performance, compared with experimental data, σ_{exp} = 0.1444, $\dot{m}_l$ (kg/s) = 0.03, 0.0225, 0.005

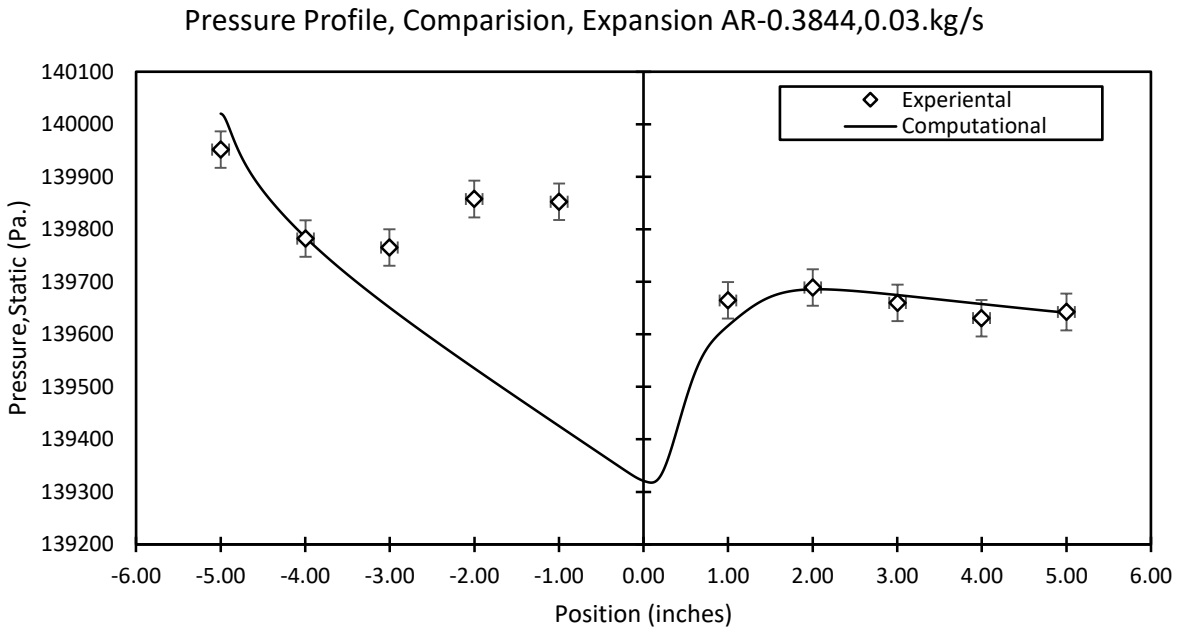

Figure 6.15. Single-phase flow pressure profile structure, compared with experimental data, σ_{exp} = 0.3844, $\dot{m}_l$ (kg/s) = 0.03

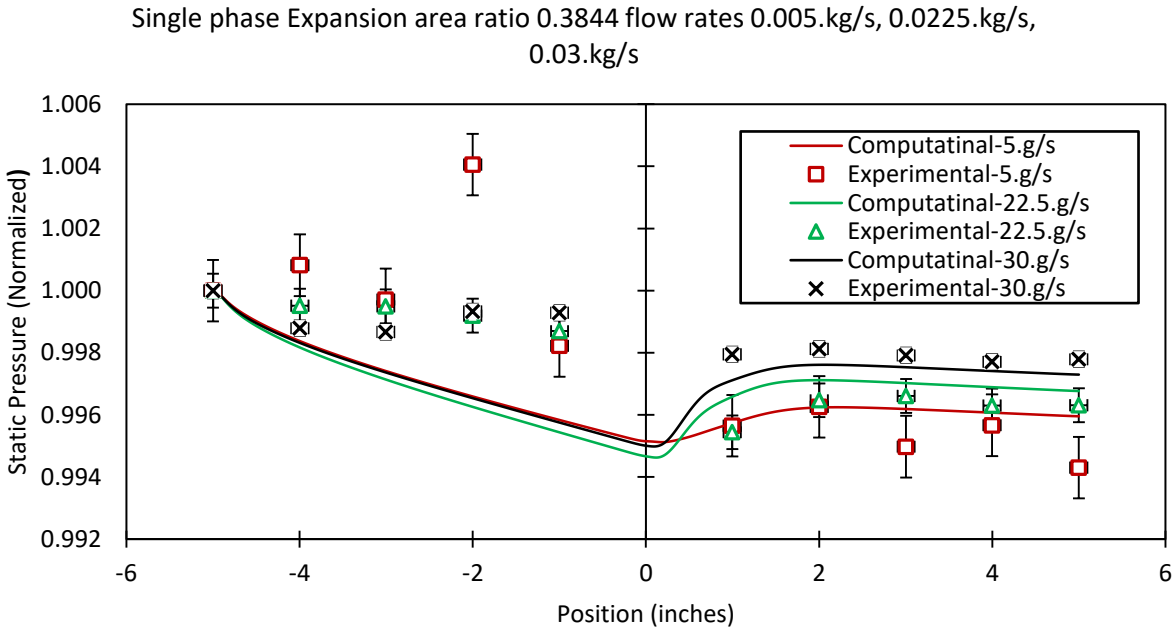

Figure 6.16. Single-phase flow pressure profile performance, compared with experimental data, σ_{exp} = 0.3844, $\dot{m}_l$ (kg/s) = 0.03, 0.0225, 0.005

The following Figure 6.17 shows the comparison of pressure profiles in all test channels by using single flow rate. In this graph, the pressure profile curve on downstream flow is different for the different section and as the statement is true for upstream flow, although the curves are normalized.

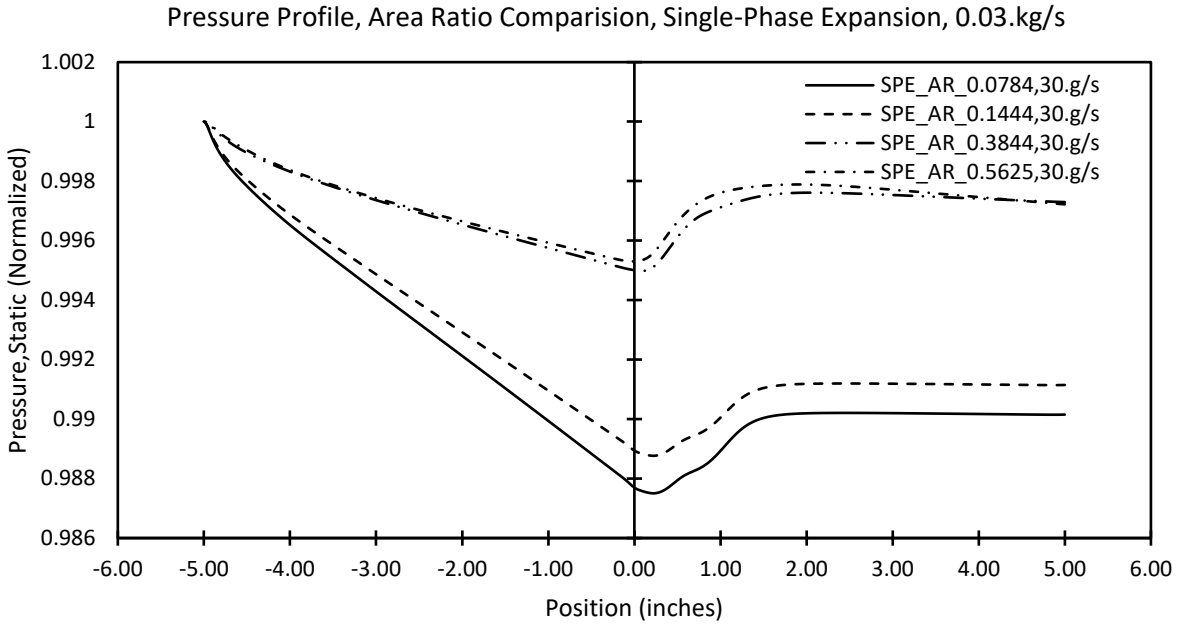

Figure 6.17. Single-phase flow pressure profile performance, comparison, σ_{exp} = 0.0784, 0.1444, 0.3844, 0.5625 $\dot{m}_l$ (kg/s) = 0.03.

In above Figure 6.17. Single-phase flow pressure profile performance, comparison, σ_{exp} = 0.0784, 0.1444, 0.3844, 0.5625 $\dot{m}_l$ (kg/s) = 0.03., the test section with $\sigma = 0.5625, and\ 0.3844$ show close resemblance of the pressure profiles, which show more elevation compaired to $\sigma = 0.1444, and\ 0.0784$ where the pressure profile show entirely different structure of curve for downstream flow with respect to previous test sections.

After calculating the pressure drop, it further analyzed with previous researcher's calculations and predictions against Reynolds number calculation. The increment in Reynolds number is directly proportional to the mass flow rate and velocities liquid. This is shown in Figure 6.18, Figure 6.19, Figure 6.20, and Figure 6.21, where in some cases the pressure drop provides excellent agreement concerning previous co-relations.

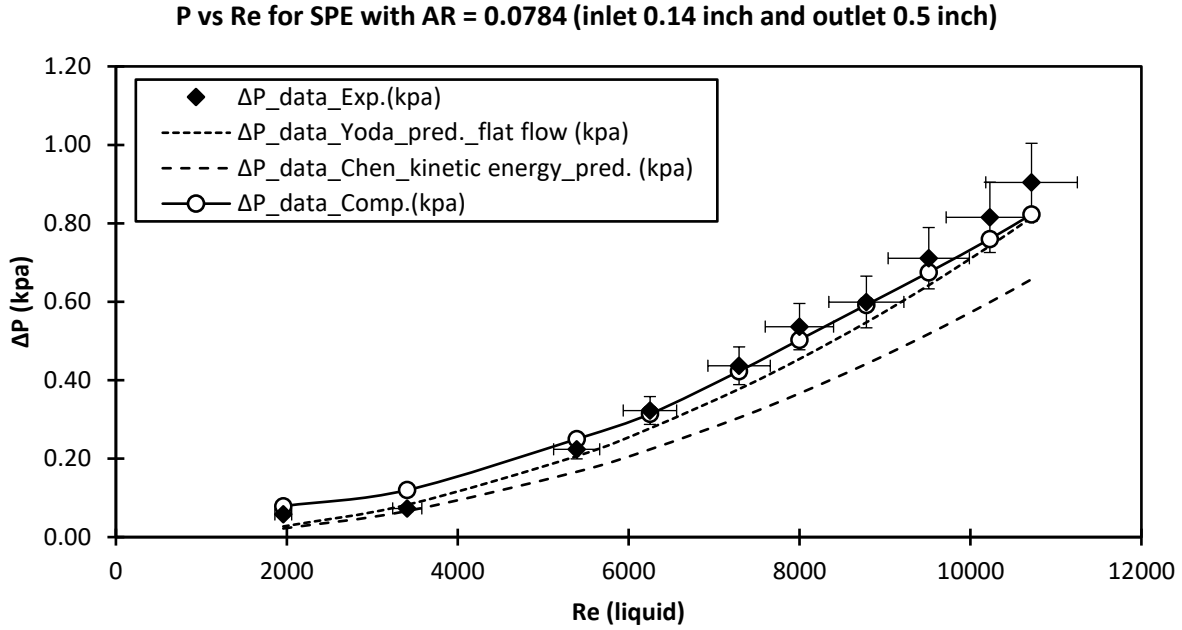

Figure 6.18. Single-phase flow pressure drop performance, compared with experimental data and other co-relations, σ_{exp} = 0.0784, $\dot{m}_l$ (kg/s) = 0.005 - 0.03

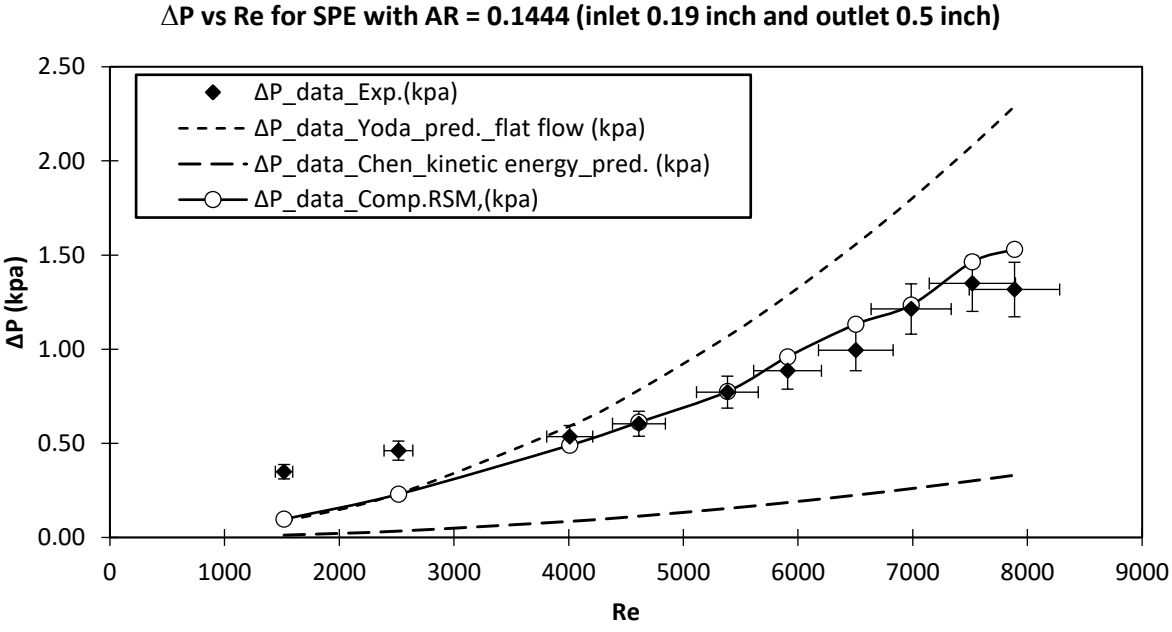

Figure 6.19. Single-phase flow pressure drop performance, compared with experimental data and other co-relations, σ_{exp} = 0.1444, $\dot{m}_l$ (kg/s) = 0.005 - 0.03

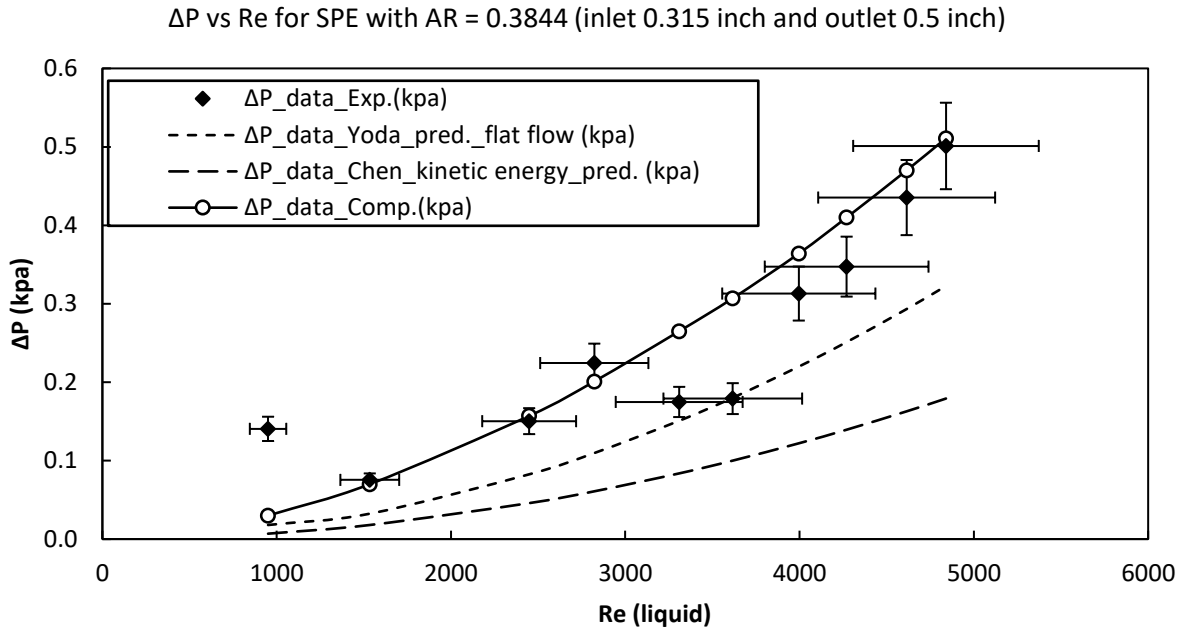

Figure 6.20. Single-phase flow pressure drop performance, compared with experimental data and other co-relations, σ_{exp} = 0.3844, $\dot{m}_l$ (kg/s) = 0.005 - 0.03

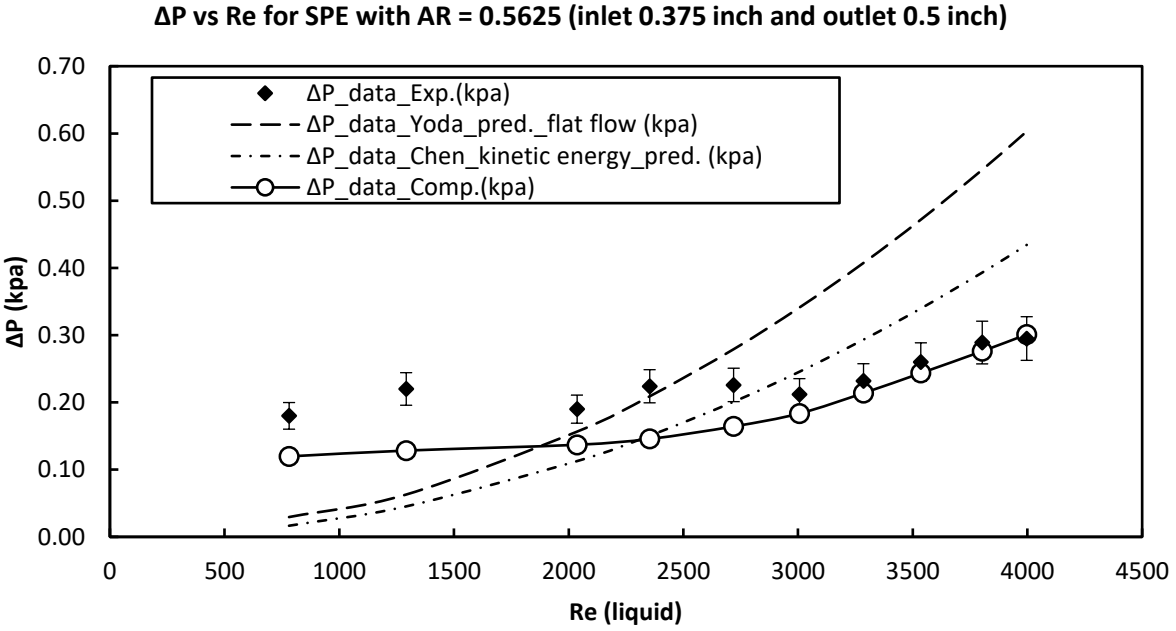

Figure 6.21. Single-phase flow pressure drop performance, compared with experimental data and other co-relations, σ_{exp} = 0.5625, $\dot{m}_l$ (kg/s) = 0.005 - 0.03

The agreement between computationally calculated and experimentally calculated Reynolds number shows 3% to 5% error. Hence, this further demonstrates the agreeable identicalness of computational and experimental calculations regarding pressure drop. Reynolds number in above graphs show lower value for lower pressure drops, in this region of all graphs the discrepancies are higher than the later part of the graph. For this, we can say that the correct theory based laminar conditions are difficult to maintain and thus the pressure drop might be higher compared to mathematical model calculations. While the higher range of Reynolds number, where the flow structure becomes fully turbulent, it is easy to maintain and achieve the desired pressure drop value.

6.2.3.2 Contraction Pressure drop and pressure profile

The single-phase flow analyzed using RSM model along with basic fluid flow model. Test sections with $\sigma = 0.0784,\ 0.1444,\ 0.3844,\ 0.5625$ are used with ten values of liquid flow rates for each section. Axial pressure profiles, which are shown in Figure 6.22, Figure 6.24, Figure 6.26, and Figure 6.28, were plotted and compared with experimental test results, which were collected using pressure taps on test sections. In addition, these pressure profiles were interpolated upstream points and downstream points and pressure drop were calculated. Because of sudden area change, pressure profiles look different for upstream and downstream. Further, the calculated pressure drops from pressure profiles were compared with experimental datasets as well as previous researcher's co-relations. Figure 6.23, Figure 6.27, Figure 6.29, and Figure 6.25 show largest flow rate comparison for other test sections followed by lower flow rate comparison with experimental results.

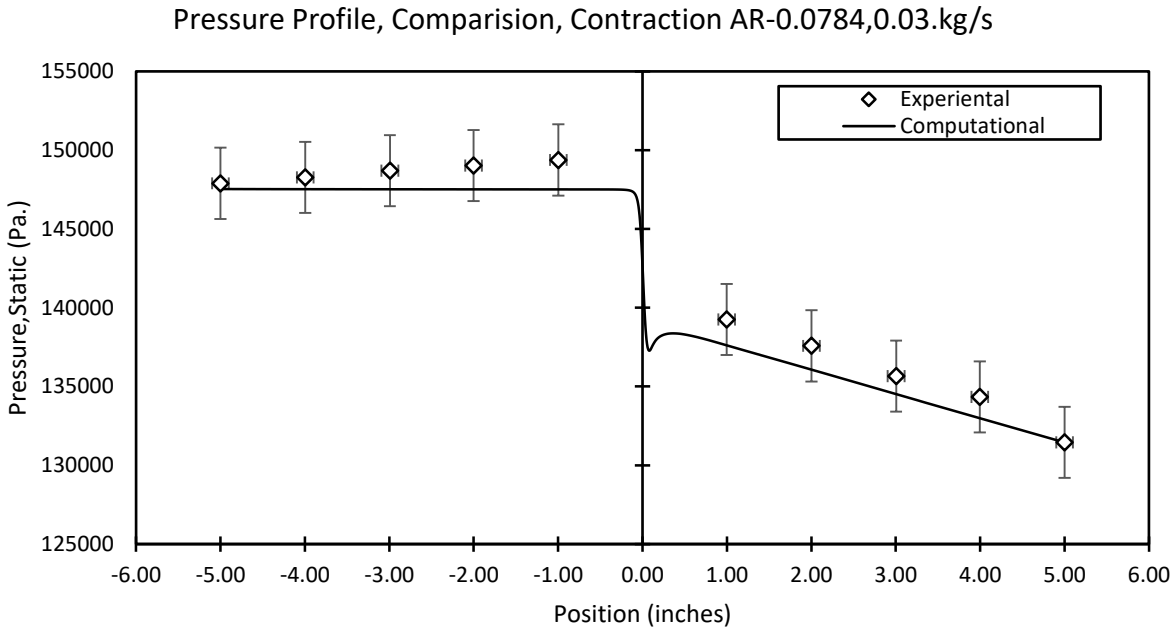

Figure 6.22. Single-phase flow pressure profile structure, compared with experimental data, σ_{con} = 0.0784, $\dot{m}_l$ (kg/s) = 0.03

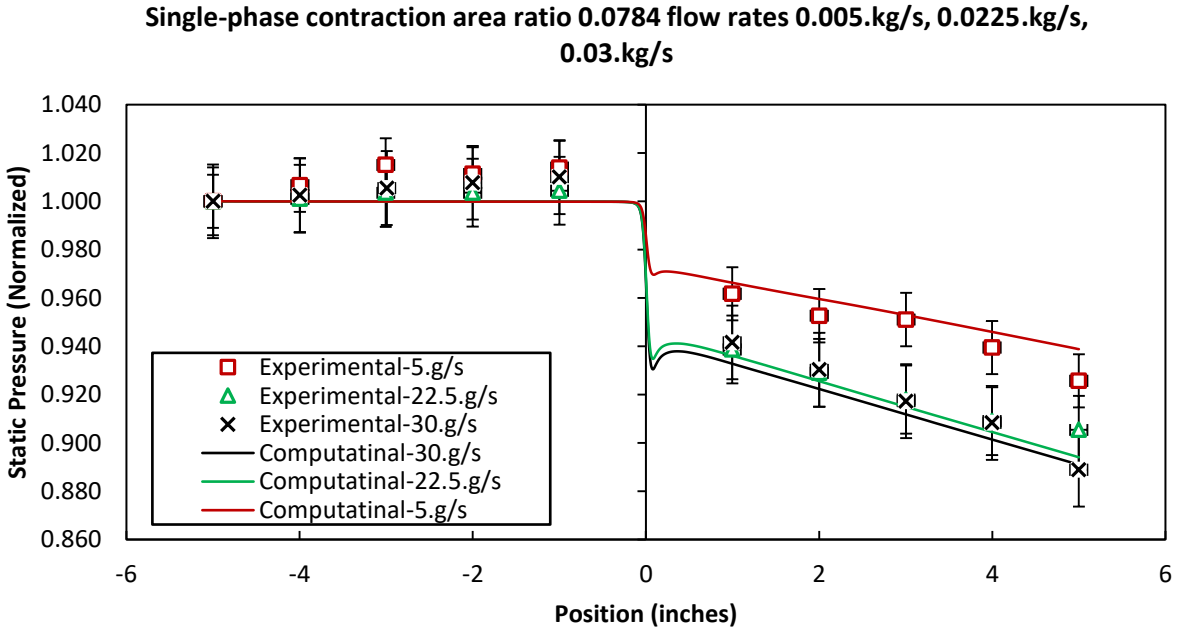

Figure 6.23. Single-phase flow pressure profile performance, compared with experimental data, σ_{con} = 0.0784, $\dot{m}_l$ (kg/s) = 0.03, 0.0225, 0.005

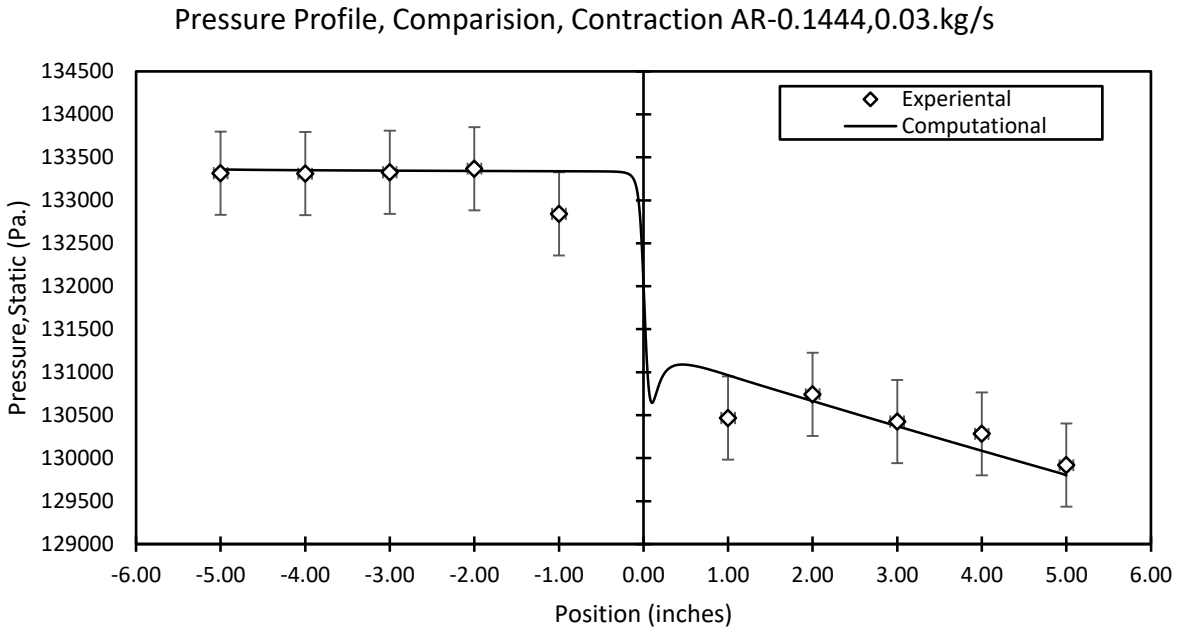

Figure 6.24. Single-phase flow pressure profile structure, compared with experimental data, σ_{con} = 0.1444, $\dot{m}_l$ (kg/s) = 0.03

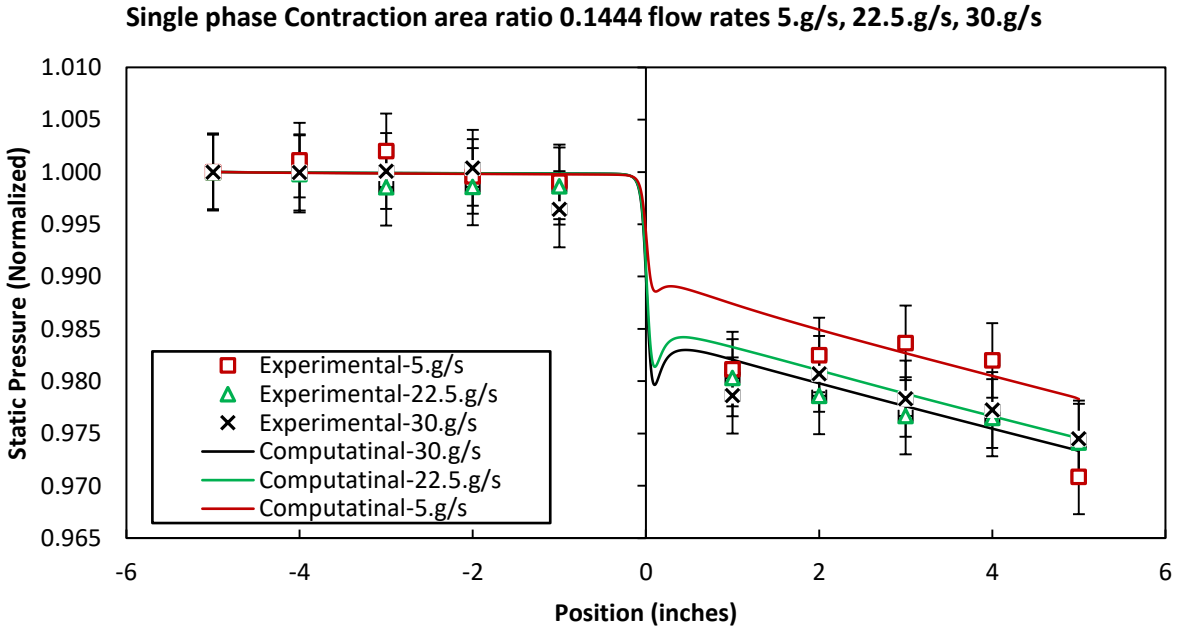

Figure 6.25. Single-phase flow pressure profile performance, compared with experimental data, σ_{con} = 0.1444, $\dot{m}_l$ (kg/s) = 0.03, 0.0225, 0.005

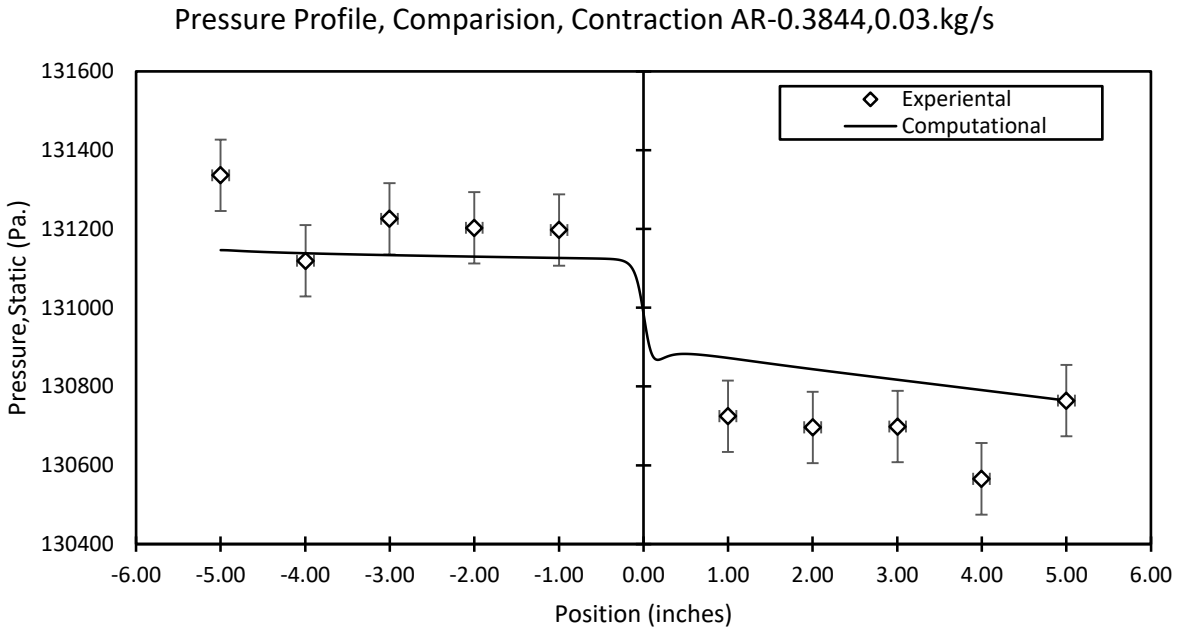

Figure 6.26. Single-phase flow pressure profile structure, compared with experimental data, σ_{con} = 0.3844, $\dot{m}_l$ (kg/s) = 0.03

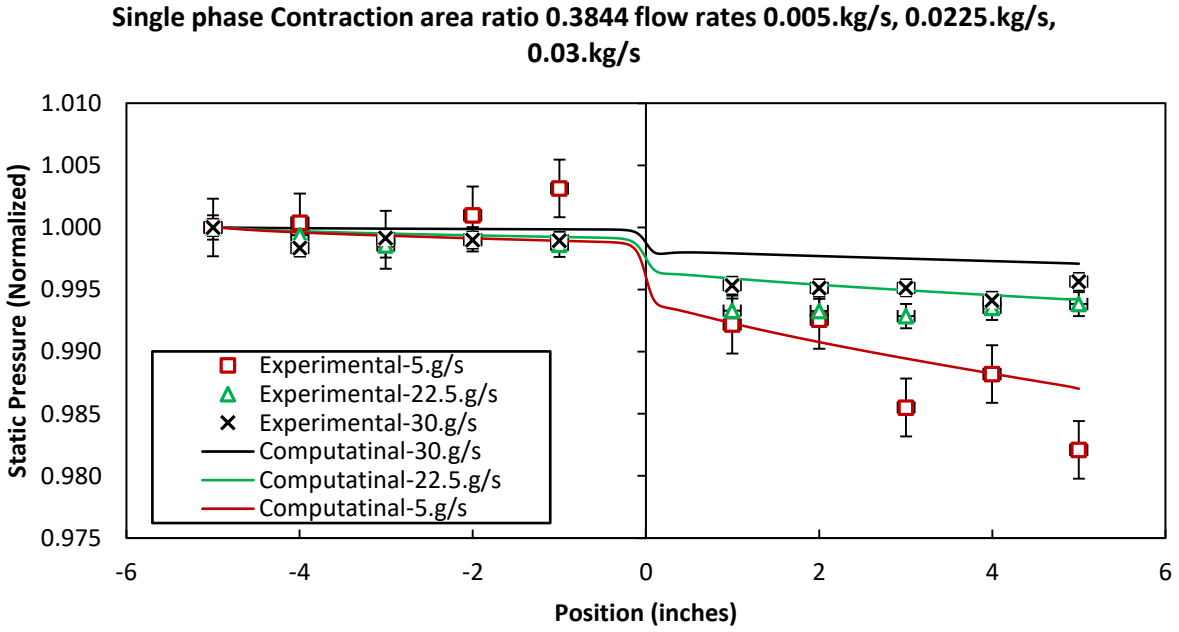

Figure 6.27. Single-phase flow pressure profile performance, compared with experimental data, σ_{con} = 0.3844, $\dot{m}_l$ (kg/s) = 0.03, 0.0225, 0.005

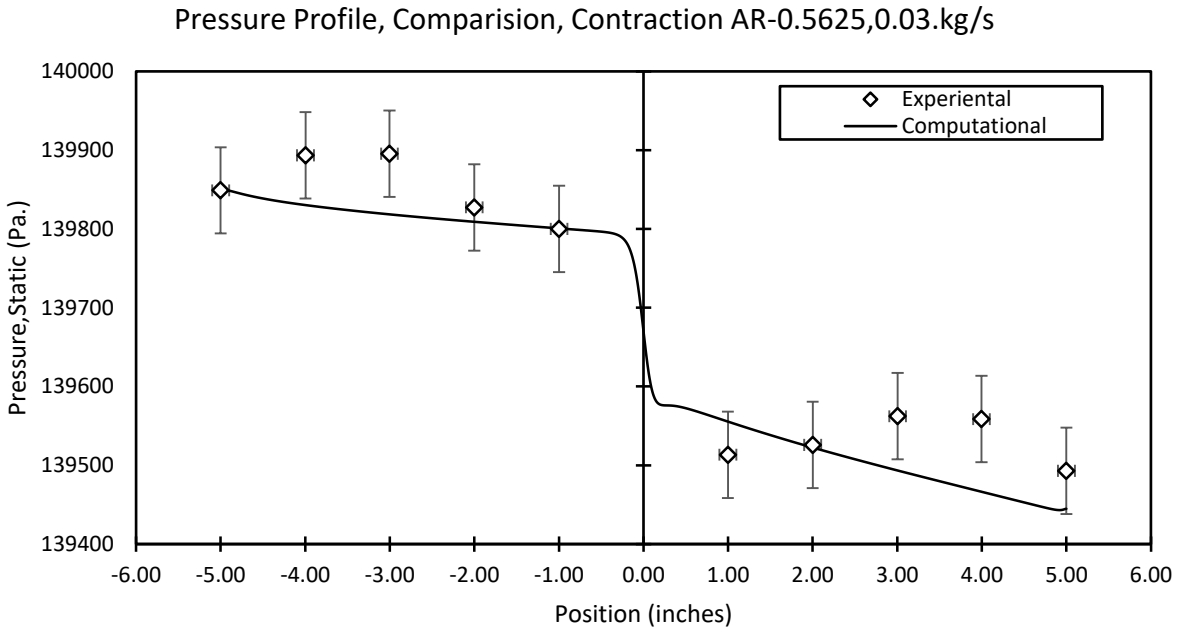

Figure 6.28. Single-phase flow pressure profile structure, compared with experimental data, σ_{con} = 0.5625, $\dot{m}_l$ (kg/s) = 0.03

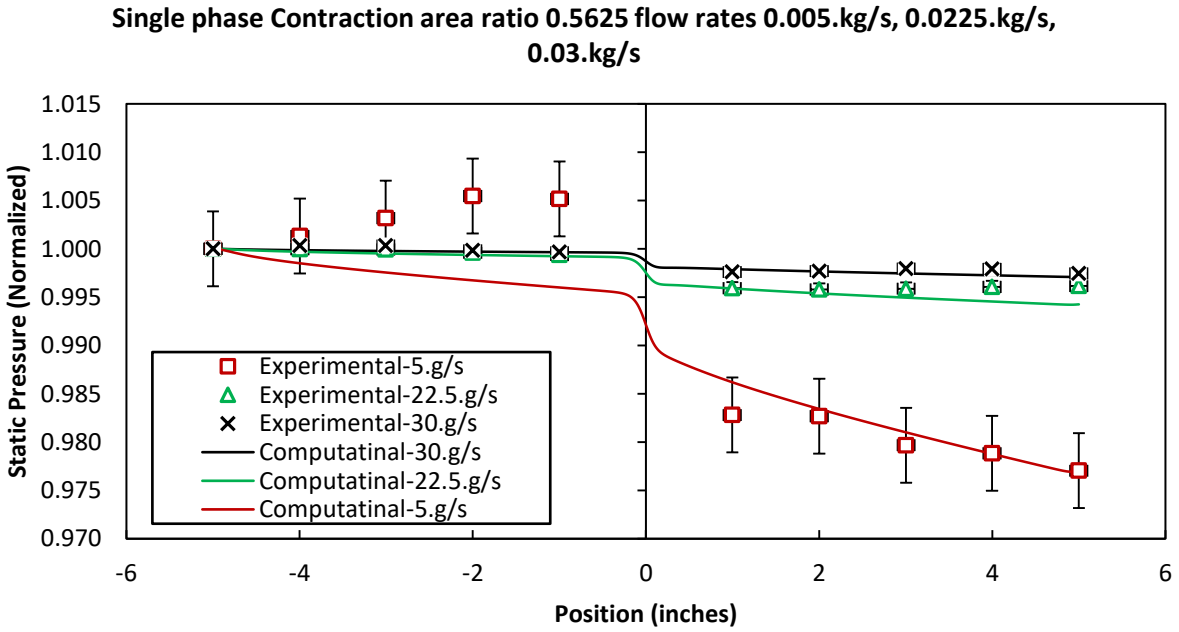

Figure 6.29. Single-phase flow pressure profile performance, compared with experimental data, σ_{con} = 0.5625, $\dot{m}_l$ (kg/s) = 0.03, 0.0225, 0.005

From the graphs, we can observe that, the slight dwell right after area change that is based on the graph, the points after centerline is maximum for the channel with smaller diameter and minimum for channels with a larger diameter. Also, the test section with lower diameter shows accurate prediction of a mathematical model for considered experimental data, although the Figure 6.26, Figure 6.27, show discrepancy in data points of experimental and computational analysis.

The following Figure 6.30 show the comparison of pressure profile occurrence in all test channels by using single flow rate. In this graph, the pressure profile curve on downstream flow is different for the different section and as the statement is true for upstream flow, although the curves are normalized.

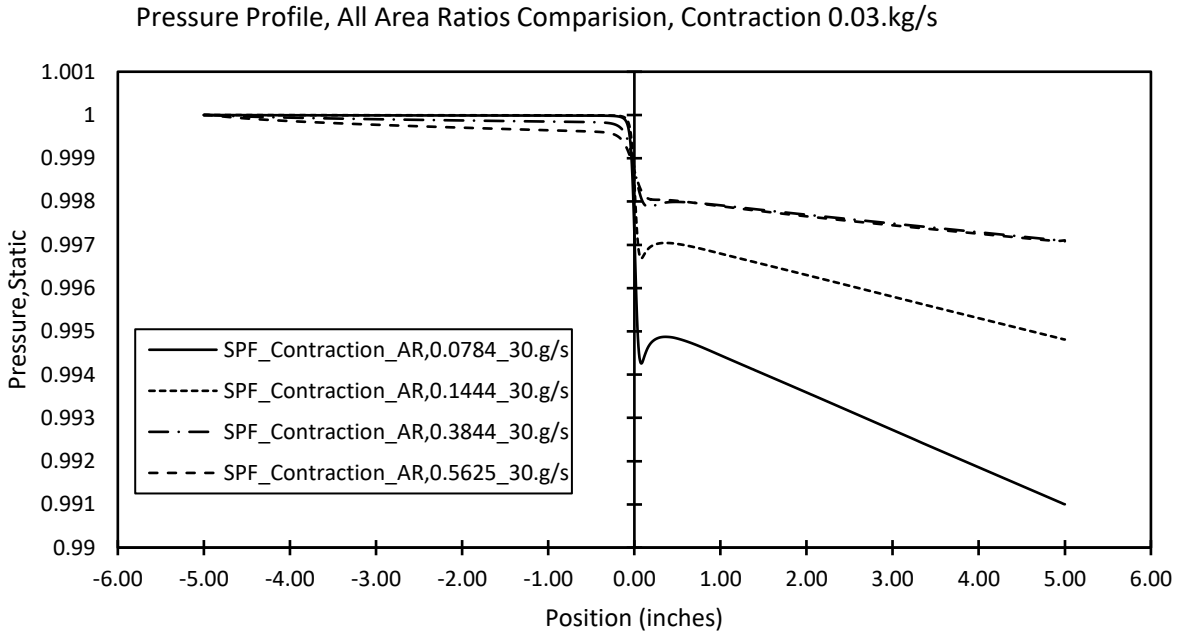

Figure 6.30. Single-phase flow pressure profile performance, comparison, σ_{con} = 0.0784, 0.1444, 0.3844, 0.5625, $\dot{m}_l$ (kg/s) = 0.03.

The test section with $\sigma = 0.0784$ show larger dwell along with the downstream curve with maximum slop value. Followed by test section $\sigma = 0.1444, 0.3844, and\ 0.5625$. The pressure profile difference for upstream flow and downstream flow along center line is lowest for $\sigma = 0.5625$, and the same difference is largest for $\sigma = 0.0784$. With further detailed observation one can speculate that, the upstream flow points show slight slanted slop for test section with $\sigma = 0.5625$, while the test section with $\sigma = 0.0784, and\ others$ show straight horizontal line.

Following Figure 6.31, Figure 6.32, and Figure 6.33 show single-phase contraction pressure drop comparison with current experimental study along with a comparison with previous researcher's co-relations. The test section with $\sigma = 0.0784, 0.3844, and\ 0.5625$ are shown below. Geiger, Yoda co-relations are developed and compared with current studies. For the comparison the, Reynolds number are calculated with traditional algebraic formula with liquid velocity.

The Figure 6.31 shows less than 5% margin error for all flow rates for test section with $\sigma = 0.0784$, which is smallest diameter used for single-phase flow analysis. Along with it, the graph also shows agreeable results with respect to Yoda's co-relation predicted results. Geiger's co-relation, although, do not resembles with neither the experimental nor the computational results. Moreover, the above statement holds true for all test sections. In addition, the Figure 6.32, which represents the results for test section with $\sigma = 0.1444$ does show similar behavior of datasets as of 0.0784 test section.

In the Figure 6.33, the graph shows results for test section with $\sigma = 0.3844$ which shows the excellent establishment for all flow rates between computational and experimental datasets but, does not show agreement between previous researcher's co-relations.

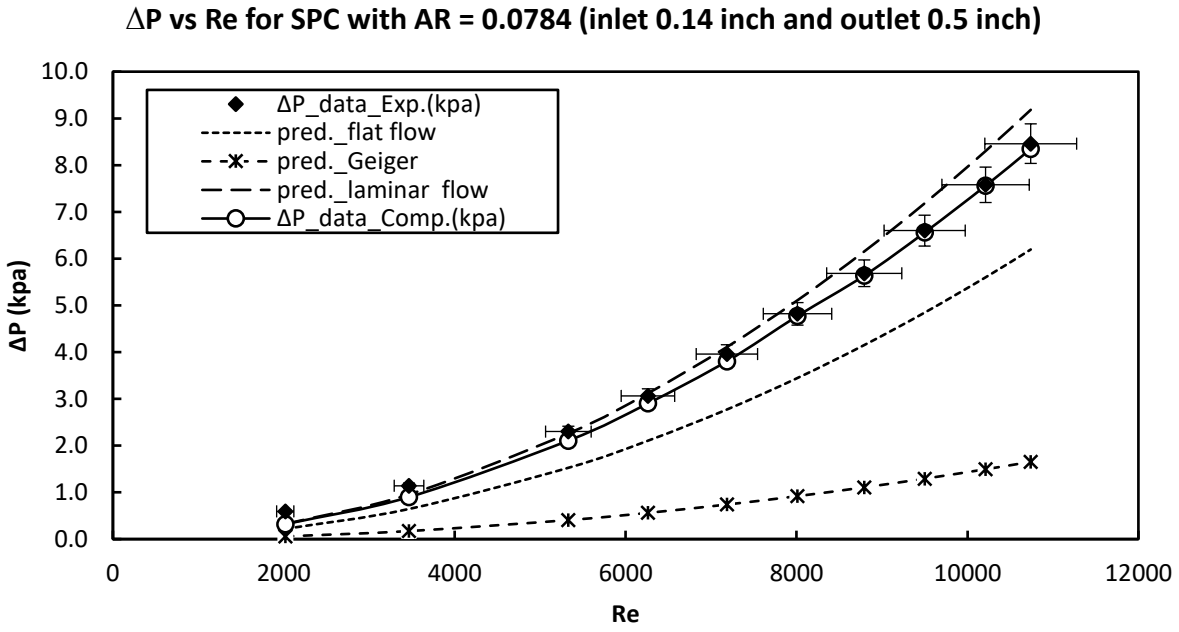

Figure 6.31. Single-phase flow pressure drop performance, compared with experimental data and other co-relations, σ_{exp} = 0.0784, $\dot{m}_l$ (kg/s) = 0.005 - 0.03

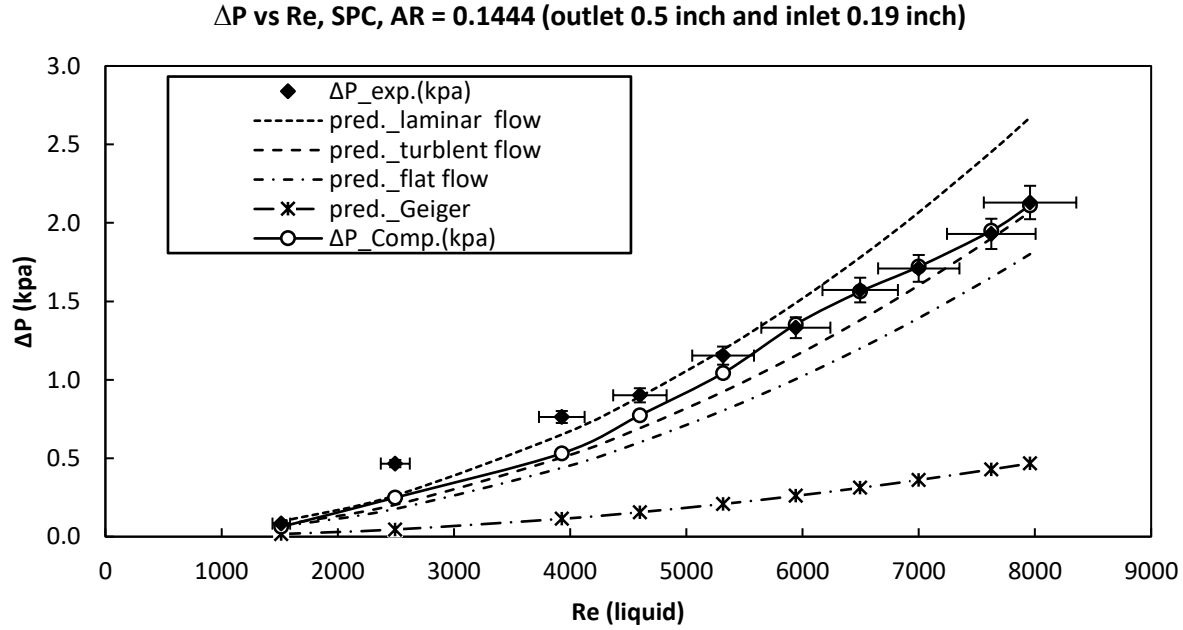

Figure 6.32. Single-phase flow pressure drop performance, compared with experimental data and other co-relations, σ_{exp} = 0.1444, $\dot{m}_l$ (kg/s) = 0.005 - 0.03

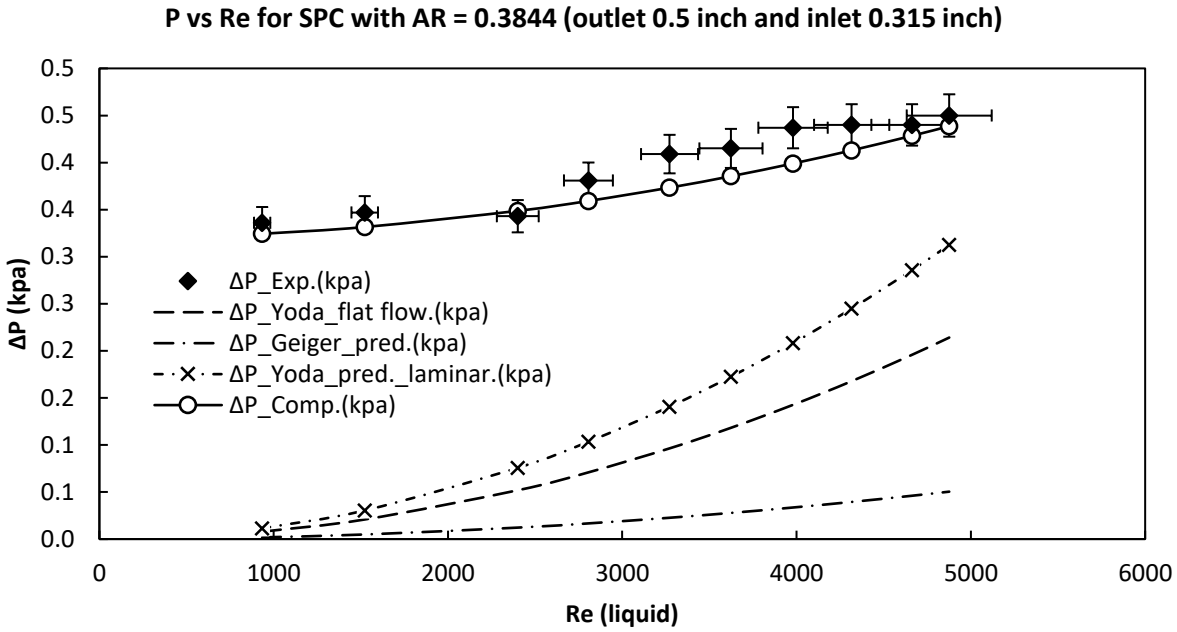

Figure 6.33. Single-phase flow pressure drop performance, compared with experimental data and other co-relations, σ_{exp} = 0.3844, $\dot{m}_l$ (kg/s) = 0.005 - 0.03

6.2.4 Two-Phase Flow

Two-phase flow computationally solved with Eulerian-Eulerian multiphase model and Reynolds Stress Turbulence Model (RSM). Identical 2-Dimensional geometries were used. RSM model is coupled with the multiphase Eulerian-Eulerian gas-liquid model because of the assurance of convergence residuals of scalar quantities in single-phase flows. This shows similar pressure profiles as single phase flows with same patterns and visualizations for both contraction and expansion channels. In this section the pressure profiles rather than showing individualistically shown in groups of 10 flow rates. Each test section analyzed with five gas flow rates, each containing ten liquid flow rates, which accounts 50 flow rate case studies for each section. Like this 3 test sections analyzed, which generates almost 150 case studies. Furthermore, these test sections were used for both contraction and expansion phenomenon. Hence nearly 300 case studies

with 300 datasets were generated. After analyzing results, the results with the excellent agreement as computational and experimental were decided to explain. A constant superficial mass flow rate of nitrogen while the variable superficial mass flow rate of water is used throughout the analysis.

6.2.4.1 Expansion Pressure Profile and Pressure Drop

The Figure 6.34, Figure 6.35, and Figure 6.36 illustrate the computational pressure profiles of test section $\sigma = 0.1444, 0.3844, 0.5625$ with the maximum gas flow rate which is 0.028 kg/s and all 10 liquid flow rates. The pressure profile structure for each test section is different compared to other. The test section with area ratio = 0.1444 show lowest rise of pressure points after flow stabilization in downstram channel. While pressure profiles for test section with area ratio = 0.3844 show better rise in downstream pressure of channel, followed by highest rise in downstream pressure profiles for test section with area ratio = 0.5625. In all the above mentioned graphs, the pressure profile for 0.01kg/s flow rate is lowest while the pressure profile for 0.03kg/s is highest. The all other presure profiles are in between these two flow rates. Moreover, the pressure profiles show close accordance between any two higher flow rates which are after 0.0225kg/s. while for lower flow rates the distance between two pressure profiles is high. It can be further stated that the pressure drop increases with respect to increase in mass flow rate of water, and hence with an increase in void fractions of water, along with increasing a mass flow rate of nitrogen. The pressure profiles and trend-lines show higher values compared to single phase flows for some cases. This trend is observed perticularlly as the flow rate for gas is increased.

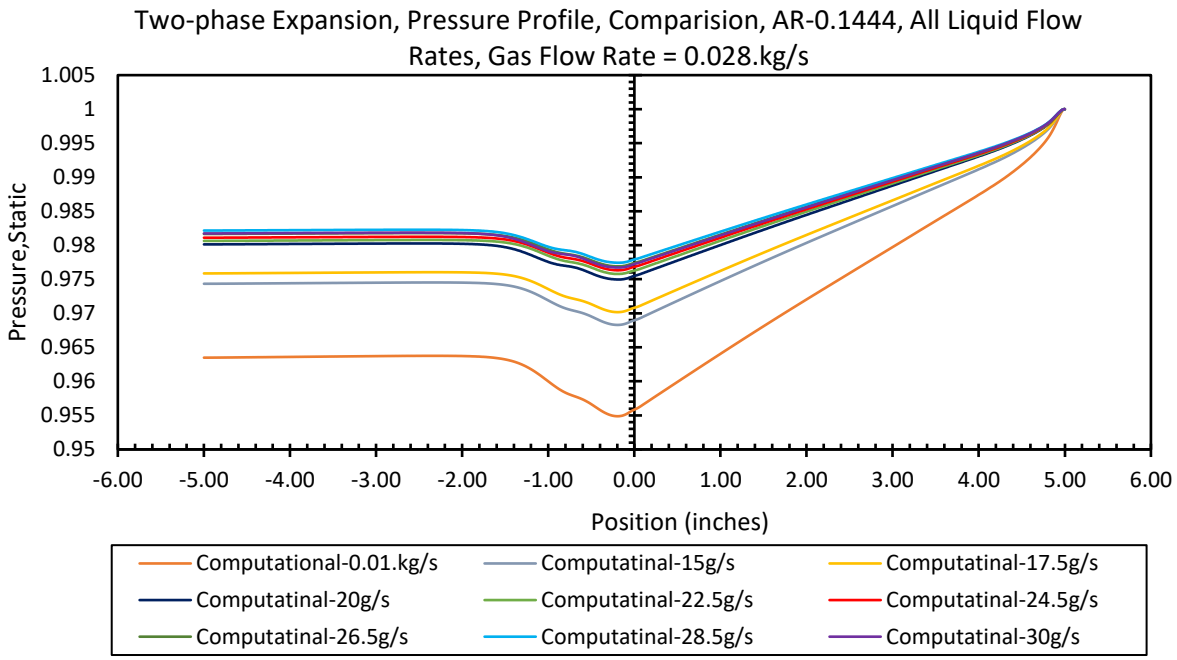

Figure 6.34. Two-phase flow pressure profile performance, σ_{exp} = 0.1444, $\dot{m}_l$ (kg/s) = 0.005-0.03, $\dot{m}_g$ (kg/s) = 0.028.

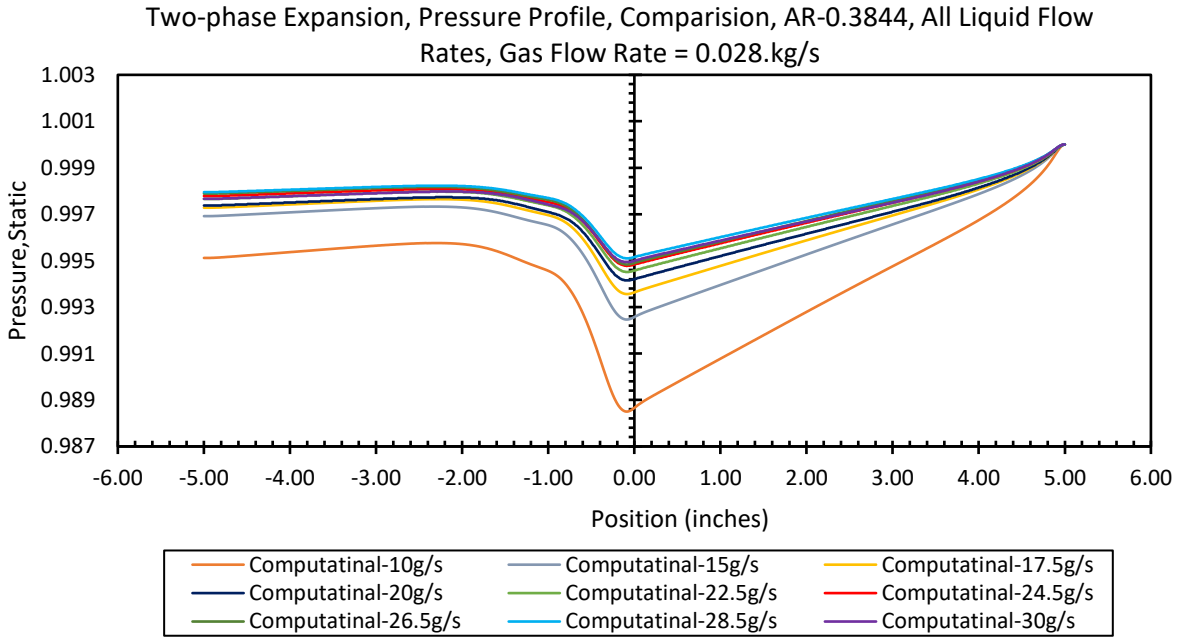

Figure 6.35. Two-phase flow pressure profile performance, σ_{exp} = 0.3844, $\dot{m}_l$ (kg/s) = 0.005-0.03, $\dot{m}_g$ (kg/s) = 0.028.

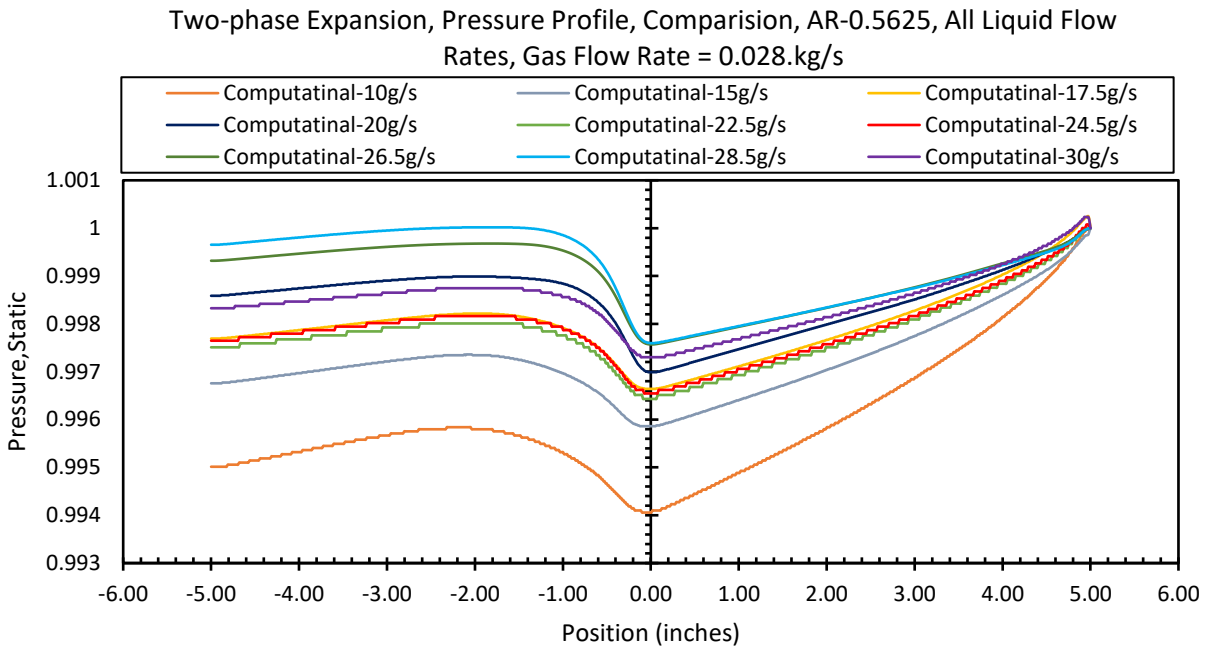

Figure 6.36. Two-phase flow pressure profile performance, σ_{exp} = 0.5625, $\dot{m}_l$ (kg/s) = 0.005-0.03, $\dot{m}_g$ (kg/s) = 0.028.

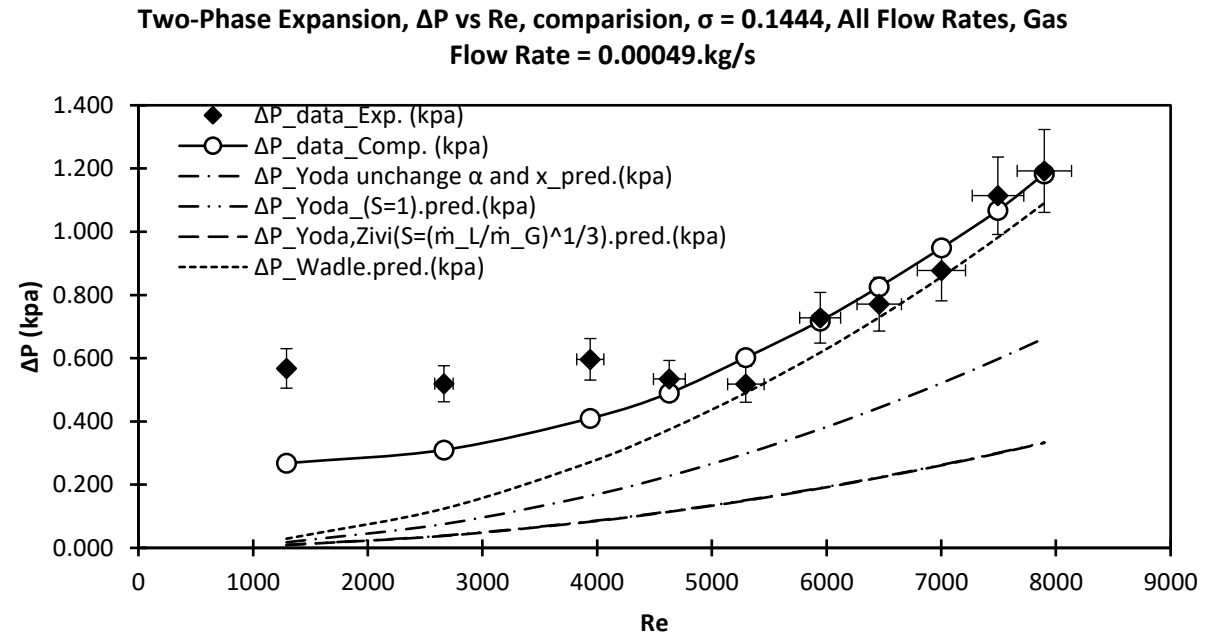

Figure 6.37. Two-phase flow pressure drop performance, compared with experimental data and other co-relations, σ_{exp} = 0.1444, $\dot{m}_l$ (kg/s) = 0.005 - 0.03, $\dot{m}_g$ (kg/s) = 0.00049

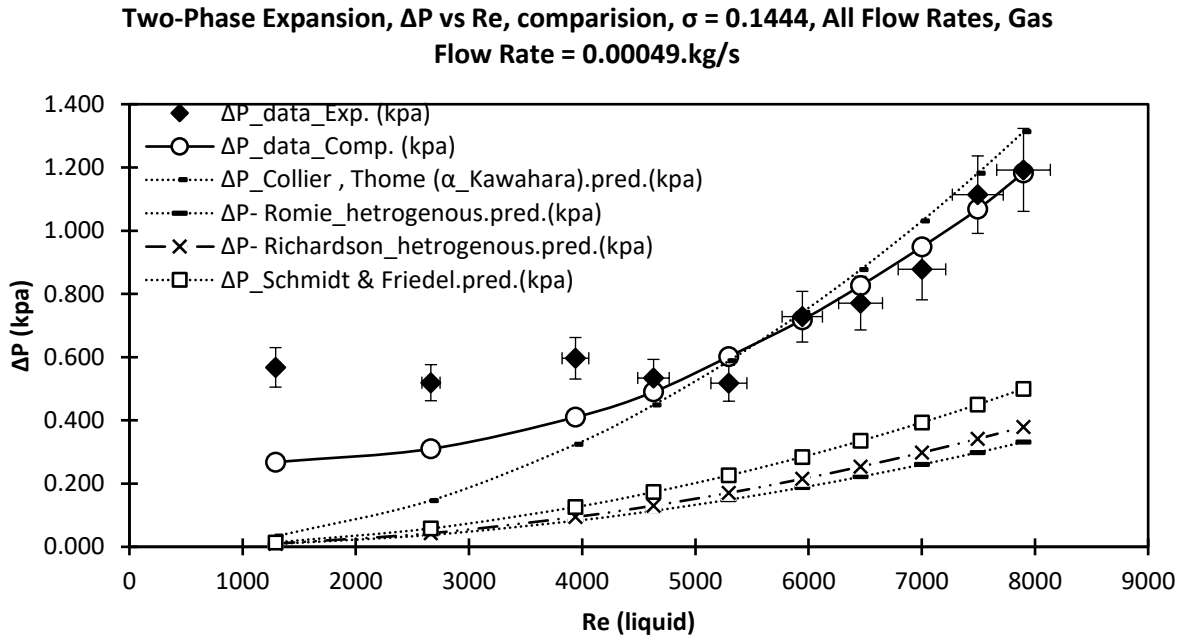

Figure 6.38. Two-phase flow pressure drop performance, compared with experimental data and other co-relations, σ_{exp} = 0.1444, $\dot{m}_l$ (kg/s) = 0.005 - 0.03, $\dot{m}_g$ (kg/s) = 0.00049

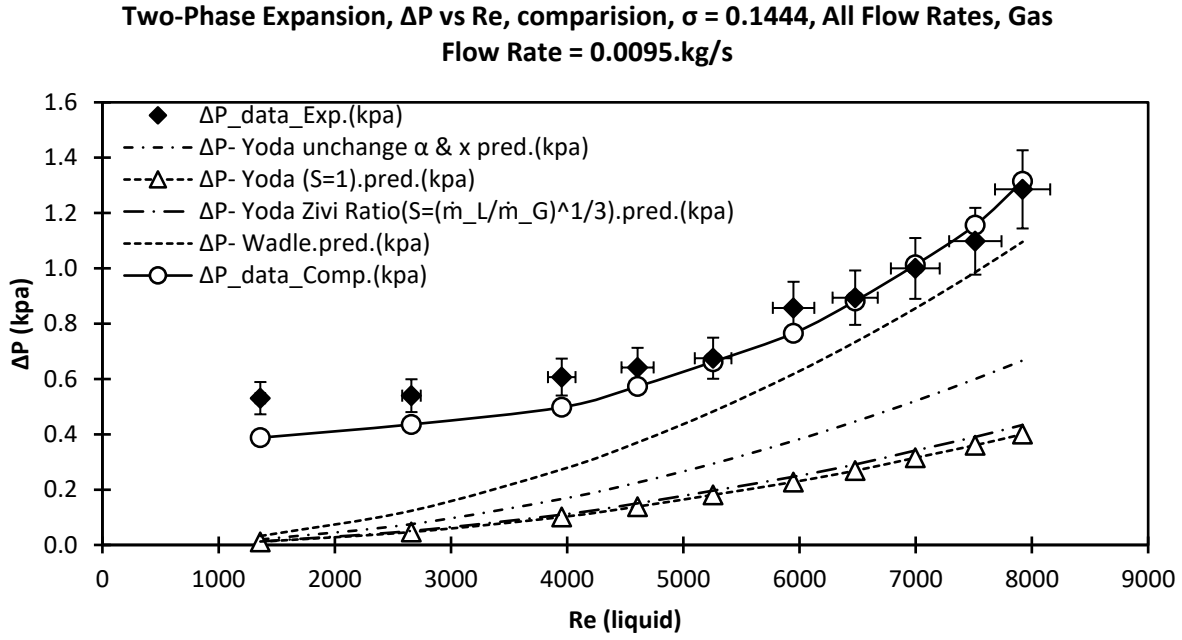

Figure 6.39. Two-phase flow pressure drop performance, compared with experimental data and other co-relations, σ_{exp} = 0.1444, $\dot{m}_l$ (kg/s) = 0.005 - 0.03, $\dot{m}_g$ (kg/s) = 0.0095

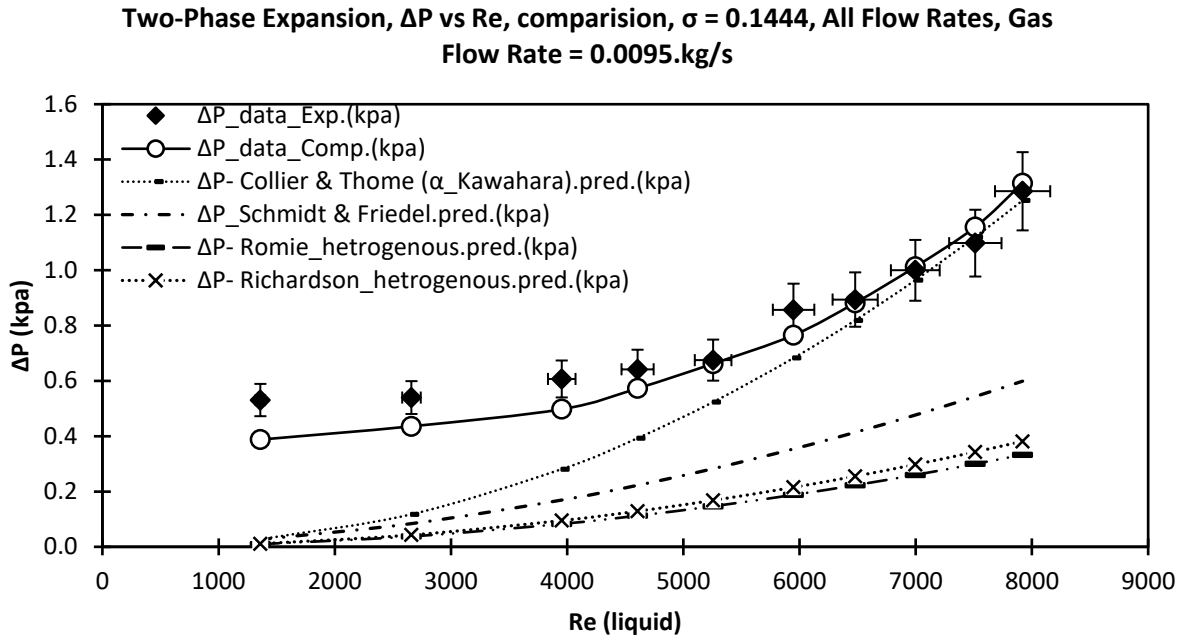

Figure 6.40. Two-phase flow pressure drop performance, compared with experimental data and other co-relations, σ_{exp} = 0.1444, $\dot{m}_l$ (kg/s) = 0.005 - 0.03, $\dot{m}_g$ (kg/s) = 0.0095

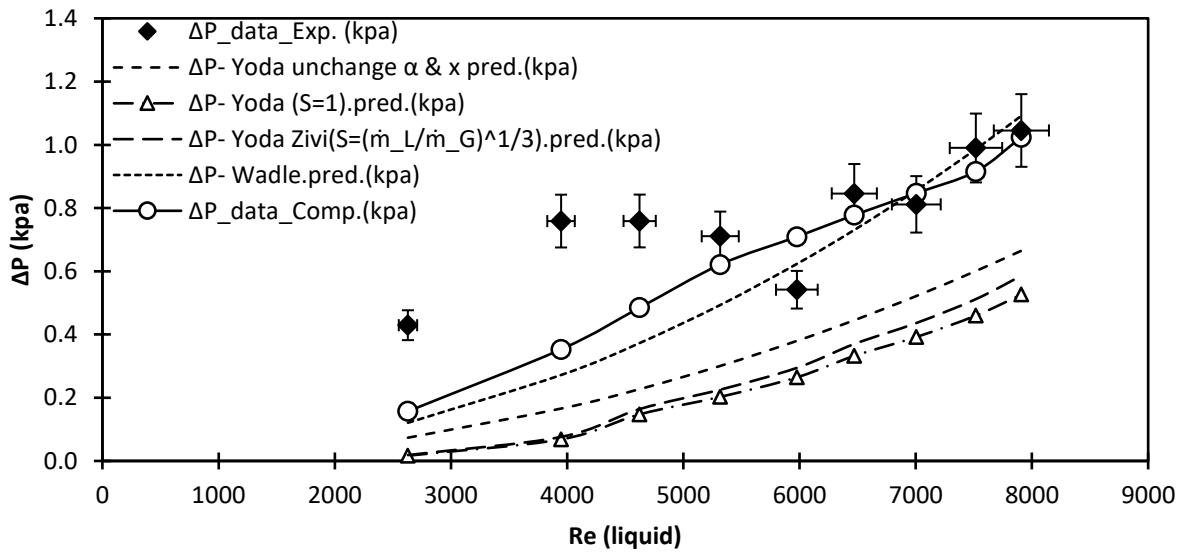

Figure 6.41. Two-phase flow pressure drop performance, compared with experimental data and other co-relations, σ_{exp} = 0.1444, $\dot{m}_l$ (kg/s) = 0.005 - 0.03, $\dot{m}_g$ (kg/s) = 0.028

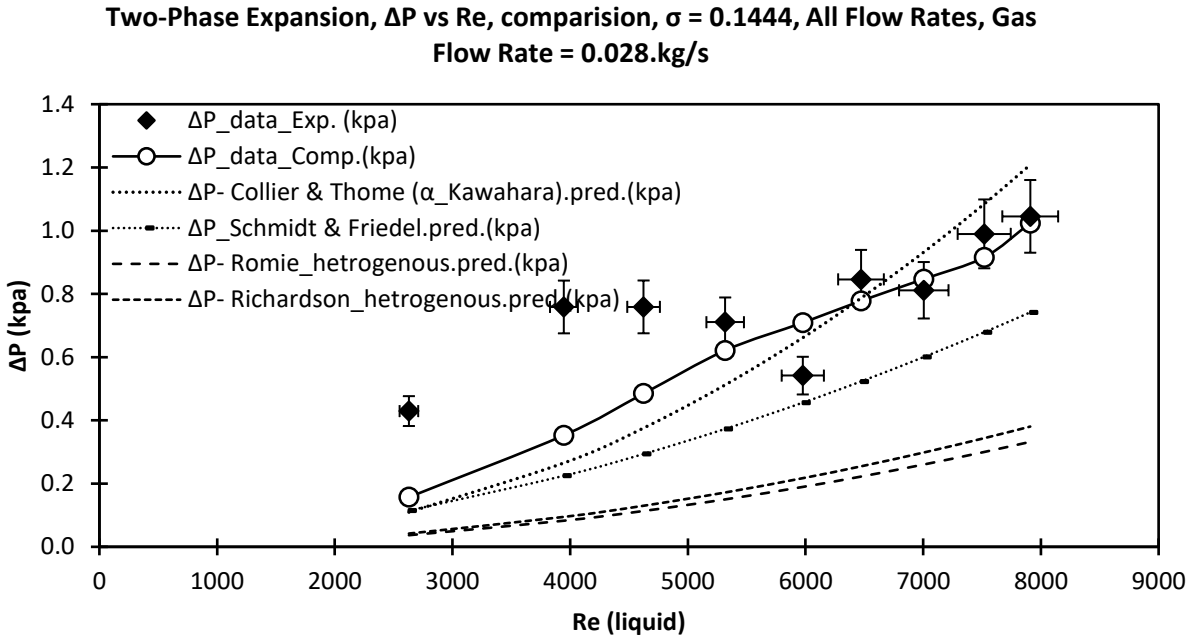

Figure 6.42. Two-phase flow pressure drop performance, compared with experimental data and other co-relations, σ_{exp} = 0.1444, $\dot{m}_l$ (kg/s) = 0.005 - 0.03, $\dot{m}_g$ (kg/s) = 0.028

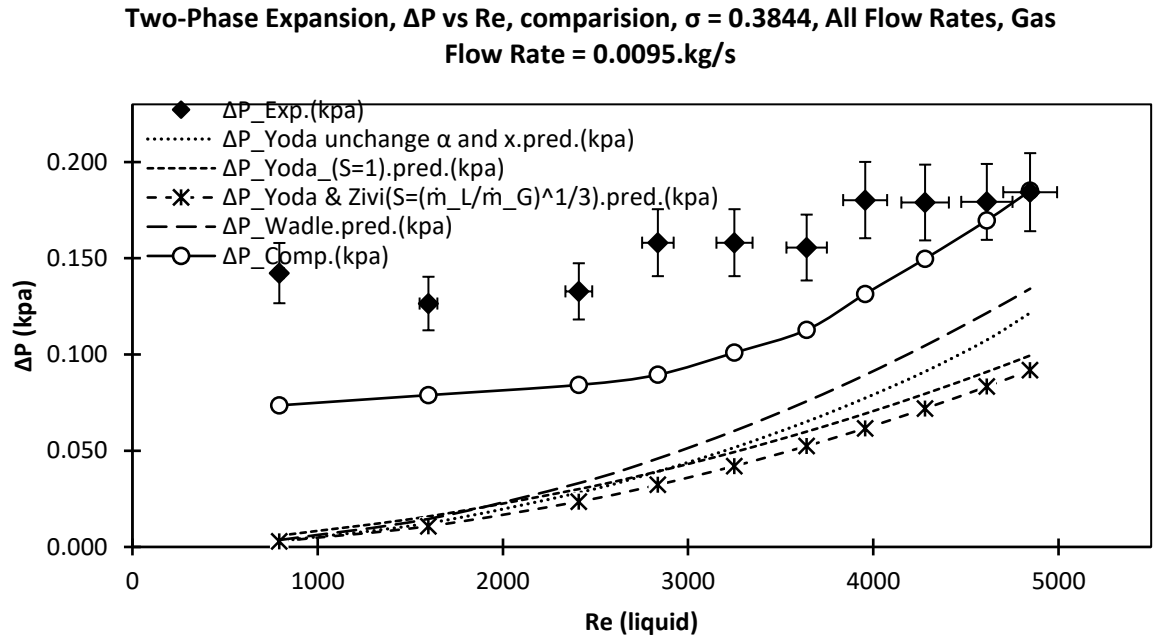

Figure 6.43. Two-phase flow pressure drop performance, compared with experimental data and other co-relations, σ_{exp} = 0.3844, $\dot{m}_l$ (kg/s) = 0.005 - 0.03, $\dot{m}_g$ (kg/s) = 0.0095

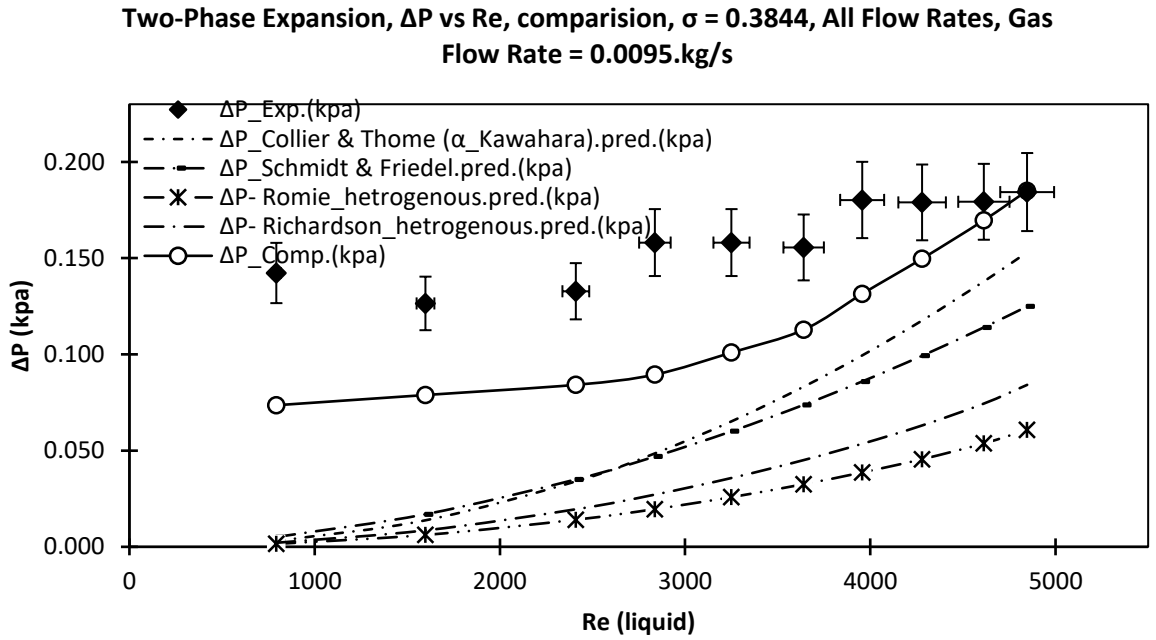

Figure 6.44. Two-phase flow pressure drop performance, compared with experimental data and other co-relations, σ_{exp} = 0.3844, $\dot{m}_l$ (kg/s) = 0.005 - 0.03, $\dot{m}_g$ (kg/s) = 0.0095

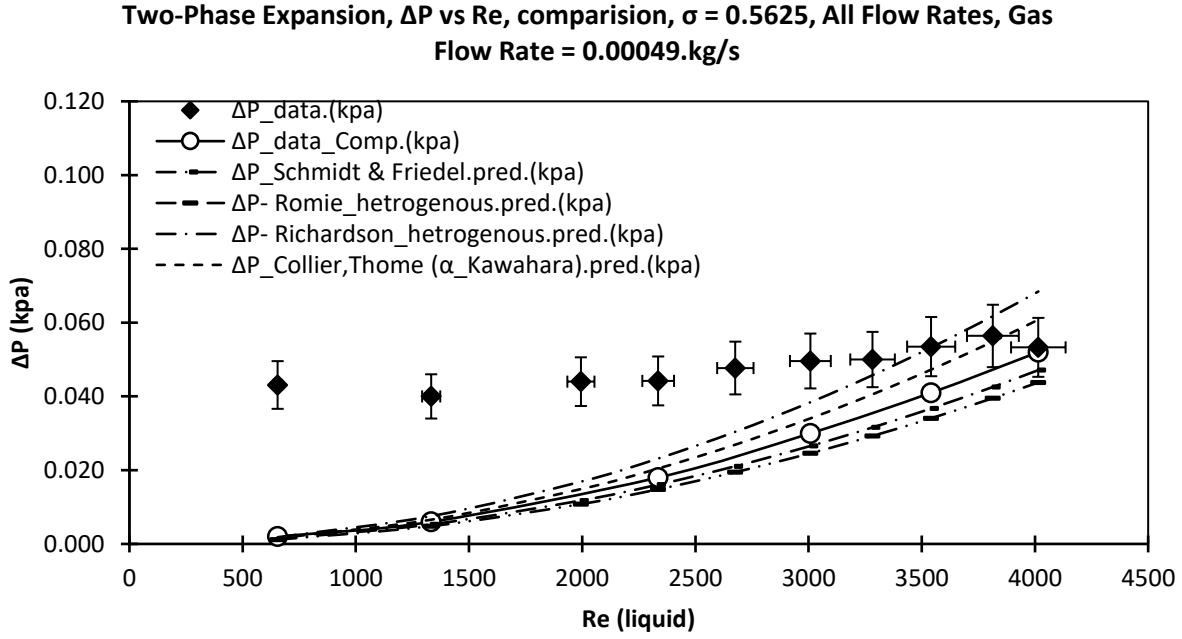

Figure 6.45. Two-phase flow pressure drop performance, compared with experimental data and other co-relations, σ_{exp} = 0.5625, $\dot{m}_l$ (kg/s) = 0.005 - 0.03, $\dot{m}_g$ (kg/s) = 0.00049

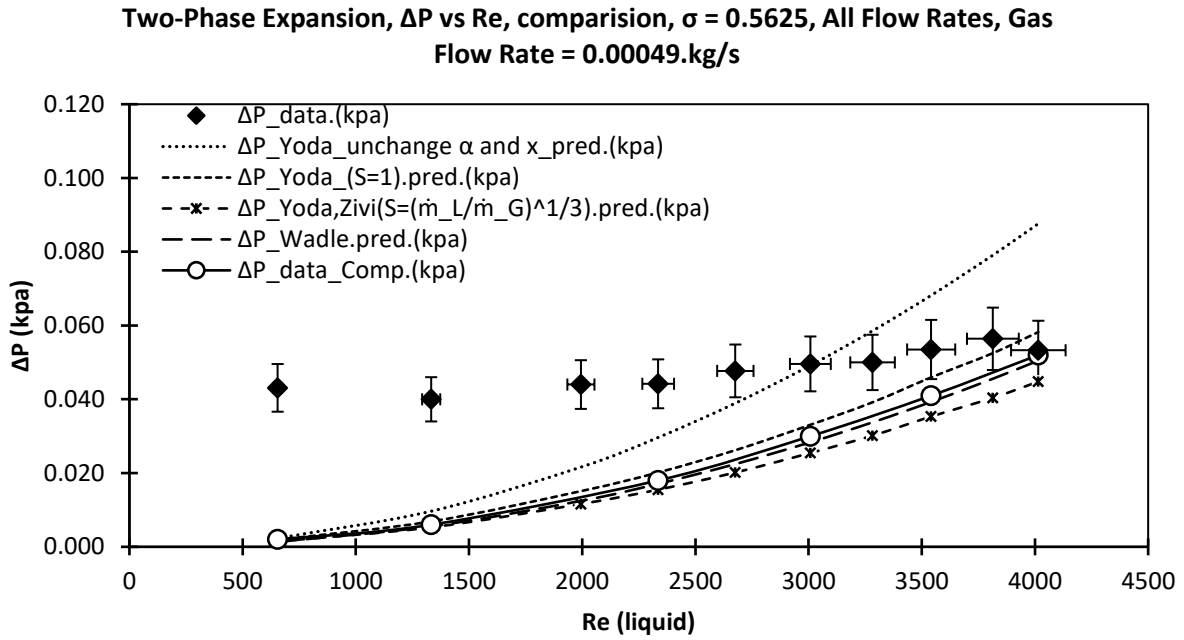

Figure 6.46. Two-phase flow pressure drop performance, compared with experimental data and other co-relations, σ_{exp} = 0.5625, $\dot{m}_l$ (kg/s) = 0.005 - 0.03, $\dot{m}_g$ (kg/s) = 0.00049

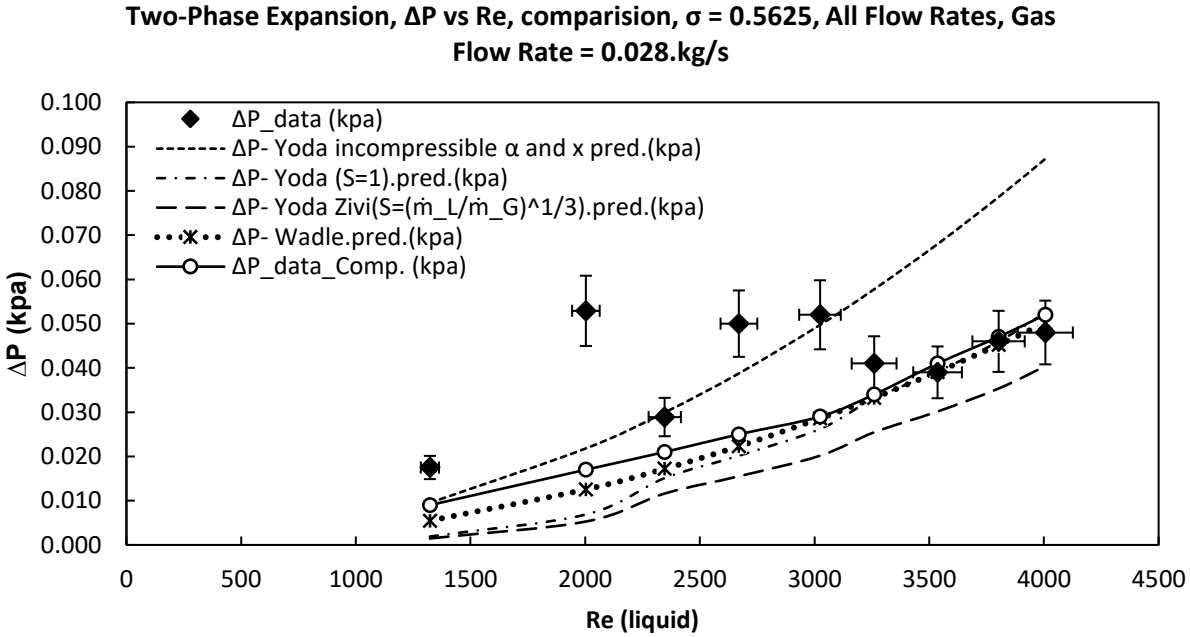

Figure 6.47. Two-phase flow pressure drop performance, compared with experimental data and other co-relations, σ_{exp} = 0.5625, $\dot{m}_l$ (kg/s) = 0.005 - 0.03, $\dot{m}_g$ (kg/s) = 0.0028

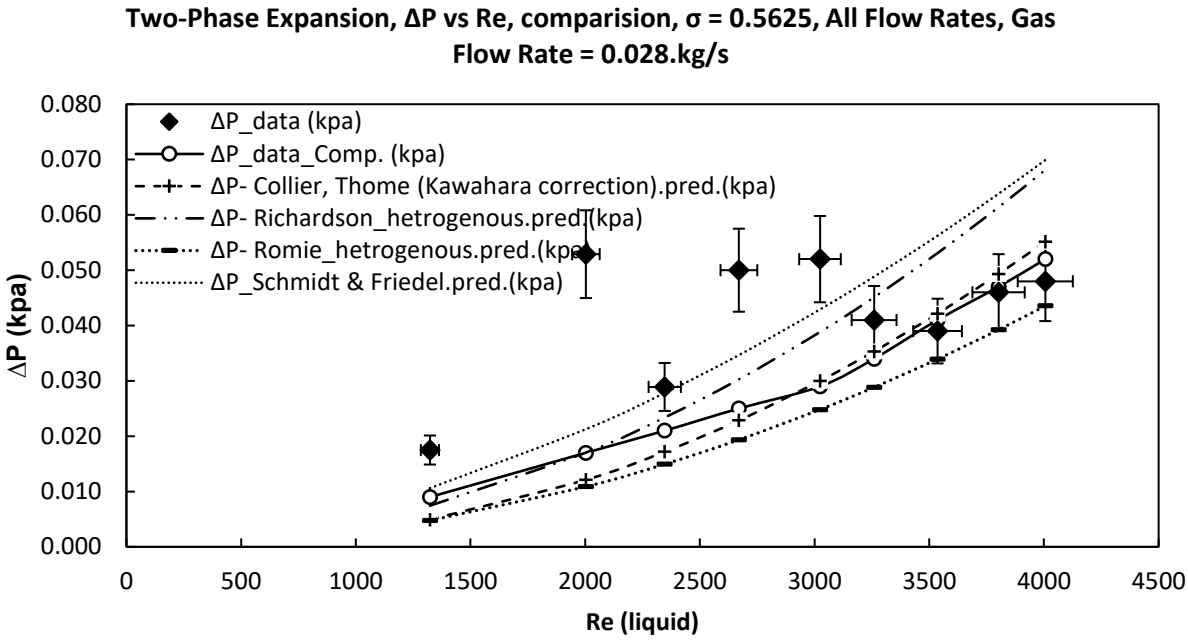

Figure 6.48. Two-phase flow pressure drop performance, compared with experimental data and other co-relations, σ_{exp} = 0.5625, $\dot{m}_l$ (kg/s) = 0.005 - 0.03, $\dot{m}_g$ (kg/s) = 0.028

The pressure drop, which is shown from Figure 6.37 to Figure 6.48 is calculated with the same procedure as the pressure drop calculations for single-phase flow that is trendlines along downstream flow and upstream flow after data points interpolation. For two-phase flow expansion phenomenon researchers, Collier-Thome [22], Wadle [9], Yoda [8], and Schmidt-Freidel [13], and their co-relations based on their experimental calculations were compared.

For lower diameter test sections, the pressure drop value is higher, while for test section with a higher diameter the pressure drop value is lower. Thus for the lower diameter test section, such as $\sigma = 0.1444$, the pressure drop for higher flow rates show resembling values with respect to Collier & Thome [22], Yoda [8], and Wadle [9]. As the diameter increased the pressure drop values of current studies, which are experimental and computational, are diffcult to resemble with

previous researcher's co-relations (except for the highest flow rate). Also, the discrepancies, just like two-phase flow are more for lower flow rates.

6.2.4.2 Contraction Pressure Profile and Pressure Drop

The fluid is considered to be incompressible, although the presence of compressibility effects was account for particular experimental data. The following Figure 6.49, Figure 6.50, Figure 6.51 illustrate the comparison of two-phase flow computationally generated pressure profiles in contraction phenomenon using test section of $\sigma = 0.1444, 0.3844, 0.5625$ with gas flow rate 0.028 kg/s. Also, the pressure profile measured based on the 5D and 10D pressure tap shows good agreement of values concerning experimental values with a percentage error of 3% concerning computational values. The pressure profiles generated from the analysis of area ratio = 0.3844 shows the elevation of data point values of downstream pressure, after sudden contraction of the area. Inlet pressure value is shown more compared to outlet pressure value. all pressure profiles are normalized and plotted. Thus with the peculiar observation this shows the pressure profile increases the value of pressure drop, also this statement holds true for larger diameter of channels while for smaller diameter, the pressure profile shows same behavior. This analysis is performed by calculating void fraction parameters of nitrogen and water, hence above discussion holds true for 0.85 to 0.9 value of a void fraction of water while, remaining is calculated to be nitrogen, the gaseous phase.

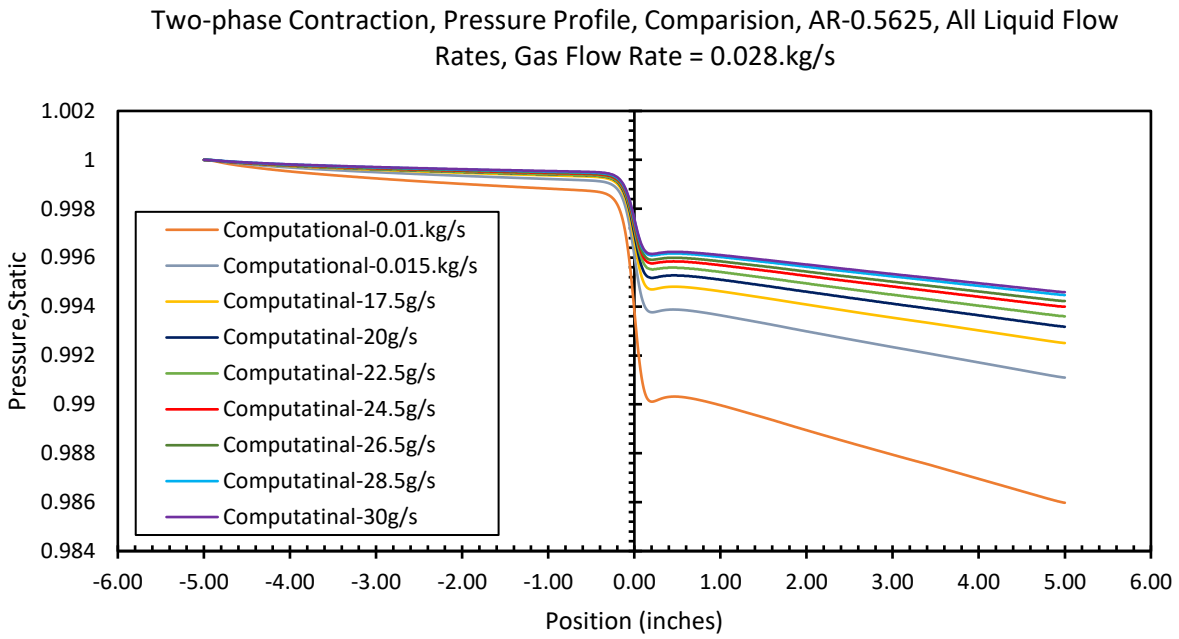

Figure 6.49. Two-phase flow pressure profile performance, σ_{con} = 0.5625, $\dot{m}_l$ (kg/s) = 0.005-0.03, $\dot{m}_g$ (kg/s) = 0.028.

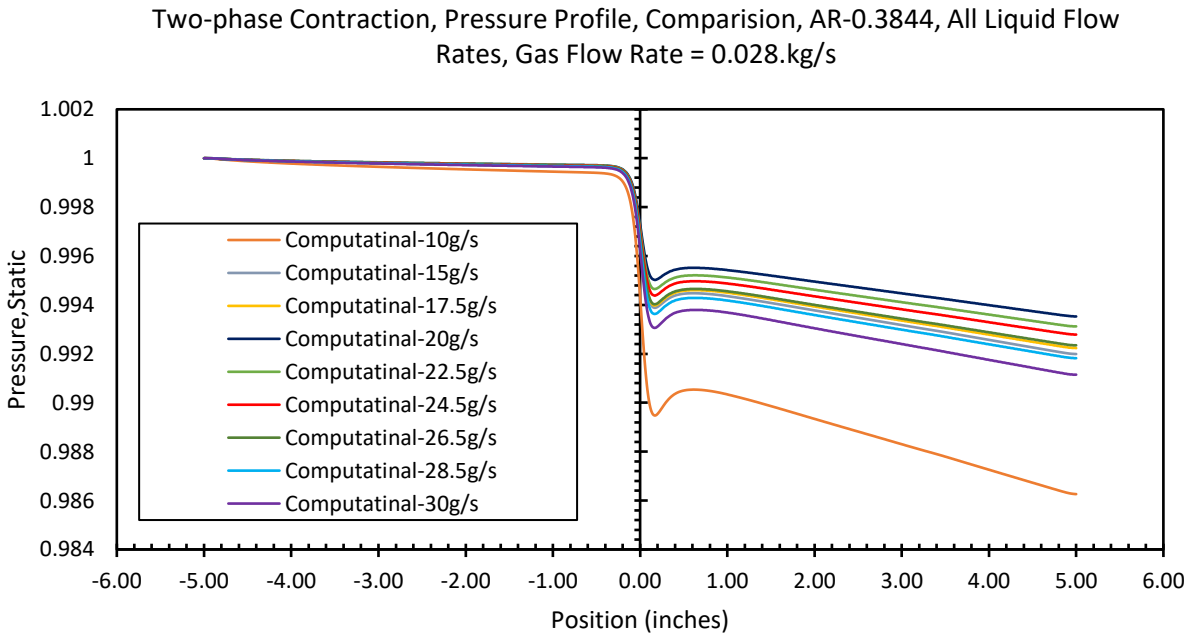

Figure 6.50. Two-phase flow pressure profile performance, σ_{con} = 0.3844, $\dot{m}_l$ (kg/s) = 0.005-0.03, $\dot{m}_g$ (kg/s) = 0.028.

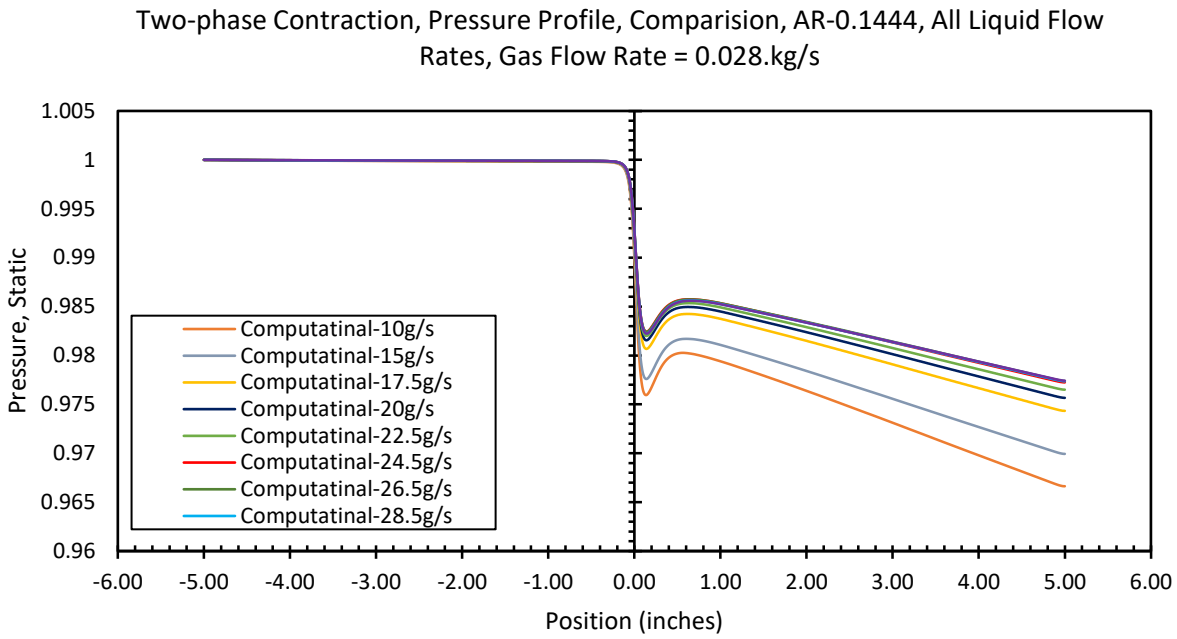

Figure 6.51. Two-phase flow pressure profile performance, σ_{con} = 0.1444, $\dot{m}_l$ (kg/s) = 0.005-0.03, $\dot{m}_g$ (kg/s) = 0.028.

The Reynolds number shows a higher value for more significant flow rates in two-phase flows calculations while for lower flow rates the values are lower, this behavior is similar to single-phase flow calculations. The Reynolds number for test section with $\sigma = 0.1444 \; and \; \dot{m}_g = 0.028 \frac{kg}{s}, and \; \dot{m}_l = 0.005 \frac{kg}{s}$, the value of Reynolds number is 2560, while for single phase flow, the similar test section area ratio with similar water flow rate, the Reynolds number value is 654. This also describe us that for smaller flow rates the two-phase flow in micro-channel does show turbulent or transition to turbulent behavior. Also, the Eulerian model computes the Reynolds number with turbulent phase interactions hence the computed Reynolds number is higher than the experimental data based theoretical calculations, but the percentage error is less than 5\%.

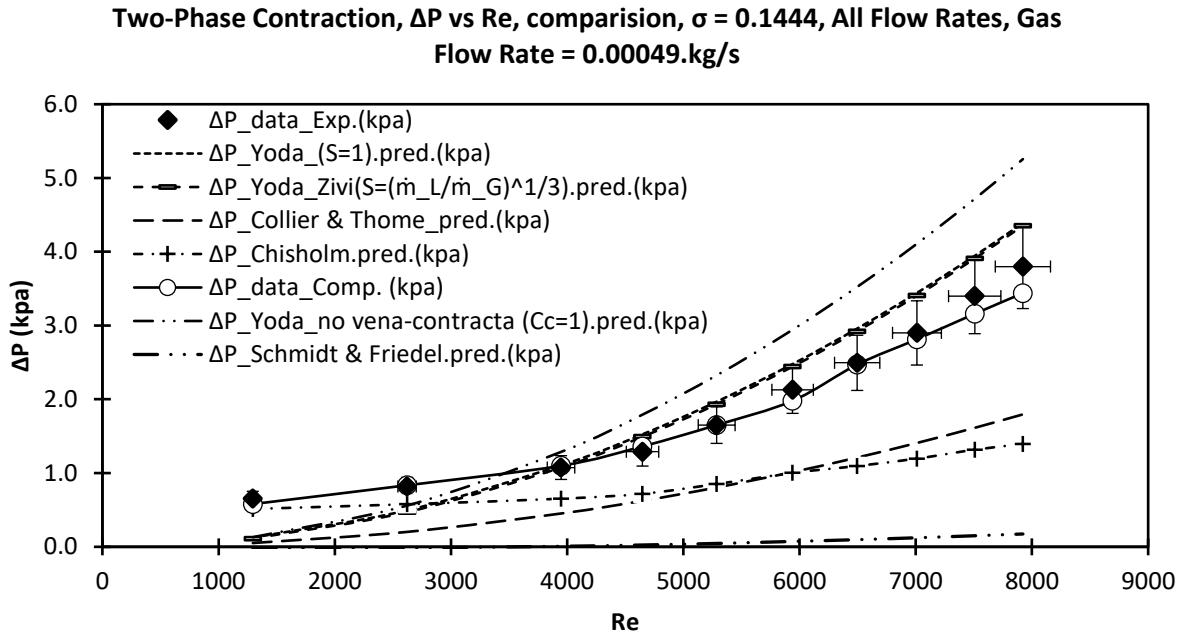

Figure 6.52. Two-phase flow pressure drop performance, compared with experimental data and other co-relations, σ_{con} = 0.1444, $\dot{m}_l$ (kg/s) = 0.005 - 0.03, $\dot{m}_g$ (kg/s) = 0.00049

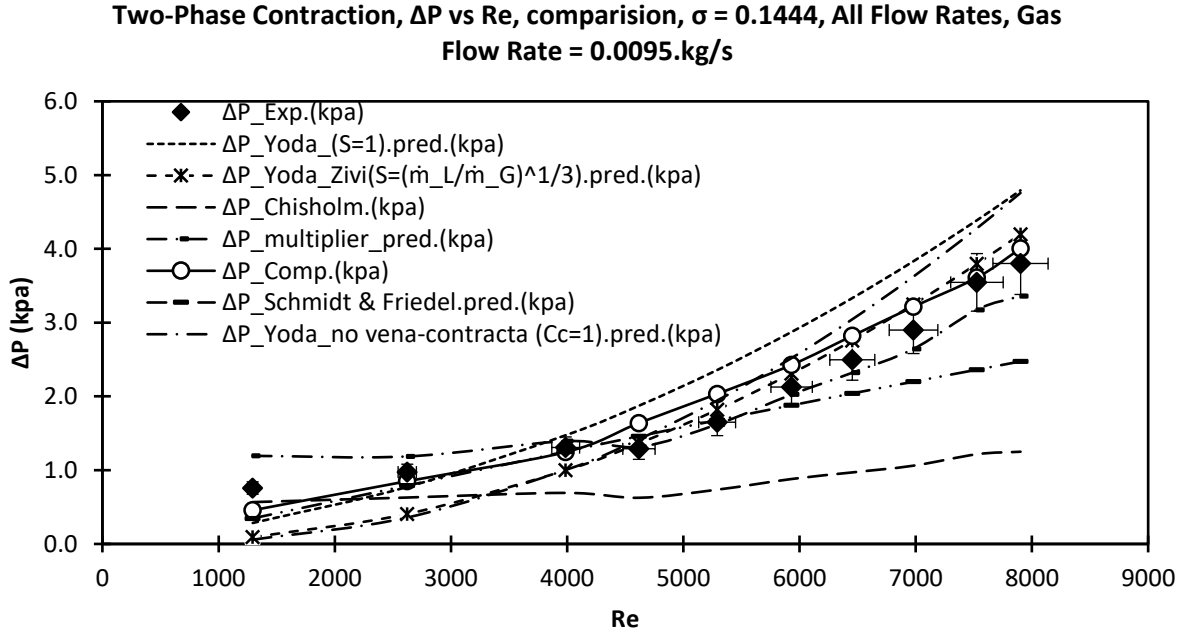

Figure 6.53. Two-phase flow pressure drop performance, compared with experimental data and other co-relations, σ_{con} = 0.1444, $\dot{m}_l$ (kg/s) = 0.005 - 0.03, $\dot{m}_g$ (kg/s) = 0.0095

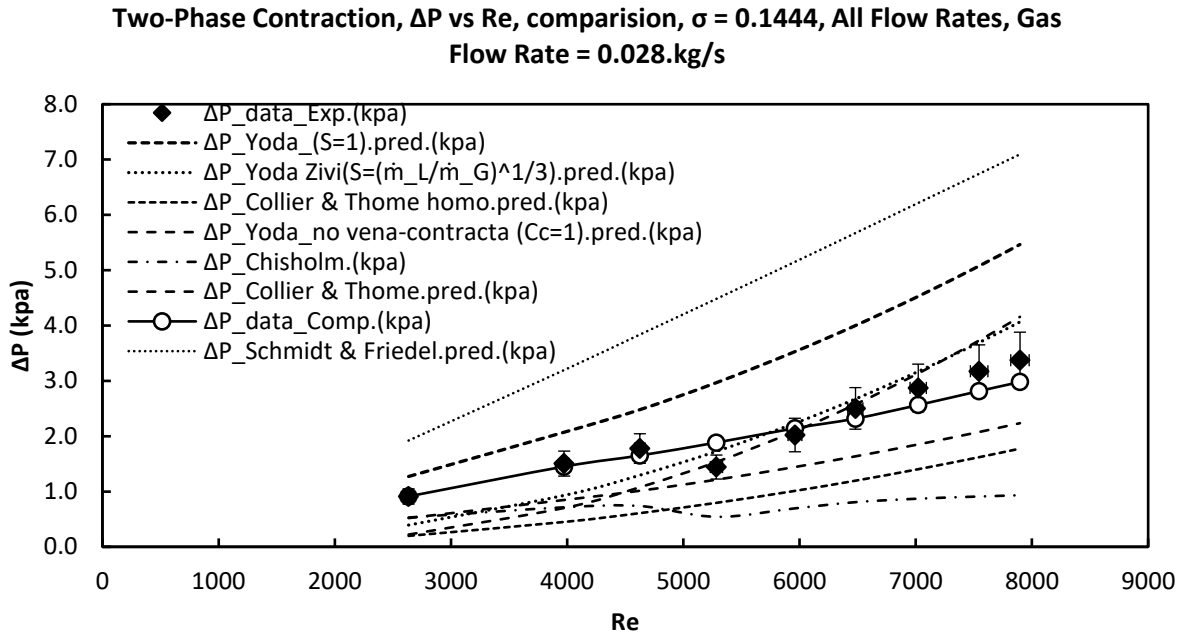

Figure 6.54. Two-phase flow pressure drop performance, compared with experimental data and other co-relations, σ_{con} = 0.1444, $\dot{m}_l$ (kg/s) = 0.005 - 0.03, $\dot{m}_g$ (kg/s) = 0.028

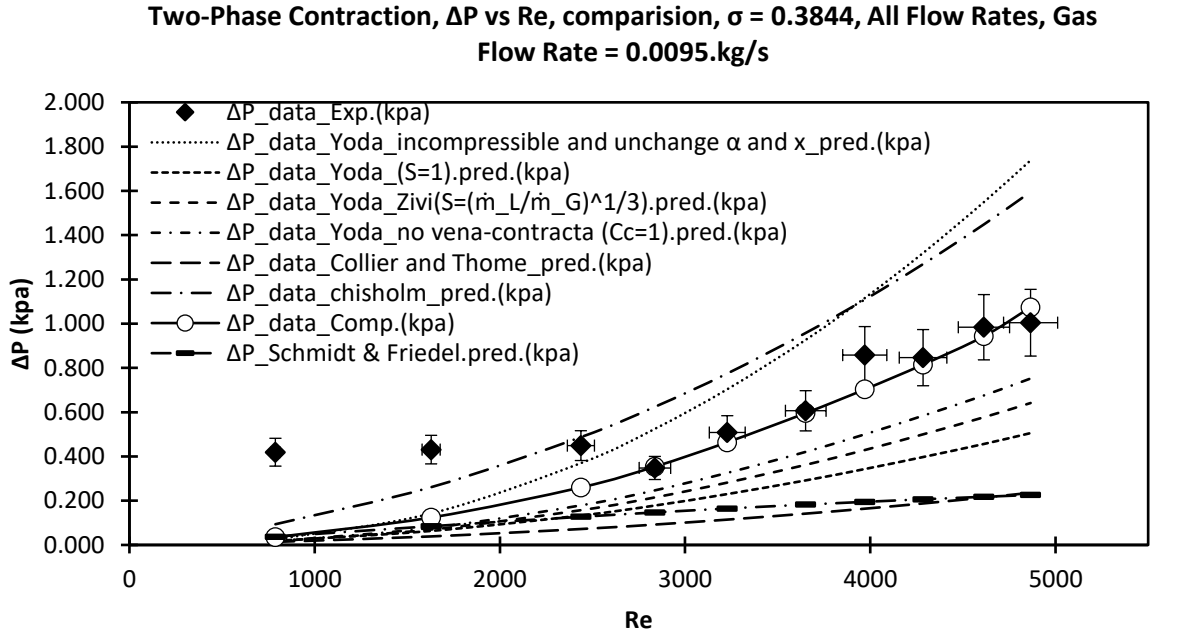

Figure 6.55. Two-phase flow pressure drop performance, compared with experimental data and other co-relations, σ_{con} = 0.3844, $\dot{m}_l$ (kg/s) = 0.005 - 0.03, $\dot{m}_g$ (kg/s) = 0.0095

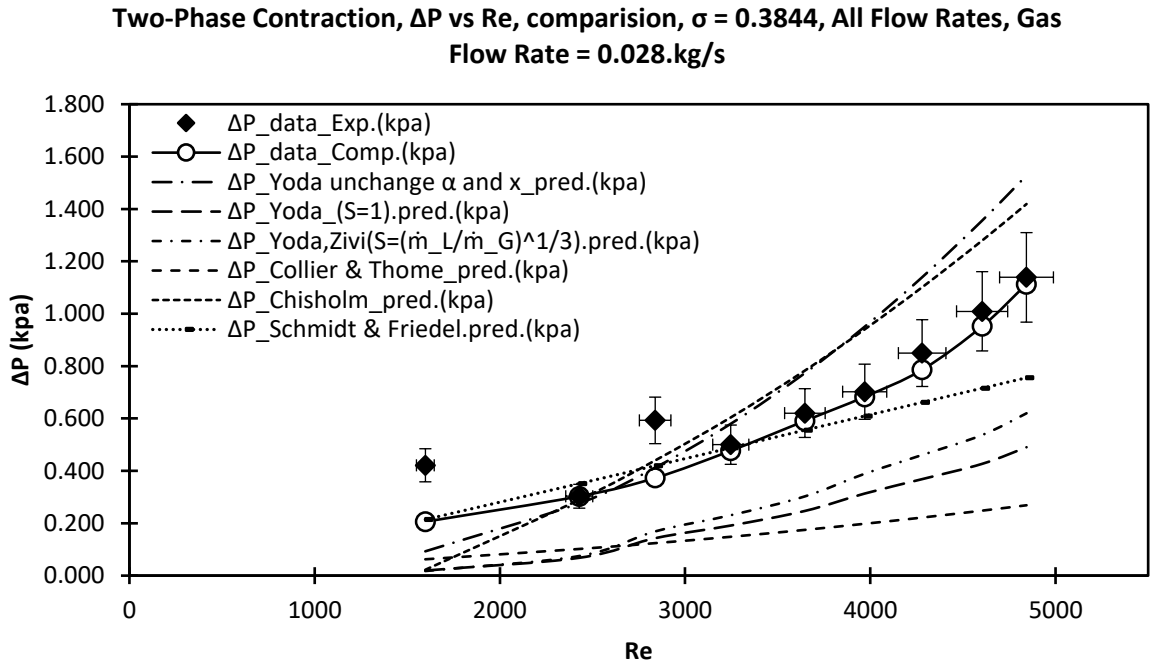

Figure 6.56. Two-phase flow pressure drop performance, compared with experimental data and other co-relations, σ_{con} = 0.3844, $\dot{m}_l$ (kg/s) = 0.005 - 0.03, $\dot{m}_g$ (kg/s) = 0.028

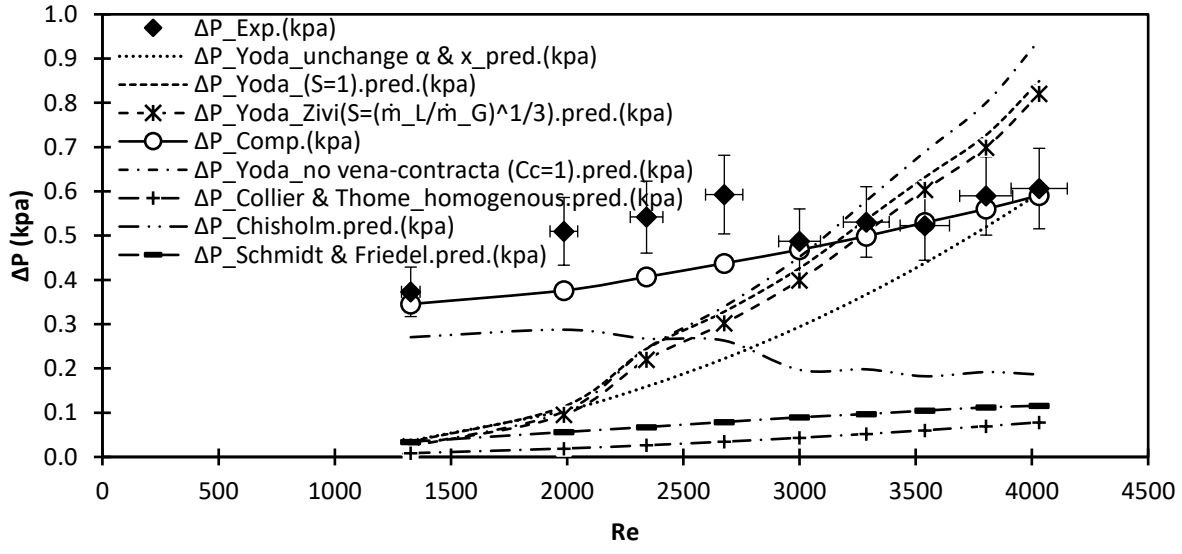

Figure 6.57. Two-phase flow pressure drop performance, compared with experimental data and other co-relations, σ_{con} = 0.5625, $\dot{m}_l$ (kg/s) = 0.005 - 0.03, $\dot{m}_g$ (kg/s) = 0.028

After attaining pressure drop accuracy, these pressure drop values analyzed with experimental analysis and previous researchers. From Figure 6.52 to Figure 6.57 show that pressure drop comparisons using test section $\sigma = 0.1444,\ 0.3844,\ 0.5625$ with gas flow rates 0.00049 kg/s, 0.0095 kg/s, and 0.028 kg/s with consideration of expansion channel and contraction channels for all liquid flow rates. In these figures, the pressure data generated by previous researchers analyzed using homogeneous flow model concept with theoretical calculations. Along with that Yoda co-relation by using no-slip condition that is slip ratio = 1 is being plotted while the current study plotted using computational toolkits. Similarly, Chisholm and Thome's correlations compared with experimental and computational present study. For two-phase flows from above graphs, one can speculate that the pressure drop is considering with the homogeneous model of Yoda, along with experimental results. While for the two-phase pressure drop across sudden contraction, for given gas and liquid flow rate the values for pressure drop are slightly above the predicted ones.

6.2.5 Two-phase flow Void/Volume fraction

while calculating the two-phase flow computationally, void fraction plays a significant role in calculations, similar to which two-phase experimental analysis requires a critical understanding of void fraction. During the computational analysis void fractions of both the phases can be calculated from axial coordinates. Also, void fraction governs the computational analysis stability and the convergence criterion, along with that void fraction shows proportionality concerning pressure drop. This further can be proved from co-relation between void fraction and superficial mass flow rate of liquid as well as gas. Hence, by keeping the constant pressure drop the void fractions are changed, for a liquid void fraction of 0.85 to 0.99 the flow converges to a solution quickly, but as the void fraction is reduced the pressure drop destabilizes including the

convergence of residuals. In order to calculate an accurate value of the void fraction, two co-relations showed promising results, which are Ghajar co-relation and Minami-Bril co-relation.

6.2.6 Two-phase flow pressure contours and velocity vectors

Using the model analysis first, the pressure profiles are developed and matched with information generated from pressure taps of the experiment. After that, the pressure drop values calculated from pressure profiles, compared with previous researcher's co-relations along with current experimental pressure drop values. However, the localization of flow and experimental data generated at inside of test section is difficult and expensive. Therefore, using computational fluid dynamics, it is possible to find the microscale fluid behavior. In this section, the results of pressure contours and velocity vectors are discussed for sudden expansion and contraction channels and their validation using previously calculated pressure drop and pressure profile comparison.

6.2.6.1 Expansion channel

After pressure profile and pressure drop comparison with experimental data for sudden expansion channel, the computational cases including test section with $\sigma = 0.5625,\ and\ 0.1444$ along with gas flow rate of 0.028 kg/s, and liquid flow rate of 0.03 kg/s are used for calculations of pressure contours and velocity vectors. The mentioned flow rates are kept constant, while the diameter of test section changed. This further helps to understand the formation of eddies in both the channels along with local cell velocities of individual phases.

The Figure 6.58 Figure 6.59, and Figure 6.60, show the pressure contours and velocity vectors of test section with $\sigma = 0.1444$. The formation of eddies in velocity vector diagram of this section is higher compared to formation of eddies in test section with $\sigma = 0.5625$, which represents largest

diameter. Also the vectors of Nitrogen velocity show more concentration at center, while the boundary of test section shows negligible attendance of nitrogen. However, the coagulations of nitrogen at corner of sudden change is high compared to coagulation of nitrogen in test section with $\sigma = 0.5625$.. This gas entrapment generates the erosion in the pipes.

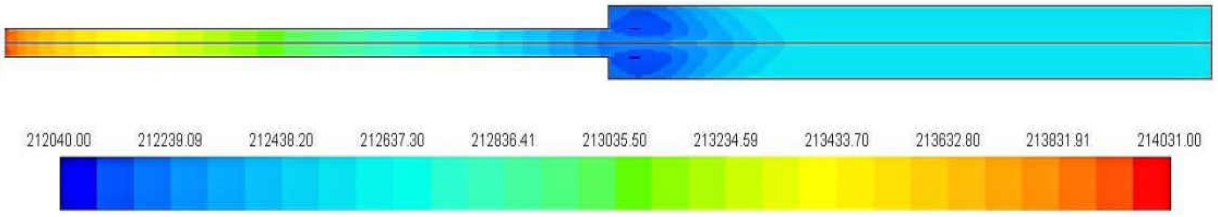

Figure 6.58. Static pressure contours of mixture in $\sigma = 0.1444, \dot{m}_g = 0.\dot{0}28\ kg/s$, $\dot{m}_l = 0.\dot{0}3\ kg/s$, here flow direction is from left to right (Units = Pa).

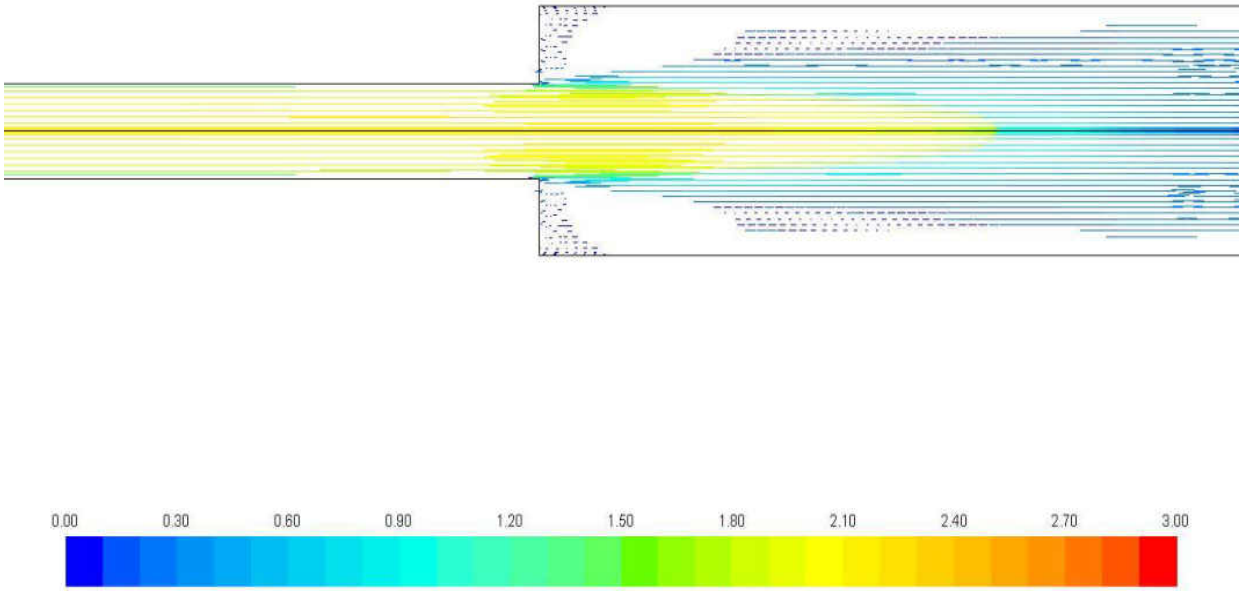

Figure 6.59. Velocity vectors of nitrogen in $\sigma = 0.1444, \dot{m}_g = 0.\dot{0}28\ kg/s$, $\dot{m}_l = 0.\dot{0}3\ kg/s$, here flow direction is from left to right (Units = m/s).

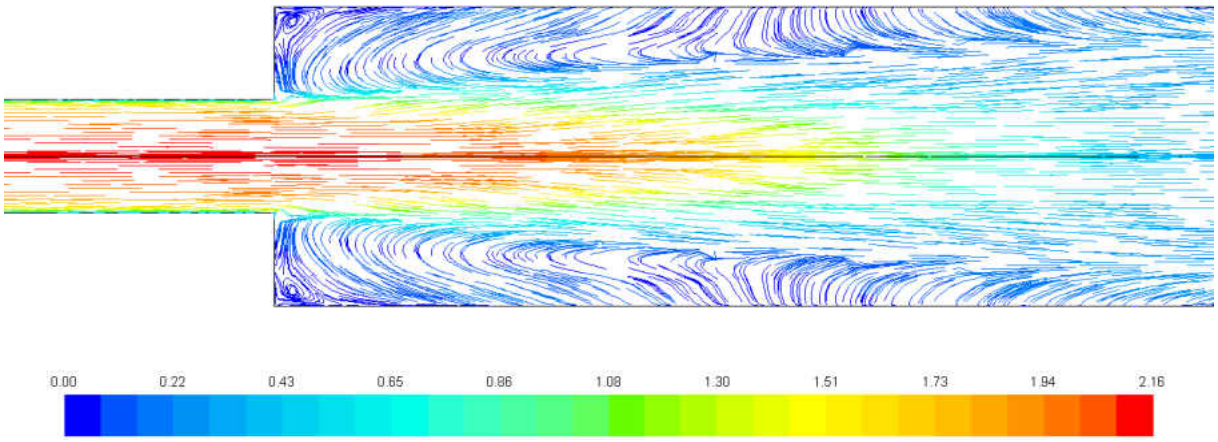

Figure 6.60. Velocity vectors of Water in $\sigma = 0.1444, \dot{m}_g = 0.\dot{0}28$ kg/s , $\dot{m}_l = 0.\dot{0}3$ kg/s , here flow direction is from left to right (Units = m/s).

The Figure 6.61, Figure 6.62, and Figure 6.63 show the pressure contours and velocity vectors of test section with $\sigma = 0.5625$. This test section holds largest diameter as inlet while the outlet diameter is 0.5 inches. Thus the diameter difference between inlet and outlet is lowest compared to other test sections this proves the pressure drop is very low compared to $\sigma = 0.1444$, thus this results in to less development of rapid velocity increment, which further gives us the understanding of less eddy currents formation causing less erosion of pipe wall. In the pressure contour graph, the formation of green contours explains the large dwell in pressure profile graph.

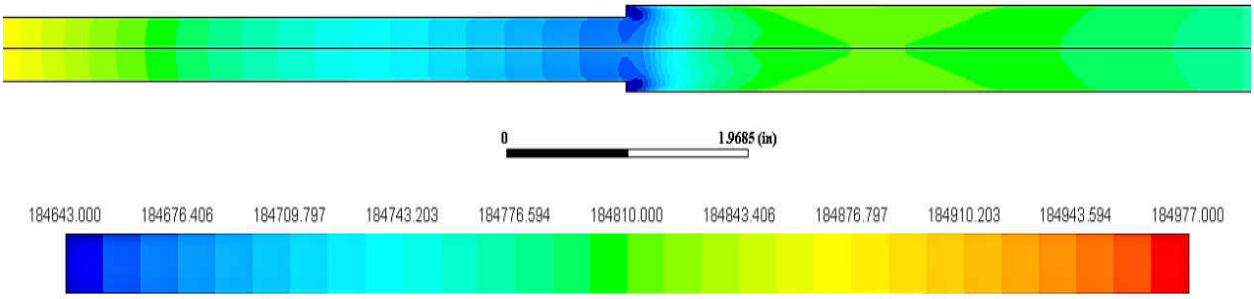

Figure 6.61. Static pressure contours of mixture in $\sigma = 0.5625, \dot{m}_g = 0.\dot{0}28\ \text{kg/s}$, $\dot{m}_l = 0.\dot{0}3\ \text{kg/s}$, here flow direction is from left to right (Units = Pa).

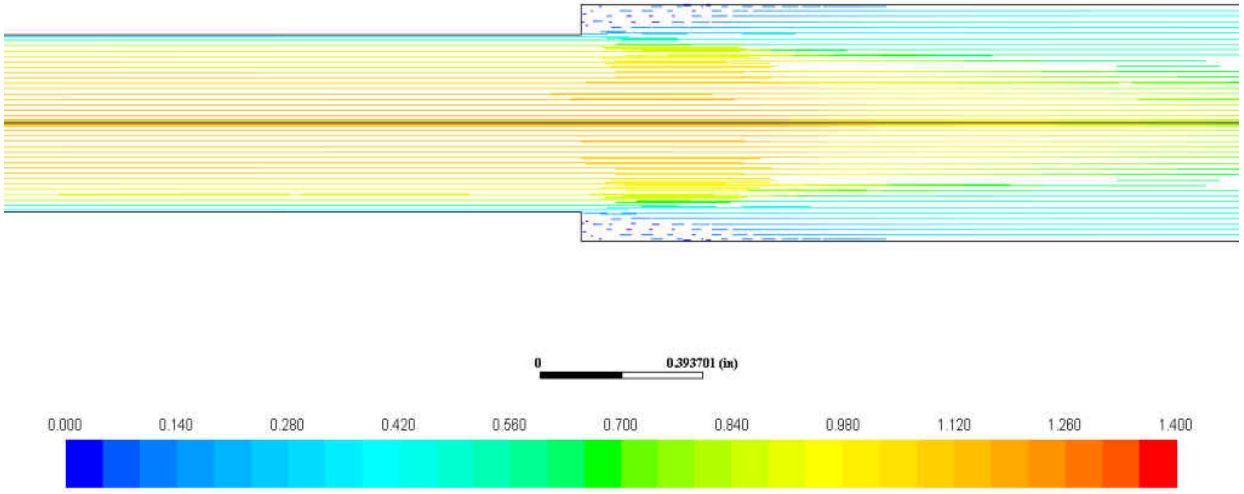

Figure 6.62. Velocity vectors of nitrogen in $\sigma = 0.5625, \dot{m}_g = 0.\dot{0}28\ \text{kg/s}$, $\dot{m}_l = 0.\dot{0}3\ \text{kg/s}$, here flow direction is from left to right (Units = m/s).

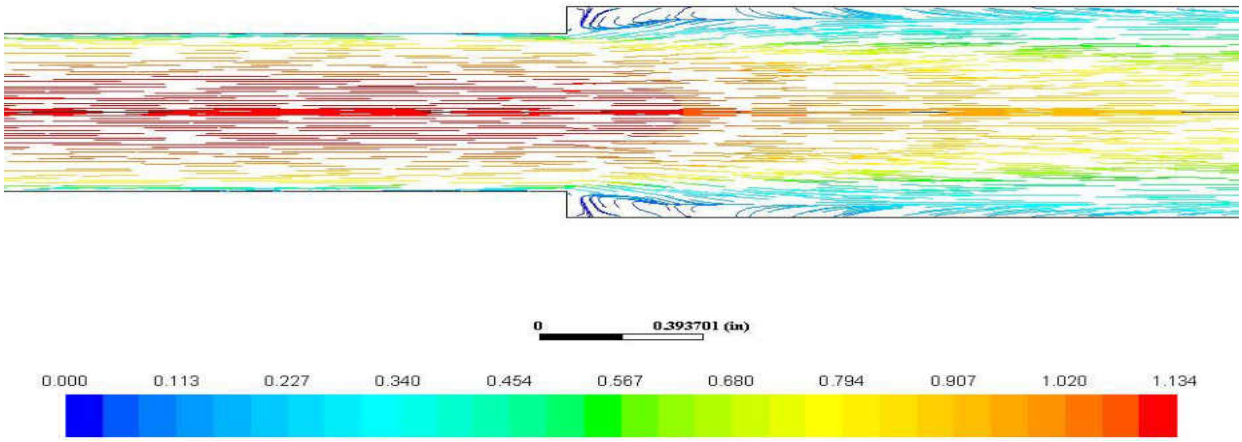

Figure 6.63. Velocity vectors of water in $\sigma = 0.5625, \dot{m}_g = 0.\dot{0}28\ \text{kg/s}$, $\dot{m}_l = 0.\dot{0}3\ \text{kg/s}$, here flow direction is from left to right (Units = m/s).

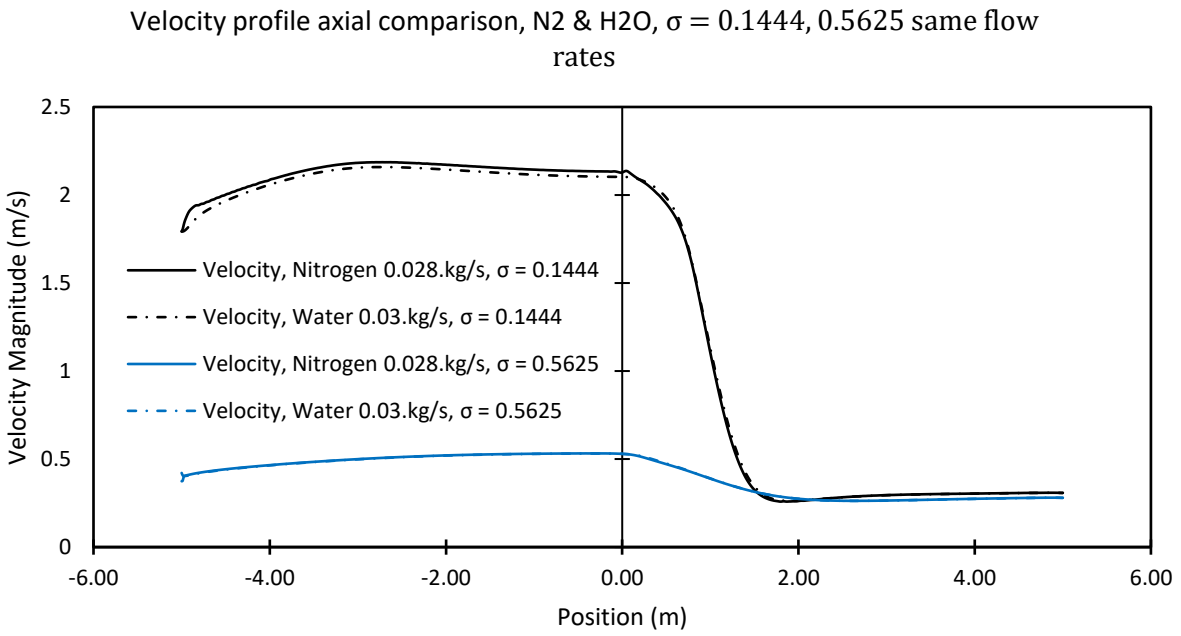

Figure 6.64. Graph of superficial velocities of nitrogen and water for both expansion test sections with same flow rates.

In terms of sudden expansion phenomenon, pressure reduces right after change in area, which gives immediate rise to velocity, this velocity increment rises the formation of eddies, and flow becomes chaotic turbulent. This situation forms small swirling eddies at the corner of pipe causing erosion of pipe wall. After which flow starts stabilizing through the channel.

6.2.6.2 Contraction channel

After pressure profile and pressure drop comparison with experimental data for sudden contraction channel, the computational cases including test section with $\sigma = 0.5625,\ and\ 0.1444$ along with gas flow rate of 0.028 kg/s, and liquid flow rate of 0.03 kg/s are used for calculations of pressure contours and velocity vectors. The mentioned flow rates are kept constant, while the diameter of test section changed. The understanding of the formation of eddies in both the channels along with local cell velocities of individual phases can be achieved using these graphs.

The Figure 6.65, Figure 6.66, and Figure 6.67 show the pressure contours and velocity vectors of test section with $\sigma = 0.1444$. In test section with $\sigma = 0.5625$, which represents largest diameter, the formation of eddies in velocity vector diagram of this section is lower compared to formation of eddies for test section with $\sigma = 0.1444$.. In addition, the vectors of Nitrogen velocity show more concentration at center, although, the boundary of test section shows sufficient amount of nitrogen compared to expansion phenomenon. Thus, the coagulations of nitrogen at corner of sudden change is less compared to coagulation of nitrogen in test sections of sudden expansion phenomenon. As result, less gas entrapment generates the less erosion in the pipes, hence, recommendation of lager diameter is more advisable.

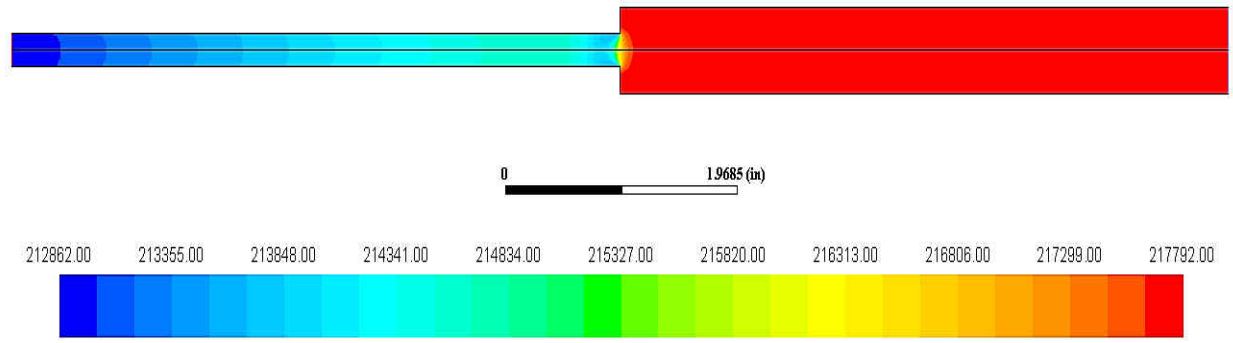

Figure 6.65. Static pressure contours of mixture in $\sigma = 0.1444, \dot{m}_g = 0.\dot{0}28\ \text{kg/s}$, $\dot{m}_l = 0.\dot{0}3\ \text{kg/s}$, here flow direction is from right to left (Units = Pa).

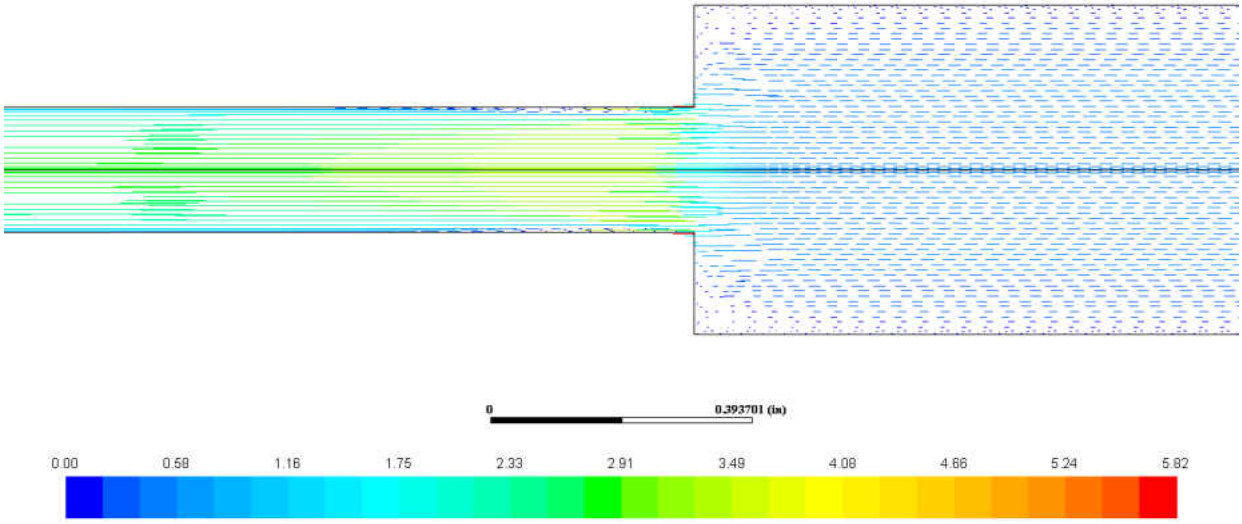

Figure 6.66. Velocity vectors of nitrogen in $\sigma = 0.1444, \dot{m}_g = 0.\dot{0}28\ \text{kg/s}$, $\dot{m}_l = 0.\dot{0}3\ \text{kg/s}$, here flow direction is from right to left (Units = m/s).

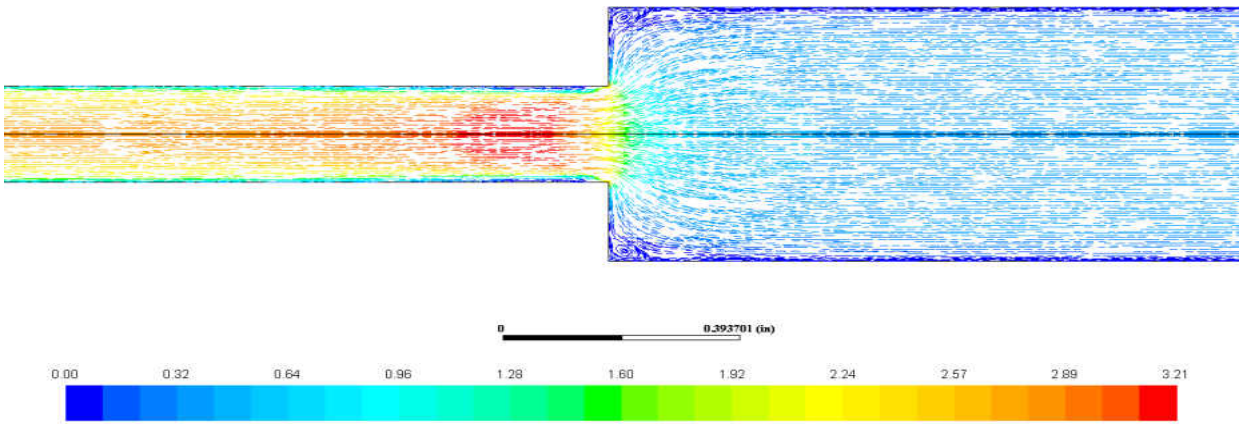

Figure 6.67. Velocity vectors of Water in $\sigma = 0.1444, \dot{m}_g = 0.\dot{0}28\ kg/s$, $\dot{m}_l = 0.\dot{0}3\ kg/s$, here flow direction is from right to left (Units = m/s).

The Figure 6.68, Figure 6.69, and Figure 6.70 show the pressure contours and velocity vectors of test section with $\sigma = 0.5625$. The diameter difference between inlet and outlet is lowest compared to other test sections because, this test section holds largest diameter at outlet while the inlet diameter is 0.5 inches. This proves the pressure drop is very low compared to $\sigma = 0.1444$, thus these results in to less development of rapid velocity increment, which further gives us the understanding of less eddy currents formation causing less erosion of pipe wall. In the pressure contour graphs o

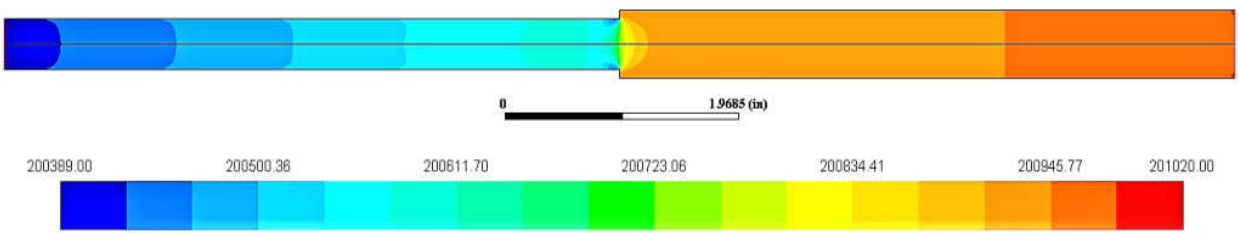

Figure 6.68. Static pressure contours of mixture in $\sigma = 0.5625, \dot{m}_g = 0.\dot{0}28\ kg/s$, $\dot{m}_l = 0.\dot{0}3\ kg/s$, here flow direction is from right to left (Units = Pa).

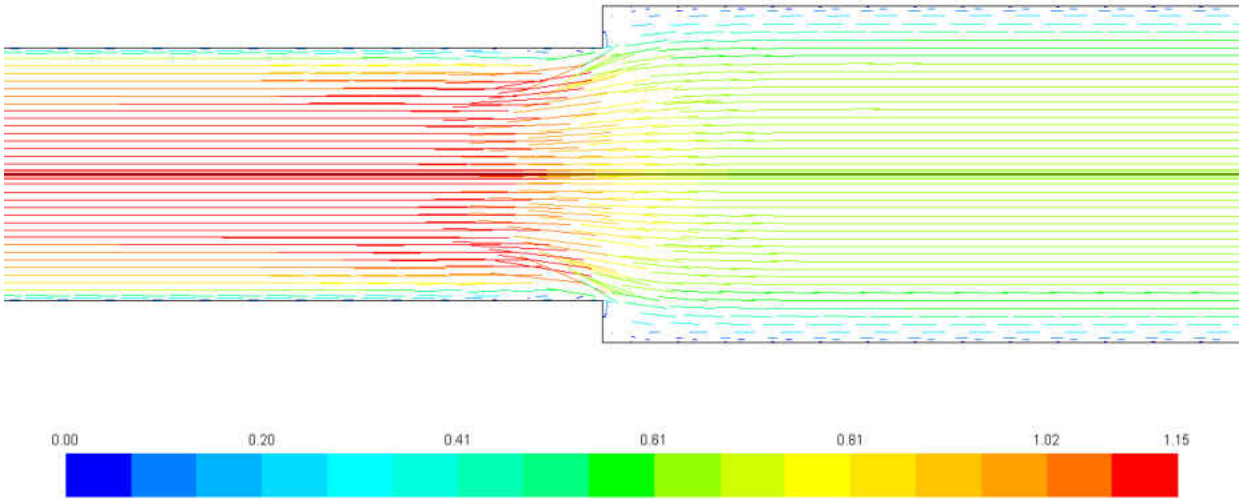

Figure 6.69. Velocity vectors of nitrogen in $\sigma = 0.5625, \dot{m}_g = 0.\dot{0}28\ \text{kg/s}$, $\dot{m}_l = 0.\dot{0}3\ \text{kg/s}$, here flow direction is from right to left (Units = m/s).

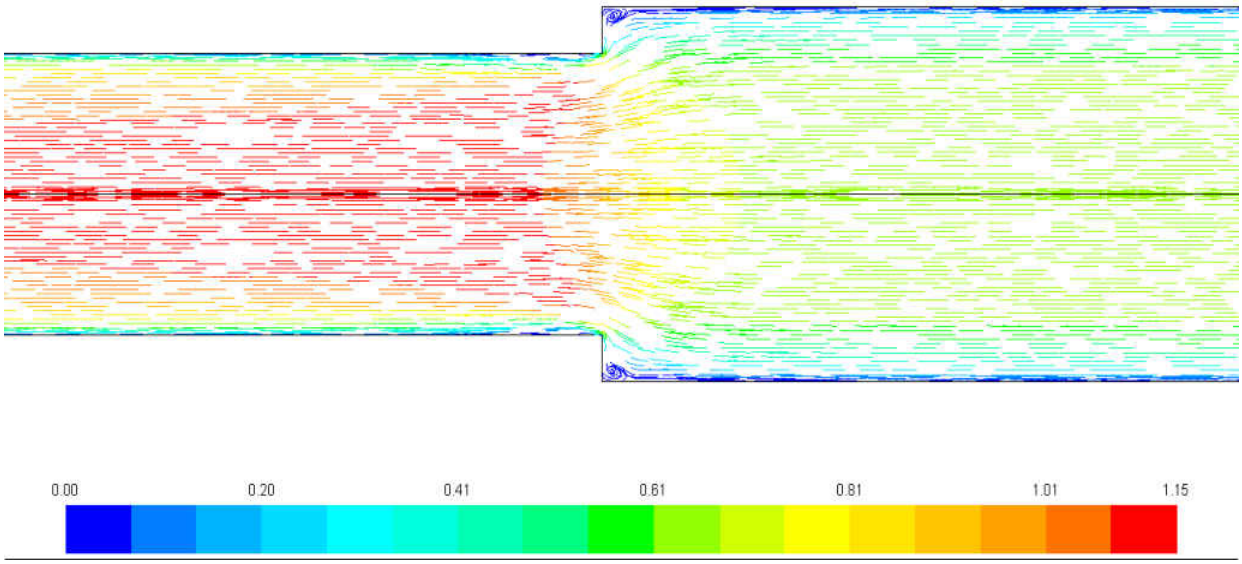

Figure 6.70. Velocity vectors of water in $\sigma = 0.5625, \dot{m}_g = 0.\dot{0}28\ \text{kg/s}$, $\dot{m}_l = 0.\dot{0}3\ \text{kg/s}$, here flow direction is from right to left (Units = m/s).

Regarding sudden contraction phenomenon, the pressure reduces right after a change in the area, which gives immediate rise to velocity. This velocity increment rises the formation of eddies at the corner of the area change. Thus, causing further velocity currents growth and flow becomes chaotic turbulent causing liquid particles to lose some energy, which generates drastic amount of pressure drop causing formation of Venna-contracta C_c. This can be seen in above contraction pressure contour. Further, downstream, at distance of 5D, the pressure regains its value by causing slight dwell in pressure profile, followed by linear stability in flow and generation of linear line with slop of approximately 45^0.

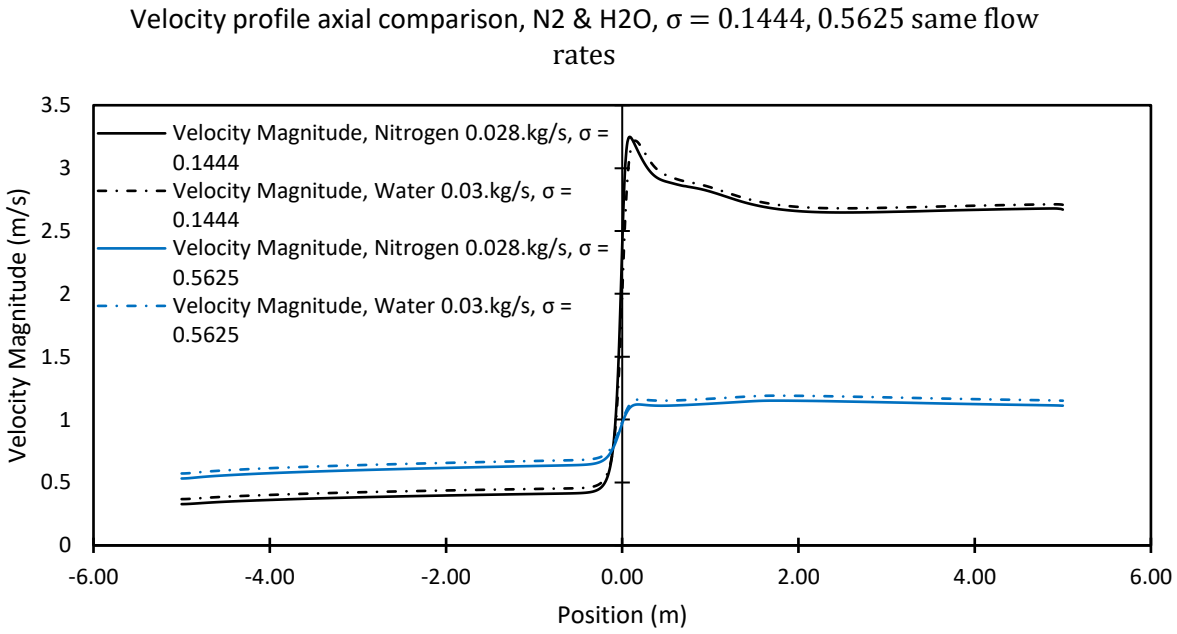

Figure 6.71. Graph of superficial velocities of nitrogen and water for both contraction test sections with same flow rates.

CHAPTER VII

CONCLUSION AND RECOMMENDATIONS

7.1 Conclusion

Typical industrial and heat-exchanging devices show two-phase and single-phase flow singularities such as impulsive expansion and sudden contraction. These singularities generate minor and significant energy losses in flow reducing system's efficiency; hence, these are dealt with change in geometry of particular section or change an entire system's anatomy. Nevertheless, beforehand studies are performed with extensive experimentation and computational analysis. Therefore, as the applications are increased, thus study of the single and two-phase flow across abrupt contraction and expansion channels have been increased over the years. Based on the applications in oil and gas industry the investigated two-phase and single-phase studies shows datasets and calculations for larger diameter channels and the correlation equations normally derived predicts answers for larger diameter channels. However, In this study, the miniature diameters of test section proves the well-established analysis for flows such as coolants or hydraulic oils inside micro-electro-mechanical systems, for example, robots such as industrial robotic arms, PC which is devised with the only purpose of high powered video gaming systems, such as customs made PC's by Digital Storm corporation. Apart from this, these small systems hold details of intricacies of flow behavior such as turbulence, the exact behavior of fluid particles under local velocities, the existence of each phase at specified location at the instance of time, and behavior of pressure in details. Thus, such data generation using experimental analysis becomes difficult and sometimes impossible. In these scenarios, the use of Computational Fluid Dynamics

fulfills the requirement. Moreover, therefore, the use of computational and mathematical modeling achieved in this research over pre-existing experimental analysis.

Application of two-phase flow across the immediate area of expansion and contraction has been increased in recent years. Most two-phase studies were done by researchers using large diameter channel. This study shows predicting of data for channels with a smaller diameter as a cross-section. The experimental results collected with high accuracy with precision instruments; however, pressure difference along channel was a significant factor for observation. Due to a reduction in channel diameter pressure loss value increases, while its direct proportionality shows increment with mass flow rate. Pressure drop is directly proportional to the Reynolds number for specific hydraulic diameter.

The flow profiles show the RSM turbulence model is better for experimental comparison rather than a $rk - \epsilon$ model for higher flow rates. Nevertheless, for lower flow rates (0.005 kg/s) it does not provide better solution for pressure and turbulence behavior.

From the experimental, and computational results, it has been observed that, for the same water mass flow rate operating in different contraction or expansion channels for single-phase flow, Reynolds number is either fully turbulent flow for smaller area ratios, while it is either transition or laminar in larger area ratios. Apart from that, the Reynolds number is directly proportional to the presence of pressure drop in the channel.

Vena contracta is always established at downstream of flow just after the cross-section of contraction or at 5D measurement in single phase flow. Its position usually depends on mass flow rate. This can be proved from the pressure contours of the test section. Further, the same contours can give insights of changing Venna-Contracta profiles as the area ration changes. For larger area

ratio, these pressure profiles provide less presence of vena contracta, while smaller diameter channels show a significant presence of vena contracta.

Pressure drop at cross-section with a larger ratio of the area shows slightly lower value compared to its experimental value. Hence, in general, the computed values of two-phase flow pressure changes caused by a sudden area of expansion and contraction are found to be slightly lower than the predicted values from co-relations but shows relatively good agreement with slip flow model. It is observed that significant velocity slips in the vicinity of flow area change.

Two-phase flow in the smaller area ratio contraction channels and lower gas mass flow rate, the pressure drop can be estimated highly accurate with experimental data by using Zivi's [26] slip ratio model prediction. For the smaller area ratio and lower gas mass flow rate in two-phase flow expansion channels, the result indicates that the Yoda's not changing void fraction logical co-relation is the best prediction for this case but the void fraction is obtaining needs a new investigation and result. In this situation, the void fraction is obtained by inverse method

Regarding two-phase flow, the void fraction co-relation based on drift-flux by Ghajar [36] shows better results in terms of pressure drop comparison for evaluated cases. Especially the smaller diameter channels do provide reasonable pressure drop concerning pressure drop of experimental analysis. This model is based on drift flux.

Local velocity profiles show velocity values at each point along the center axis, which give precise idea about, the behavior of particles in test section under the influence of pressure. The rise of pressure decreases the speed of the particle, while the loss of pressure accelerates the particle providing a dramatic rise in velocity profiles. Also, local velocities of each particle do provide an idea about the hydraulic diameter channel. Moreover, this relationship is inversely proportional.

7.2 Recommendations

Many predictions and correlation equations and formulas can be found from the previous works and studies for single and two-phase flow with abrupt contraction and expansion. Most of these studies are carried out with experimental analysis, where larger diameter channels are chosen. In recent years, due to electronics development and small systems in industries. The Research with smaller diameter is yet to come up to research limelight.

Nevertheless, other than experimental analysis. A huge development in computational analysis is yet to achieve greater peaks in industry. Although the development in personal computers, or clusters or super-computers is progressing fast, the reliability over computational software predictions is not at par in industries. Turbulence, which is considered as vast chaotic subject is yet to understand by either experimental or computational analysis. Apart from this, although in recent years the understanding of computational analysis is approved; open-source high performance computing is still yet to achieve industry standards. This research study can be achieved by open source computational software such as OpenFOAM (Open Field Operation and Manipulations). The Algorithms used in software are yet to refine further, so that even after physics and mathematics based ideal model should not crash, or generate anomalies in answers.

BIBLIOGRAPHY

[1] R. Benedict, Fundamentals of Pipe Flow, New York: John Wiley & Son, 1980.

[2] D. Chisholm and A. Laird, "Two-phase flow in rough tubes," *ASME,* no. 80, pp. 276-286, 1985.

[3] N. Goldberg, "Narrow channel forced air heat sink," *IEEE Trans. Comp. Hybrids Manuf. Technol,* vol. 7, pp. 154-159, 1984.

[4] C. C. Tang and A. J. Ghajar, "Void Fraction and Flow Patterns of Two-Phase Flow in Upward and Downward Vertial and Horizontal Pipes," *Advances in Multiphase flow and Heat Transfer,* vol. 4, pp. 175-201, 2011.

[5] J. Weisman, A. Hussain and B. Harshe, "Two phase pressure drop across abrupt area changes and restrictions.," *Proceedings of condensed papers,* vol. 9, pp. 301-303, 1976.

[6] Y. Taitel, D. Bornea and A. Dukler, "Modeling flow pattern transitions for steady upward gas-liquid flow in vertical tubes," *AIChE J,* vol. 26, pp. 345-354, 1980.

[7] A. E. Bergles, J. G. Collier, J. Delhaye and G. Hewitt, Two-phase flow and heat transfer in the power and process industries, New-York: Hemisphere, 1981.

[8] M. Yoda, F. Abdelall, G. Hahn, S. Ghiaasiaan, S. Abdel-Khalik, S. Jeter and D. Sadowski, "Pressure drop caused by abrupt flow area changes in small channels," *Experimental thermal and fluid science,* vol. 29, pp. 425-434, 2005.

[9] M. Wadle, "A new formula for the pressure recovery in an abrupt diffuser," *Internaitonal Journal of Multiphase flow,* vol. 15, pp. 241-256, 1989.

[10] J. Chen and P. Spedding, "An analysis of holdup in horizontal two-phase gas-liquid FLow," *Int. J. Multiphase Flow,* 1983.

[11] J. Schmidt and L. Freidel, "Two-phase pressure drop across sudden contractions in duct areas," *International Journal of Multiphase Flow,* vol. 2, no. 23, pp. 283-299, 1997.

[12] A. Attou and Bolle, "A New Correlation for the Two-phase Pressure Recovery Downstream From a Sudden Enlargement,," *Chemical Engineering Technology,,* vol. 20, 1997.

[13] J. Schmidt and L. Friedel, "Two-Phase flow pressure change across sudden expansion in duct area," *Chemical Engineering Communications,* vol. 6, no. 10, pp. 175-190, 1996.

[14] I. Y. Chen, S. Wongwises, B.-C. Yang and C.-c. Wang, "Two-phase flow across small sudden expansions and contractions," *Heat Transfer Engineering,* vol. 31, no. 4, pp. 298-309, 2010.

[15] J. Schmidt and L. and Friedel, "Two-Phase Flow Pressure Change," *Chemical Engineering Communications,* no. 141, 1995.

[16] G. E. Geiger, "Sudden contraction losses in single and two phase flow," University of Pittsburgh, Pittsburgh, 1964.

[17] D. Chisholm and L. Sutherland, Prediction of pressure gradients in pipeline systems during two-phase flow, London: SAGE Publications, 1969.

[18] D. Beattie and P. Whalley, "A simple two-phase frictional pressure drop calculation method.," *Int. J. Multiphase Flow,* 1982.

[19] G. Hewitt and N.S. Hall-Taylor, Annular Two-Phase Flow, Oxford: Pergamon Press, 1970.

[20] Hewitt, G. Hewitt, G. Shires and T. Bott, Process Heat Transfer, Ann Arbor: CRC Press, 1993.

[21] E. Janssen and J. Kervinen, "Two-phase pressure drop across contractions and expansion, steam–water mixtures at 600–1400 psia," General Electric Company, Atomic Power Equipment, San Jose, California, 1964.

[22] T. J. Collier J.G., in *Converctive boiling and condensation* , New York, Oxford, 1994, pp. 109-111.

[23] M. M. Awad and Y. S. Muzychka, "Bounds on Two-Phase Frictional Pressure Gradient and Void Fraction in Circular Pipes," *Advances in Mechanical Engineering,* vol. 6, pp. 438-428, 2015.

[24] A. Armand and G. and Treschev, "The resistance during the movement of a two-phase system in horizontal pipes," pp. 16-23, 1946.

[25] J. Lahey and F. Moody, The Thermal Hydraulics of Boiling Water Nucrear Reactor., Illinois: American Nuclear Society, 1993.

[26] S. Zivi, "Estimation of steady state steam void fraction by means of principle of minmum entropy production," *ASME,* vol. C, no. 86, p. 237252, 1964.

[27] K. A.A., C. P.M.Y. and K. M., "International journal of heat and mass transfer," *Investigation of two phase flow pattern, void fraction and pressure drop in a microchannel,* vol. 28, pp. 1411-1435, 2002.

[28] F. Romie, P. Lottes, M. Petrick and J. Marchaterre, "Lecture notes on heat extraction from boiling water power reactors," osti.gov, San Jose, California, 1959.

[29] B. Richardson, "Some problems in horizontal two-phase two-component flow (P.hD. dissertation, Purdue)," Purdue University, Purdue, Indiana, 1958.

[30] N. Al'Ferov and Y. Shul'Zhenko, "Pressure drops in two-phase flows through local resistances," *Fluid Mechanics Soviet Research,* vol. 6, pp. 20-33, 1977.

[31] G. Guglielmini, A. Muzzio and G. Sotgia, "The structure of two-phase flow in ducts with sudden contractions and its effects on the pressure drop," *Experimental Heat Transfer, Fluid Mechanics and Thermodynamics,* vol. 11, pp. 41-57, 1997.

[32] D. Chisholm, in *Two-phase flow in pipelines and heat exchangers*, London, George Godwin, 1983, pp. 175-192.

[33] K. Triplett, S. Ghiaasiaan, S. Abdel-Khalik, A. LeMouel and B. McCord, "Ga-liquid two-phase flow in microchannels Part II: void fraction and pressure drop," *International Journal of Multiphase Flow,* no. 25, pp. 395-410, 1999.

[34] T. Balakhrisna, S. Ghosh, G. Das and P. Das, "Oil–water flows through sudden contraction and expansion in a horizontal pipe – Phase distribution and pressure drop," *International Journal of Multiphase Flow,* vol. 36, no. 1, pp. 13-24, 2010.

[35] M. B. Bowers and I. Mudawar, "High flux boiling in low flow rate, low pressure drop mini-channel and micro-channel heat sinks," *Int. J. Heat Mass Transfer,* vol. 37, no. 2, pp. 321-332, 1994.

[36] M. Woldesemayat and A. Ghajar, "Comparison of void fraction correlations for different flow patterns in horizontal and upward inclined pipes," *International Journal of Multiphase Flow,* vol. 33, pp. 347-370, 2007.

[37] P. Bhramara, V. D. Rao, K. V. Sharma and T. K. K. Reddy, "CFD Analysis of Two Phase Flow in a Horizontal Pipe – Prediction of Pressure Drop," *World Academy of Science,* no. 40, pp. 1-7, 2008.

[38] H. Müller-Steinhagen and K. Heck, "A simple friction pressure drop correlation for two-phase flow in pipes," *Chemical Engineering and Processing: Process Intensification,* vol. 20, no. 6, pp. 297-308, 1984.

[39] M. Roul and S. Dash, "Two-phase pressure drop caused by sudden flow area contraction/expansion in small circular pipes," *International Journal for Numerical Methods in Fluids,* vol. 66, no. 1, p. 1420–1446, 2011.

[40] M. Roul and S. Dash, "Single-Phase and Two-Phase Flow Through Thin and Thick Orifices in Horizontal Pipes," *Journal of Fluids Engineering, ASME,* vol. 134, no. 5, 2012.

[41] P. Patro and S. Dash, "Computations of Particle-Laden Turbulent Jet Flows Based on Eulerian Model," *Journal of Fluids Engineering, ASME,* vol. 136, no. 1, pp. 113-129, 2014.

[42] M. Roul and S. Dash, "Pressure drop caused by two-phase flow of oil/water emulsions through sudden expansions and contractions: a computational approach," *emerald insights, Emerald Group Publishing Limited,* vol. 9, no. 5, pp. 665-688, 2008.

[43] R. Pal and C. Hwang, "Flow of Two Phase Oil/Water Mixtures through Sudden Expansions and Contractions," *Chemical Engineering Journal,* vol. 68, no. 2, pp. 157-163, 1997.

[44] H. Rusche, "Computational Fluid Dynamics of Dispersed Two-Phase Flows at High Phase Fractions," Imperial College of Science, Technology & Medicine, London, 2002.

[45] A. Abaas, "Two Phase Flow Pressure Drop in a Horizontal Pipe," *Al- Mustansiriya Journal Sciences,* vol. 21, no. 2, pp. 133-143, 2010.

[46] A. Kartushinsky, S. Tisler and J. Oliveira, "Eulerian-Eulerian modelling of particle-laden two-phase flow," *Powder Technology,* vol. 301, no. 7, p. 999–1007, 2016.

[47] G. Anjos, "A 3D ALE Finite Element Method for Two-Phase Flows with Phase Change," école polytechnique fédérale de lausanne, lausanne, Switzerland, 2012.

[48] S. Szczukiewicz, M. Magnini and J. Thome, "Proposed models, ongoing experiments, and latest numerical simulations of microchannel two-phase flow boiling," *International Journal of Multiphase Flow,* vol. 59, no. 11, pp. 84-101, 2014.

[49] O. Ubbink, "Numerical prediction of two fluid systems with sharp interfaces," Imperial College of Science, Technology & Medicine, London, 1997.

[50] C.-H. Yang and C. and Tang, "Two-phase flow pressure drop in circular small channels with abrupt contraction and expansion," University of North Dakota, Grand Forks,ND, 2015.

[51] T. Saito, E. Hughes and M. Carbon, "Multi-fluid modeling of annular two-phase flow," *Nuclear Engineering and Design,* vol. 50, no. 2, pp. 225-271, 1978.

[52] D. Spalding, "A general purpose computer program for multi-dimensional one- and two-phase flow," *Mathematics and Computers in Simulation (MATCOM),* vol. 23, no. 3, pp. 267-276, 1981.

[53] B. Launder and D. Spalding, "The numerical computation of turbulent flows," *Computer Methods in Applied Mechanics and Engineering,* vol. 11, no. 3, pp. 269-275, 1974.

[54] M. M. Gibson and B. E. Launder, "Ground effects on pressure fluctuations in the atmospheric boundary layer," *Journal of Fluid Mechanics,* vol. 3, no. 68, p. 125–143, 1975.

[55] A. Chorlin, "Numerical solution of the Navier-stoke's equations," *Mathematical Computational Physics,* vol. 22, pp. 745-760, 1978.

[56] G. H. Yeoh and J. Tu, Computational Techniques in Multiphase flows, London : Elsevier, 2010.

[57] D. Drew, "Mathematical modeling of two-phase flows," *Annual Review of Fluid Mechanics,* vol. 3, no. 15, pp. 261-291, 1983.

[58] D. Drew and R. Lahey, "Application of general constitutive principles to the derivation of multidimensional two-phase flow equations," *International Journal of Multiphase Flow,* vol. 11, no. 7, pp. 243-264, 1979.

[59] D. Gidaspow, Multiphase Flow and Fluidization: Continuum and Kinetic Theory Descriptions, Boston,MA: Academic Press, 1994.

[60] L. Schiller and A. and Naumann, "A drag coefficient correlation.;," *Z. Ver. Deutsch. Ing;,* vol. 1, no. 77, p. 318–320, 1935.

[61] T. Cook and F. Harlow, "Virtual Mass in Multiphase Flows," *International Journal of Multiphase flows,* vol. 10, no. 6, pp. 691-696, 1984.

[62] H. Anglart, O. Nylund, N. Kurul and M. Podowski, "Cfd prediction of flow and phase distribution in fuel assemblies with spacers," *Nuclear Engineering and Design,* no. 177, pp. 215-228, 1997.

[63] B. E. Launder, G. J. Reece and W. Rodi, "A new correlation for the two-phase pressure recovery downstream from a sudden enlargement," *Experimental Heat Transfer, Fluid Mechanics and Thermodynamics,* vol. 6, no. 20, pp. 537-566, 1975.

[64] H. Ueda and J. O. Hinze, "Fine-structure turbulence in the wall region of a turbulent boundary layer," *Journal of Fluid Mechanics,* vol. 1, no. 67, pp. 125-143, 1975.

[65] S. E. Elgobashi and T. and Abou-Arab, "A two equation turbulence model for two-phase flows.," *Physics of Fluids,* vol. 4, no. 26, pp. 931-938, 1983.

[66] A. Troshko and Y. Hassan, "A two-equation turbulence model of turbulent bubbly flows," *International Journal of Multiphase Flow,* vol. 11, no. 2, pp. 1965-2000, 2001.

[67] W. L. A. S. Z. Y. a. J. Z. T.-H. Shih, "A New - Eddy-Viscosity Model for High Reynolds Number Turbulent Flows - Model Development and Validation," *Computers Fluids.,* vol. 24, no. 3, pp. 227-238, 1995.

[68] O. Simonin and P. L. Viollet, "Modeling of Turbulent Two-Phase Jets Loaded with Discrete Particles," *Phenomena in Multiphase Flows,* pp. 259-269, 1990.

[69] O. Simonin and P. L. Viollet, "Predictions of an Oxygen Droplet Pulverization in a Compressible Subsonic Coflowing Hydrogen Flow," *Numerical Methods for Multiphase Flows,* vol. FED, no. 91, pp. 65-82, 1990.

[70] B. Leonard, "Locally modified QUICK scheme for highly convective 2-D and 3-D flows," *Numerical methods in laminar and turbulent flow,* vol. 5, no. 1, pp. 35-47, 1987.

[71] C. Rhie and W. Chow, "Numerical study of the turbulent flow past an airfoil with trailing edge separation," *AIAA journal,* vol. 21, no. 11, pp. 1525-1532, 1983.

[72] S. Patankar, "A calculation procedure for two-dimensional elliptic situations," *Numerical heat transfer,* vol. 4, no. 4, pp. 409-425, 1981.

[73] K. Triplett, S. Ghiaasiaan, S. Abdel-Khalik, Sadowski and D.L., "Gas-liquid two-phase flow in microchannels Part I: two-phase flow patterns," *International Journal of Multiphase Flow,* no. 25, pp. 377-394, 1999.

[74] S. G. Toufik Y. Chalfi, "Pressure drop caused by flow area changes in capillaries under low flow conditions," *International journal of mutiphase flow,* pp. 1-11, 2007.

[75] W. Idsinga, N. Todreas and R. Bowring, "An assessment of two-phase pressure drop correlations for steam-water systems," *International Journal of Multiphase Flow,* vol. 3, no. 5, pp. 401-413, 1976.